Sedimentology of Convergent Margins

Symposia and field trips to celebrate the 100th anniversary of the Society for Sedimentary Sedimentology

Organizers

Ludvig Löwemark[1] and Shahin Dashtgard[2]

[1]National Taiwan University
[2]Simon Fraser University



To celebrate SEPM's 100th anniversary, and almost ten years of successful collaboration, Shahin Dashtgard at Simon Fraser University, Canada, and Ludvig Löwemark, NTU, invited specialists to a scientific meeting dedicated to the sedimentology of convergent margins. From experience, most scientific interaction at meetings does not take place through technical presentations, but happens during breaks, meals, or field trips. To capitalize on this insight, we structured the meeting around two symposia flanked by field trips to selected sites chosen to highlight different stages of the formation of Taiwan. In all, 17 sedimentologists from 10 different countries representing four continents presented their research and participated in the geological field trip around Taiwan.

The first symposium was held at the Department of Geosciences (NTU) and featured two keynote presentations. First Michael Hren from University of Connecticut, USA, outlined how compound specific isotopes can be used to estimate the altitude of the uplifting Taiwan orogen over the past 5–6 million years. Our second keynoter speaker, Annette George from University of Western Australia, gave an overview of the continent-arc collisions responsible for the formation of northern Thailand.

Speaker	**Convener: Ludvig Löwemark**
Ludvig Löwemark	Welcome address and introduction to Taiwan
Michael Hren	**Keynote**: Organic molecular paleohypsometry: Promises, pitfalls and implications for the topographic evolution of the Taiwan orogen
Sung-Ping Chang	Millennial- to Centennial-Scale Sequence Stratigraphy in the Choshui River Subaqueous Delta, Offshore Taiwan
Tae Soo Chang	Wave-modulated, macrotidal open-estuary tidal bar facies at the Geum River estuary mouth, mid-western coast of Korea: resembling open-coast tidal flats

Speaker	Convener: Shahin Dashtgard
Annette George	**Keynote**: Basin Evolution and Paleozoic-Mesozoic terrane assembly in Northern Thailand
Zong-Dai Chen	Integrating Microfossil and Geochemical Evidence to Refine the Paleoenvironmental Understanding of the Szekou Formation in southern Taiwan
Chelsea Wong	Sedimentary Environment Evolution of the Maobitou Limestone on the Western Hengchun Tableland, Southern Taiwan
Zhonghao Zhang	The Role of Coccolithophore Deposition in Moving Suspensions: Importance of Flocculation and Its Implication for Modern and Ancient Calcareous Ooze (Chalk) Deposition
Juan José Ponce	Recurrence of hyperpycnites in the cenozoic of the foreland Austral Basin, Argentina
Milovan Fustic	Potential Genetic Relation of Coal-bearing Foreland and Pull-apart Basins of Central Kazakhstan and Carboniferous Pacific-type Convergent Margin System of the Paleo-Asian Ocean
Yechan Park	Three-Dimensional facies architecture and estuary–delta transition in a Holocene tide-influenced system, southern coast of Korea
Noelia Carmona Juan Ponce	Paleoenvironmental analysis of the Lower Cretaceous Río Mayer Formation (Austral Basin), Argentina

After the first symposium, we took the group for a two-and-a-half-day field trip to visit river sections in the Western Foothills, where the sedimentary rocks record the shift in sediment sources as Taiwan started to uplift. Before the collision started, sands and muds were delivered by long rivers from the Eurasian mainland onto a passive continental margin in a shallow marine to coastal environment. As the collision progressed, the sediment source shifted to the uplifting Taiwan mountain ranges, and the sediment delivered by short, steep rivers was deposited in a strait characterized by strong tidal currents which formed between the uplifting island and the Asian continent.



Shahin Dashtgard introducing the prograding tidal flats of the Late Miocene Nanchuang Formation in the Dahan River section by Yingge, northern Taiwan.

The second symposium was held at the Department of Earth Sciences (NCU), and featured two more keynote addresses. The first keynote was delivered by our local host, Prof. Andrew T-S Lin, who gave an overview of the formation of Taiwan and resulting strata. The final keynote address was given by Liz Hajek, Penn State University, USA, who explored how the interplay between sediment delivery and accommodation space influences the sedimentary structures preserved.

Speaker	**Convener: Ludvig Löwemark**
Andrew Lin	Welcome address
Liz Hajek	**Keynote**: Identifying climate signals in convergent margins: deconvolving signal, noise, and climate-tectonic feedbacks in tectonically active basins
Shahin Dashtgard	The linked sedimentologic-tectonic evolution of a forearc basin–forearc depression: Georgia Basin, Canada
YiSheng Tan	Sapropel, Cyclostratigraphy and Milankovitch cycles: Revisits of Pleistocene GSSPs
Michael Hren	**Keynote**: Organic molecular paleohypsometry: Promises, pitfalls and implications for the topographic evolution of the Taiwan orogen

Following the second symposium, the group headed south for the second field trip. They visited the spectacular badlands in Moon World, Tianliao, before crossing over to the East Coast. The Coastal Range, which stretches from Taitung in the south to Hualien in the north, consists of an uplifted volcanic island arc. In the sediments deposited on the sides of the volcanic islands, a record of the island arc gradually approaching and finally colliding with the Eurasian margin is preserved. Spectacular stops included the volcanoclastic rocks at Shitiping and overturned turbidites at Xiaoyehliu.



Tae Soo Chang on top of volcano-clastic layers at Shitiping, Coastal Range.

Our last day was spent on the NE Coast, where shallow marine strata from the past 30 million years or so expose snapshots of paleoenvironmental conditions of the different stages of the collision. For instance, at Yehliu Geopark we saw trace fossils that demonstrate how vertebrates such as stingrays hunted for shrimp and worms hiding deep in the sediment on the paleo-continental shelf.



The meeting attracted scientists from four continents. Here posing for the final group photo in front of the Candle Stick Rocks near Jinshan, NE Taiwan.

SPONSORS


SOCIETY FOR SEDIMENTARY GEOLOGY
100th
1926
2026
ANNIVERSARY


NSTC


COX
ANALYTICAL SYSTEMS


中華民國地質學會
Geological Society Located in Taipei


國立臺灣大學
敦品勵學・愛國愛人


國立中央大學


SEDIMENTOLOGY OF
CONVERGENT MARGINS
Taiwan April 26 - May 2
ABSTRACTS

Schedules

Symposium I – April 26th

Venue: Room 213, second floor, Department of Geosciences, National Taiwan University, Taipei

Start	End	Speaker	Title
08:45	09:00	Ludvig Löwemark	Welcome address and introduction to Taiwan
09:00	09:50	**Andrew Lin**	**Keynote**: Interplay between tectonics and sedimentation and its resulting stratigraphy of the Taiwan foreland basin: A review
09:50	10:05	Sung-Ping Chang	Millennial- to Centennial-Scale Sequence Stratigraphy in the Choshui River Subaqueous Delta, Offshore Taiwan
10:05	10:20	Tae Soo Chang	Wave-modulated, macrotidal open-estuary tidal bar facies at the Geum River estuary mouth, mid-western coast of Korea: resembling open-coast tidal flats
10:20	10:40	**Coffee Break**	
10:40	11:30	**Annette George**	**Keynote**: Basin Evolution and Paleozoic-Mesozoic terrane assembly in Northern Thailand
11:30	11:45	Zong-Dai Chen	Integrating Microfossil and Geochemical Evidence to Refine the Paleoenvironmental Understanding of the Szekou Formation in southern Taiwan
11:45	12:00	Chelsea Wong	Sedimentary Environment Evolution of the Maobitou Limestone on the Western Hengchun Tableland, Southern Taiwan
12:00	13:00	**Lunch**	
13:00	13:15	Zhonghao Zhang	The Role of Coccolithophore Deposition in Moving Suspensions: Importance of Flocculation and Its Implication for Modern and Ancient Calcareous Ooze (Chalk) Deposition
13:15	13:30	Juan José Ponce	Recurrence of hyperpycnites in the cenozoic of the foreland Austral Basin, Argentina
13:30	13:45	Milovan Fustic	Potential Genetic Relation of Coal-bearing Foreland and Pull-apart Basins of Central Kazakhstan and Carboniferous Pacific-type Convergent Margin System of the Paleo-Asian Ocean
13:45	14:00	Yechan Park	Three-Dimensional facies architecture and estuary–delta transition in a Holocene tide-influenced system, southern coast of Korea
14:00	14:15	Noelia Carmona (Juan Ponce)	Paleoenvironmental analysis of the Lower Cretaceous Río Mayer Formation (Austral Basin), Argentina

Symposium II – April 29th

Venue: S135 lecture room, Department of Earth Sciences, National Central University, Taoyuan

Start	End	Speaker	Title
08:45	09:00	Andrew Lin	Welcome address
09:00	09:50	**Liz Hajek**	**Keynote**: Identifying climate signals in convergent margins: deconvolving signal, noise, and climate-tectonic feedbacks in tectonically active basins
09:50	10:05	Shahin E. Dashtgard	The linked sedimentologic-tectonic evolution of a forearc basin–forearc depression: Georgia Basin, Canada
10:05	10:20	YiSheng Tan	Sapropel, Cyclostratigraphy and Milankovitch cycles: Revisits of Pleistocene GSSPs
10:20	10:40	**Coffee Break**	
10:40	11:30	**Michael Hren**	**Keynote**: Organic molecular paleohypsometry: Promises, pitfalls and implications for the topographic evolution of the Taiwan orogen
11:30	11:45		Open discussion
11:45	12:45	**Lunch**	

Participant roster

Noelia Carmona, Universidad Nacional de Río Negro

Sung-Ping Chang, National Cheng-Kung University

Tae Soo Chang, Chonnam National University

Zong-Dai Chen, National Taiwan University

Shahin Dashtgard, Simon Fraser University

Milovan Fustic, Nazarbayev University

Annette George, The University of Western Australia

Liz Hajek, Penn State

Michael Hren, University of Connecticut

Yi-Jen Lee, National Taiwan University

Andrew Lin, National Central University

Ludvig Löwemark, National Taiwan University

Yechan Park, Chonnam National University

Juan Ponce, Instituto de Investigación en Paleobiología y Geología (IIPG), CONICET

YiSheng Tan, National Taiwan University

Chelsea Wong, National Taiwan Uinversity

Zhonghao Zhang, Indiana University Bloomington

Paleoenvironmental analysis of the Lower Cretaceous Río Mayer Formation (Austral Basin), Argentina

Carmona, N.B.(1,2), Ponce, J.J.(1,2), Cevallos, M.(3), Jait, D.M.(4), Padva, D.(4), Cevallos, M.(3)

1 Instituto de Investigación en Paleobiología y Geología. Consejo Nacional de Investigaciones Científicas y Técnicas. Universidad Nacional de Río Negro. Av. Gral. Julio Argentino Roca 1242, R8332 Gral. Roca, Río Negro, Argentina. ncarmona@urnn.edu.ar

2 Universidad Nacional de Río Negro.

3 Universidad Nacional de San Juan.

4 Compañía General de Combustibles S.A. Gerencia de Exploración, Honduras 5663, CABA, Buenos Aires RC1414BNE, Argentina.

The Río Mayer Formation (Lower Cretaceous) is one of the units that accumulated during the first generalized marine transgression in the back-arc Austral Basin. This formation has been the subject of increasing study in recent years due to its potential as an unconventional reservoir. This study was conducted at Estancia Cristina locality, where this formation comprises a 647 m-thick succession, being the most complete section recorded up to now, for this unit. Four main facies associations have been recognized in this section. FA1 consists mostly of organic-rich mudstones, completely bioturbated, recording the highest TOC values (average 1.5%, maximum 2.17%). These deposits are interpreted as formed in an upper to lower offshore. FA2 is composed of massive marls due to bioturbation with the development of *Zoophycos* ichnofacies, abundant microorganism content, and minimum TOC values (0 to 0.5%). This facies association is interpreted as deposited on an inner shelf. FA3 consists of mudstones and heterolithic mudstones with the development of a *Cruziana* ichnofacies with components of the *Zoophycos* ichnofacies. TOC values range from 0.2% to 1.14%, and it is interpreted as formed in an inner shelf to upper offshore environment. Finally, FA4 comprises marlstones and laminated mudstones, with intercalations of very fine-grained sandstones, without bioturbation and showing the development of extensive levels of microbial mats. This facies association presents TOC values between 0.07% -1.15%, and it is interpreted as deposited in an upper offshore setting. Combined sedimentological, ichnological and geobiological analysis allowed us to infer that oxygen conditions may have fluctuated during the deposition of this unit which affected the establishment of benthos, and that the occurrence of microbial mats was most likely related to upwelling events with expansion of the OMZ, as it occurs in modern analogous.

Millennial- to Centennial-Scale Sequence Stratigraphy in the Choshui River Subaqueous Delta, Offshore Taiwan

Sung-Ping Chang[1], Bo-Hao Shih[1], Jheng-Syun Huang[1], Ho-Han Hsu[2], Yi-Ping Chen[2], Arif Mirza[2]

[1] Department of Earth Sciences, National Cheng-Kung University, Tainan, Taiwan
[2] Institute of Oceanography, National Taiwan University, Taipei, Taiwan

The Choshui (Zhuoshui) River is an ideal natural laboratory for studying source-to-sink sediment dynamics, owing to its exceptionally high sediment flux relative to its small (~3,000 km²) drainage basin and the presence of active faults. Despite its global significance as an end-member small mountainous river, the Holocene evolution of sediment delivery and its responses to climate variability and tectonic activity remain poorly constrained. The continuous offshore sedimentary archive provides a robust proxy for the upstream fluvial changes. In this study, we utilize high-resolution seismic reflection data (vertical resolution of ~decimeters) to decipher the stratal stacking pattern of the subaqueous delta during the Late Holocene, aiming to gain insights into the environmental parameters within the source-to-sink system.

The high-resolution seismic profiles extending from the river mouth to the offshore area reveal a compound subaqueous delta system, characterized by bathymetric and clinoform features. Based on key bounding surfaces, this subaqueous delta succession is subdivided into five distinct seismic units. Shore-parallel profiles exhibit pronounced onlapping geometries that track the north-south migration of the depocenter, suggesting a Late Holocene river avulsion. The estimated progradation direction is sub-parallel to the onshore transport direction of the Choshui River, indicating a primarily river-dominated setting, though longshore currents gained influence in pro-delta regimes.

Furthermore, analysis of the internal clinoform features resolves two distinct scales of variability. The longer-term cycles manifest as sigmoidal geometries with a concave-up trajectory, reflecting changes in sediment flux. In contrast, a shorter-period cycle is captured by abrupt progradation over every 5-10 m thickness, potentially representing a higher-order depositional sequence. Based on the independent age constraints onshore, preliminary estimates from these stratigraphic hierarchies yield average periodicities on millennial and centennial timescales, respectively. These estimates establish a stratigraphic framework against which future high-resolution dating and paleoclimate records can be tested, offering a rare sedimentary archive linking upstream forcing to offshore depositional response at sub-millennial timescales.

Wave-modulated, macrotidal open-estuary tidal bar facies at the Geum River estuary mouth, mid-western coast of Korea: resembling open-coast tidal flats

Tae Soo Chang, U-Seong Kim, Hun Jun Ha
Department of Geological and Environmental Sciences
Chonnam National University

Estuarine tidal bars are formed by the complex interplay of fluvial, tidal, and wave processes. Open estuary-mouth bars remain understudied compared to their inner-estuary counterparts. This study examines a lobate tidal bar at the Geum River estuary mouth, surrounding Yubu Island, where a central sand spit and coastal dune system bifurcate the bar into a seaward sand flat and a landward mud flat. While the seaward portion operates under a wave-tide mixed-energy regime, the landward section remains tide-dominated. Topographic surveys reveal a convex morphology, with a peak elevation of approximately 3.1 m above MHWL at the central portion, tapering off with gentle gradients. Grain-size analysis shows distinct trends: the sand flat exhibits unimodal frequency with minimal altitudinal variation, whereas the mud flat displays a bimodal, coarsening-upward succession. Seasonal dynamics are pronounced; in summer, mud content increases locally on the sand flat (by 41–90%), while the mud flat surprisingly experiences a 10–25% increase in sand content. Sedimentary facies analysis from box-cores reveals that the sand flat is characterized by hummocky cross-stratification (HCS) and wave ripples with mud drapes, which transition to tide-dominated structures such as current ripples with flaser bedding during summer. The central sand spit exhibits distinct beach facies with alternating heavy- and light-mineral laminations. The landward mud flat is dominated by lenticular bedding, with sand lenses thickening during the summer. The prevalence of wave-induced features and specific grain-size trends suggests that this open-estuary bar closely resembles open-coast tidal flats, with the intervening beach facies serving as a critical diagnostic marker for differentiating these depositional environments.

Integrating Microfossil and Geochemical Evidence to Refine the Paleoenvironmental Understanding of the Szekou Formation in southern Taiwan

Zong-Dai Chen[1], Tzu-Ruei Yang [2, 3, 4], Ludvig Löwemark [1]

[1.] Department of Geosciences, National Taiwan University, Taipei, Taiwan
[2.] Department of Life Sciences, National Chung Hsing University, Taichung, Taiwan
[3.] Department of Earth Sciences, National Cheng Kung University, Tainan, Taiwan
[4.] Department of Geology, National Museum of Natural Science, Taichung, Taiwan

The abundant fossil assemblages within the Late Pleistocene Szekou Formation (Hengchun Peninsula, southern Taiwan) suggest a semi-open to open lagoonal system sheltered by barrier islands. However, paleoenvironmental interpretations have long been hindered by dating limitations and uncertainties regarding the spatiotemporal distribution of fossils. While the formation's age is broadly constrained to 30,000-260,000 years, the specific depositional conditions of its fossiliferous intervals remain unclear.

The discovery of a whale skeleton—over 70% complete—offers a unique opportunity to refine the environmental framework of the Szekou Formation. By integrating sedimentological characteristics with molluscan and foraminiferal assemblage analyses, this study reconstructs the paleoenvironmental conditions and constrains the whale-bearing interval to the lowermost part of the Szekou Formation.

Foraminiferal assemblages and planktic/benthic (P/B) ratios indicate fluctuating paleobathymetry between 10–100. The dominance of suspension-feeding bivalves (66%) reflects abundant particulate organic matter (POM) and suggests a productive coastal environment. Together, these results indicate that the paleo-lagoon provided ecological niches favorable for large marine vertebrates. Coarse-grained sediments surrounding the whale fossils, paired with geochemical proxies (C/N ratio: 20.6–23.0; δ13C: –22.4 to –22.9‰), indicate episodic terrestrial organic matter input. These signatures provide critical insights into the taphonomic conditions contributing to the exceptional preservation.

By combining stratigraphically continuous core materials, stable isotope ratios, and fossil assemblages, this study reconciles previous discrepancies. It clarifies the environmental conditions of the whale's death, the depositional settings favoring its preservation, and the stratigraphic framework of its occurrence.

The linked sedimentologic-tectonic evolution of a forearc basin–forearc depression: Georgia Basin, Canada

Shahin E. Dashtgard, Chuqiao Huang, Maziyar Nazemi, and Francyne Bochi do Amarante

Applied Research in Ichnology and Sedimentology (ARISE) Group, Department of Earth Sciences, Simon Fraser University, Burnaby, British Columbia, Canada V5A 1S6

The Georgia Basin, Canada and USA has been studied extensively as it records the tectonic evolution of western North America from the Late Cretaceous to today. However, most studies of Georgia Basin strata focused on limited outcrop exposures of Upper Cretaceous strata and this led to the acceptance of a relatively simplistic view of the basin's evolution. Recent studies integrating outcrop and core-based stratigraphic descriptions, 2D seismic, well logs, detrital zircon, and biostratigraphy reveal a complicated depositional history that records both syn-tectonic activity and post-deposition deformation. The fill of the Georgia Basin exceeds 7 km at its deepest point and evidence of syn-sedimentary uplift is recorded in stratigraphic architectures from the Upper Cretaceous through to recent with a general NE-SW trend to structural elements. The strata comprise sediment derived mainly from the adjacent Coast Plutonic Complex.

There was a major shift in depositional environments and drainage patterns from the Late Cretaceous to the Eocene that corresponds to the docking of Siletzia Terrane on North America's western margin. During the Late Cretaceous, sedimentation in the Georgia Basin occurred in deepwater with westward-flowing turbidites. In the Eocene through the Miocene, uplift of the forearc high (Vancouver Island) protected the interior of the Georgia Basin, which was dominated by south through westward flowing rivers in a terrestrial to coastal plain setting. Uplift of the forearc high marked the evolution of the Georgia Basin from a forearc to a forearc depression. The stratigraphic record of the Georgia Basin reveals the close linkage between tectonic activity along North America's active margin and sedimentation responses in the adjacent basin. The Georgia Basin is an example of how a forearc basin can evolve through several different geometries in response to regional tectonic events, and highlights the need to resolve how basin architecture is tied to local tectonic regime.

Potential Genetic Relation of Coal-bearing Foreland and Pull-apart Basins of Central Kazakhstan and Carboniferous Pacific-type Convergent Margin System of the Paleo-Asian Ocean

Milovan Fustic, Yerkebulan Tazabek, Amir Umralin, George Mathews, Mahmoud Leila, Kamal Regmi, and Antoine Dillinger

Nazarbayev University

The geology of Central Kazakhstan comprises a complex assemblage of Proterozoic to Late Paleozoic magmatic, volcanic, and sedimentary successions. The Carboniferous strata hosts Kazakhstan's two largest coal-producing basins, Karaganda and Ekibastuz. The erosional remnants of their age-equivalent ophiolites, basalts, and intrusions, interpreted as Paleozoic intra-oceanic arc formed along a Pacific-type convergent margin are exposed in the Itmurundy, Tekturmas, Zharma, and Char hills. These Late Paleozoic rock-units represent the final accretionary stage of the Neoproterozoic–Late Paleozoic accretionary complex known as Central Asian Orogenic Belt (CAOB), one of the largest and most complex accretionary orogens on Earth.

While the architecture of the paleo-arc orogen is well documented, far less is known about the coeval fold and thrust belt and foreland basin including their sediments. The reasons include: i) poorly preserved rock record as majority of sediments were subsequently reworked; ii) The Karaganda Basin (~3,000 km²) and Ekibastuz Basin (<250 km²) despite decades of large-scale mining exploitations, are lacking modern basin-analysis, provenance, and sedimentological studies.

Examples of our evidences of these basins' potential genetic relation with the Late-Devonian – Carboniferous subduction of the Paleo-Asian Ocean under Kazakhstania plate include:

1. Coeval processes behind two distinct basin types: Karaganda and Ekibastuz basins are characterized by different tectono-stratigraphic framework. The Karaganda (<5km deep wedge-shaped) foreland basin contains dozens of thin (o.5-6m thick) liptinite-free coal seams separated by fluvio-deltaic facies associations; Ekibastuz continental pull-apart basin, contains laterally and vertically dislocated strata within graben-syncline depression and hosts tens of meters thick liptinite-rich coals. The analogy with Pacific-type convergent margin system suggests that these 250km apart from each other coeval basins are most likely simultaneous product of the same oblique arc-continent collision.

2. Syn-depositional volcanic ashfalls: Although volcanic ash is typical of convergent-margin systems, it has not been documented in the Carboniferous basins of Central Kazakhstan. In the Ekibastuz mine, eight suspected tuff layers, each up to 0.5 m thick, are currently being analyzed to determine their provenance and age. These data will help constrain the frequency of explosive volcanism and may guide the search for ash-fall layers in coeval offshore carbonates, where they

could have contributed to supergene copper enrichment.

Strong similarities between CAOB tectonic elements and Karaganda and Ekibastuz basins with the modern convergent-margin accretionary orogen and basins of Taiwan suggests that modern system studies may improve the reconstruction of the Central Kazakhstan's paleo convergent-margins, supporting resource exploration efforts.

Basin Evolution and Paleozoic-Mesozoic terrane assembly in Northern Thailand

Annette George

School of Earth and Oceans, The University of Western Australia

Multiple models have been proposed for amalgamation via collision and accretion of the continental terranes that make up Thailand and neighbouring countries, generating significant debate despite much work over many decades. Geological complexity reflects the collisional events of the Permo–Triassic Indosinian Orogeny, overprinted by the subsequent Himalayan Orogeny. Tropical marine conditions along the (now) western margin of Indochina led to extensive development of Pennsylvanian–Mid Permian mixed carbonate–siliciclastic platforms that are exposed in the Loei-Phetchabun Foldbelt in NE Thailand and intersected by petroleum wells in the deformed subsurface basins beneath the Khorat Plateau. Stratigraphic analysis, carbonate sedimentology and biostratigraphy have been useful for reconstructing stratal architecture in the foldbelt, building on well-described shallow inner platform facies and extensive paleontological work. Interpreting platform evolution has been enhanced by recognition of significant framework-builders, representing outer ramp biostromes and low-relief biostromes, and patch reefs/mounds (platform margin to upper slope deposits) as has recognition of widespread mixed carbonate-siliciclastic slope deposits that link the well-known platform facies with coeval deep basinal deposits. Important tectonic events in platform/basin evolution have been highlighted by detrital zircon provenance data from siliciclastic units and crystallization ages of igneous units recording subduction-related magmatism. The Uttaradit-Nan Suture Zone, located between Indochina and the Sukhothai Arc, has long been considered enigmatic in the collisional history and suturing of Indochina and Sibumasu terrane. Within this suture zone, studies focusing on the Nan Basin have been limited. Detrital zircon geochronology highlights provenance variations across the basin and, in combination with igneous crystallisation ages, supports a back-arc basin origin. Maximum depositional ages constrain timing of closure of the Nan Basin to middle Late Triassic and this timing then also records collision and amalgamation of the Sukhothai Arc and Indochina.

Identifying climate signals in convergent margins: deconvolving signal, noise, and climate-tectonic feedbacks in tectonically active basins

Liz Hajek

Penn State University

Convergent margins can preserve critical information about climate-tectonic coupling and mass fluxes from terrestrial to marine systems. However, complex interactions among sediment supply, accommodation creation, and landscape dynamics on convergent margins make these settings inherently challenging for interpreting the sedimentary record of climate change. Here, we use numerical modeling approaches to explore how coupled feedbacks among tectonics, climate, and sediment-transport systems shape the sedimentary record of climate change on active margins. At the largest scales, a simplified mass-balance model that includes climate-sensitive sediment-transport thresholds shows how, under the same tectonic conditions, wet vs. dry settings record cyclic climate changes in different ways. Margins experiencing climate variability that crosses sediment-transport thresholds can preserve climate signals as identifiable facies changes. In contrast, margins that are either wetter or drier, and are therefore farther from sediment-transport thresholds, instead preserve climate signals as subtle shifts in grain size or shoreline position. At a landscape scale, autogenic sediment-transport dynamics can obscure, overprint, or "shred" climate signals recorded by, for example, geochemical proxies. Stochastic landscape models provide guidelines for overcoming this sedimentary signal shredder through increased sampling. We show that complete paleoclimate records may be recoverable – even in noisy depositional systems – by building composite records from multiple individual records (e.g., outcrop sections or cores) that sample a paleo landscape. Together, these results offer tools for assessing the sensitivity of an active margin setting to record climate change and provide guidelines for study design and sampling to maximize the recovery of paleoclimate signals in deposits from convergent margins.

Organic molecular paleohypsometry: Promises, pitfalls and implications for the topographic evolution of the Taiwan orogen

Michael T. Hren

University of Connecticut

Understanding how mountain belts grow through time requires robust constraints on past topography, yet paleoelevation reconstructions remain challenging in humid, high-relief settings. This talk highlights the application of organic molecular paleohypsometry, a biomarker-based approach that uses the hydrogen isotope composition of fluvially-exported plant leaf waxes to reconstruct catchment-scale elevations, and demonstrates its power for constraining the geomorphic and topographic evolution of active orogens. Because leaf waxes record the hydrogen isotope composition of precipitation during biosynthesis and are transported and integrated across drainage basins, their isotopic signatures preserved in sedimentary archives provide a catchment-averaged record of organic source elevation that is applicable across a wide range of climates and depositional environments. The talk will address key controls on molecular isotope production, transport, and integration, including biomass distribution, erosion efficiency, and sediment routing, and outlines a general framework for applying organic molecular paleohypsometry to other mountain systems worldwide. Finally, this talk will integrate recently published and new Pliocene to recent organic molecular records from eastern Taiwan which provide key constraints on the topographic evolution of the Central Range of Taiwan. Organic molecular isotope data capture significant increases in the mean catchment elevation of river networks draining both southern and central eastern Taiwan in the last ~1.7 Myr and highlight the acceleration of topographic growth along the length of the orogen through the Pleistocene.

Three-Dimensional facies architecture and estuary–delta transition in a Holocene tide-influenced system, southern coast of Korea

Yechan Park

Department of Geological and Environmental Sciences, Chonnam National University

While tectonic uplift, subsidence, and volcanism are primary controls on sedimentation in convergent-margin forearc, backarc, and foreland basins, the evolution of estuarine and coastal systems in tectonically stable settings is predominantly governed by non-tectonic factors, such as climate-driven relative sea-level (RSL) fluctuations and sediment supply rates. In this study, we present the Holocene sedimentary record of a tide-influenced estuary–delta system developed along the southern coast of Korea, and document the facies architecture and stratigraphic evolution pattern of an epicontinental coastal shelf at the marginal sea. Based on sedimentary facies analysis of 6 borehole cores, along with 63 radiocarbon and 14 OSL ages, we identified 27 sedimentary facies grouped into five depositional units: tidal bar (DU1), mudflat/mixed flat (DU2), central bay (DU3), delta front (DU4), and mouth bar (DU5). Stratigraphically, the area exhibits a rapid transition from an estuarine to a deltaic system during the late Holocene. This evolution was primarily driven by RSL fluctuations, variations in sediment supply, and tidal reworking, rather than tectonic subsidence. Specifically, we demonstrate the three-dimensional evolution of the estuary along-strike and down-dip directions, revealing that distinct facies architectures and evolutionary patterns can coexist within a single system where tidal and fluvial processes operate together. These findings suggest a progressive evolution of the estuary–delta transition in tectonically stable settings, contrasting with sedimentary models from active convergent-margin basins where episodic structural forcing dictates sedimentation.

Recurrence of hyperpycnites in the cenozoic of the foreland Austral Basin, Argentina

Juan José Ponce, Noelia Carmona
Instituto de Investigación en Paleobiología y Geología (IIPG), CONICET, Av. J. A. Roca 1242, 8332, General Roca, Argentina.
Universidad Nacional de Río Negro, Instituto de Investigación en Paleobiología y Geología, General Roca, Argentina.

The Cenozoic deep marine deposits of the foreland Austral Basin in Tierra del Fuego, Argentina, show a high frequency of hyperpycnites in their stratigraphic record. The hyperpycnites are density currents produced by river floods, which develop internal arrangements that cannot be modeled by applying the classical turbidite analysis. The sedimentological and ichnological characteristics exhibited by hyperpycnites result from a complex interaction between the morphology of the basin, the duration of the discharges, the fluctuations in flow velocity, and the contribution of fresh water to the basin. These characteristics result in the accumulation of deposits of variable thicknesses, characterized by: 1- a transitional passage, both vertically and laterally, of aggradational and tractive sedimentary structures, which may include granulometric changes and reactivation surfaces, 2- the abundant concentration of particulate organic matter (phytodetritus), and 3- the absence or scarcity of trace fossils, with the development of impoverished ichnofacies. The unusual occurrence of hyperpycnites in the Cenozoic of the foreland Austral basin of Tierra del Fuego is related to its configuration and tectonic evolution. The configuration of the basin, consisting of a supply area (uplifted orogen) close to the accumulation zone and separated by a very narrow transfer area, favored the generation and acceleration of density flows genetically linked to river discharge systems. Tectonic evolution generated two well-defined fill geometries. A ramp system linked to a compressive tectonic regime that ended approximately in the Middle Miocene, which led to the development of a system of prograding clinoforms from the NE. These geometries produced different architectural elements that controlled the distribution of the main sand wedges. The hyperpycnites linked to the ramps are represented by lobe systems fed by small channels of moderate to high sinuosity, while the hyperpycnites associated with the clinoform systems show lobe deposits fed by small channels of high sinuosity in topset positions, and larger channels of low sinuosity at the toe.

Sapropel, Cyclostratigraphy and Milankovitch cycles: Revisits of Pleistocene GSSPs

YiSheng Tan, Ching-En Li, De-Cian Chen, Hao-Ting Yu, Hsing-Yi Yao, & Jih-Pai Lin

National Taiwan University

The Global Boundary Stratotype Section and Point (GSSP), commonly referred to as the "golden spike," is a geochronological standard established to provide a globally consistent reference framework for stratigraphic correlation. The Mediterranean region preserves a continuous marine stratigraphic record from Pliocene to Holocene, particularly characterized by the alternating occurrence of marls and sapropels. The formation of Mediterranean sapropels is generally attributed to intensified Northern Hemisphere summer insolation driven by precession, which strengthened the African monsoon. The resulting increase in freshwater input reduced or even halted thermohaline ventilation, leading to oxygen depletion in bottom sea water and thereby suppressing organic matter decomposition. The marl-sapropel successions are then can be calibrated and astronomically tuned to Milankovitch cycles. The coding scheme of Mediterranean Precession-Related Sapropels (MPRS), for example, further enhances their potential for global stratigraphic correlation. Among these, the top of sapropel 'e' (MPRS 176) in the Vrica Section of Calabria, southern Italy, defines the GSSP for the Calabrian Stage, and it also formerly served as the lower boundary of the Quaternary. The revised base of the Quaternary is now defined at the top of the Nicola Bed (Mediterranean Precession-Related Cycle 250) in the Monte San Nicola section, southern Sicily. During this field trip, four GSSP localities in southern Italy: the Heraclea Minoa section (Zanclean Stage), Punta Piccola section (Piacenzian Stage), Monte San Nicola section (Gelasian Stage), and Vrica section (Calabrian Stage) were visited. Samples were collected from sapropel A5 (the chronological equivalent of the Nicola Bed) and the overlying marl. In addition, samples were collected from sapropel 'e' at the Vrica section and the overlying marl.

In term of stratigraphic correlation of Taiwan, the Cholan Formation, owing to the high subsidence and high sedimentation rates of the foreland basin setting in which it accumulated, preserves sea-level changes related to Milankovitch cycles. Recent studies have shown that its stratigraphic cyclicity was influenced by variations in Northern Hemisphere insolation driven jointly by obliquity and precession, suggesting a potential comparability with Mediterranean sapropels, which are likewise linked to precession. By integrating the Mediterranean sapropel framework with existing studies on calcareous nannofossils, magnetostratigraphy, and sequence stratigraphy in the Cholan Formation, it may be possible to identify both the former and current lower boundaries of Quaternary within the Cholan Formation, and to further investigate the influence of Milankovitch forcing and related temporal lags recorded in this succession.

Sedimentary Environment Evolution of the Maobitou Limestone on the Western Hengchun Tableland, Southern Taiwan

Chelsea Wong[1], J. Bruce H. Shyu[1], Shih-Wei Wang[2], Kai-Shuan Shea[3]

[1.] Department of Geosciences, National Taiwan University, Taipei, Taiwan
[2] Geology Department, National Museum of Natural Science, Taiwan
[3] Geological Survey and Mineral Management Agency, Ministry of Economic Affairs, Taiwan (retired)

The Hengchun Limestone is an important Quaternary stratigraphic unit in Taiwan, formed offshore the Hengchun Peninsula and uplifted above the sea level during the Penglai orogeny. Although most lithostratigraphic units in the Hengchun Peninsula have been studied, the Maobitou Limestone, a distinctive part of the Hengchun Limestone, has received comparatively little attention. Located at one of the southernmost tips of Taiwan, this unit recorded critical paleoenvironmental information for refining stratigraphic frameworks of the Hengchun Peninsula. The only previous study (Li, 1992) on the Maobitou Limestone proposed its sedimentary environment to be an open shoreface dominated by wave and tidal processes, based on sedimentary structures that were interpreted as large-scale trough, low-angle planar, and herringbone cross-stratifications. However, hummocky cross-stratification (HCS) occurs frequently within this coarse-grained unit, inconsistent with this interpretation.
This study examines the Maobitou Limestone through field investigations at 16 coastal outcrops. Three major lithofacies associations were identified: (a) bioclastic packstone facies; (b) bioclastic packstone-grainstone facies; and (c) bioclastic grainstone facies. We interpreted the limestone as a storm-dominated deposit based on six taphonomic indicators: (T1) graded grains within amalgamated beds with HCS; (T2) high abrasion of large bioclastic shell layers; (T3) mixing of planktonic and benthic shell assemblages; (T4) reworked carbonate grain redeposition; (T5) manganese oxide precipitation; and (T6) intensely bioturbated beds beneath HCS. A newly obtained 70-m drill core is also integrated with stratigraphic columns from outcrops, enabling more robust stratigraphic correlation. We also incorporated new

biostratigraphic age determinations to establish a temporal framework for the evolution of sedimentary environments. Through these results, we reconstructed the depositional history of the Maobitou Limestone, and provide a foundation for future correlation between adjacent limestone units across the Hengchun Peninsula. These new data would also have broader implications for Quaternary geological evolution in southern Taiwan.

The Role of Coccolithophore Deposition in Moving Suspensions: Importance of Flocculation and Its Implication for Modern and Ancient Calcareous Ooze (Chalk) Deposition

Zhonghao Zhang

Indiana University Bloomington

Coccolithophores, a group of calcifying phytoplankton, are among the most productive carbonate producers in the oceans. Their remains accumulate to form chalk deposits, which provide unique archives of Earth's geological history. Previous studies have commonly interpreted chalk as a semi-pelagic to pelagic deposit, settling slowly to the seafloor by suspension. Laminated chalk, in particular, has traditionally been explained by meter-scale Milankovitch-paced fluctuations in bottom-water oxygenation, with lamination attributed to intervals of reduced benthic activity under low-oxygen conditions. However, growing sedimentological and ichnological evidence suggests that this interpretation is insufficient. For example, shale was once considered to form exclusively in quiet-water environments, yet physical experiments have demonstrated that fine-grained sediments can aggregate into flocs capable of being transported as bedload. Recent microfacies analyses further indicate that laminated chalk is a product of bottom-current activity. In this study, we use a large racetrack flume facility to conduct physical experiments aimed at understanding the physicochemical properties of coccolithophores and their transport and depositional behavior. Specifically, we investigate the mechanisms of coccolithophore flocculation and quantify the critical velocities required for sediment transport and deposition. Our results demonstrate that bottom-water reworking processes play a key role in the formation of laminated chalk, thereby providing direct insights into pelagic and hemipelagic sedimentary processes.

Itrax Core Scanner description and data sheet

The Itrax Core Scanner™ determines the variation of all elements from Mg to U along wet as well as dry cores. It offers very high speed of analysis combined with high sensitivity, variable analytical step size and non-destructive scans. The sensor range includes a unique combination of XRF and X-ray radiography, plus high-quality sample images and magnetic susceptibility. Typical applications include paleoclimate and paleoenvironmental reconstruction, lacustrine and marine sediment studies, quaternary geology, cyclostratigraphy and varve analysis ,core correlation and composite sequence construction, drill-core characterization, sedimentology and stratigraphic interpretation

Main benefits

- A unique combination of XRF scanning and X-ray radiography, plus RGB camera and Magnetic Susceptibility in one fully position-calibrated system.
- Very fast XRF scanning at any step size while maintaining high data quality, from centimeter scale and all the way down to sub-millimeter analyses.
- Provides excellent preservation of sensitive samples through non-contact scanning combined with very high analytical speed.
- Measurement of all detectable elements simultaneously in a single scan.
- Excels in proxy studies thanks to very high precision in peak-area determination combined with high sensitivity across a wide range of elements.
- Provides uniquely strong positional precision and repeatability, making it ideal for spliced records and high-resolution stratigraphic studies where position precision is crucial.



Itrax Core Scanner samples are inserted in the left wing, and automatically moved during scanning. The user sets the scan parameters from the computer, and can then leave the instrument to apply the measurements unattended.

- Gives users extended control of the analytical process through easy access to the XRF spectrum from every analytical point.
- Is the leading XRF scanner for sediments examinations worldwide, supported by a large installed base and with extensive scientific publication output of over 200 scientific articles published yearly.
- Is the preferred choice for labs requiring both maximum throughput and the highest performance at millimeter and sub-millimeter resolution.
- Only Itrax Core Scanner maintains the same high data quality per unit time across all resolutions from centimeter scale down to 0.1 millimeter.

Features

The Itrax Core Scanner™ can scan both wet and dry cores. It offers high sensitivity across a wide elemental range, including the elements commonly used in sediment proxy studies as well as rare earth elements (REEs). The analytical step length can be easily adjusted in the software to meet different resolution requirements, while ensuring continuous coverage over the full step interval and sample length. This makes Itrax equally well suited to rapid sample overviews and high-resolution detailed scans.



This photo shows a split sediment core sample in a liner being placed in the Itrax Core Scanner. The long sample holder allows for all standard core lengths and is easily accessible. All scanning can be performed with or without a foil covering the sample surface, as chosen by the user.

Compatible sample types include wet cores, rock drill cores, slabs, U-channels, peat, cave stones, etc. As long as the samples are reasonably flat, the Itrax follows the surface and automatically adjusts the measurement to a constant distance over the surface.

Only the Itrax scanner family can perform XRF scans that cover all elements, from the lightest to the heaviest, in a single pass.

Itrax does not make direct contact with the sample surface during scanning, but analyzes it from a fixed, close distance.] The advantages include:

- No deformation of soft sediment samples
- The risk of forming a water film between a wet sample and an applied XRF foil is minimized, since no pressing on the film occurs.
- Drying or deformation of the sample between scans is avoided, as can occur in multi-pass scanners that touch the surface.
- Total scan time is minimized by eliminating the need for vertical up-and-down movement at each analytical step.

The combination of XRF and X-ray radiographic imaging enables detailed identification of laminae and clear differentiation between stratigraphic layers and individual particles. This, plus the uniquely precise steps positioning along the sample provides an indispensable examination tool for high-resolution core analysis.

Itrax Core Scanner™ **excels** in rapid analysis, with performance that has been continuously improved over the years. This high speed is enabled by several features, including the high-power X-ray tube, the very short time between analytical steps, the non-contact measurement principle, and the unique Itrax capability to determine all elements simultaneously at a single voltage. Together, these features reduce scan time to only a fraction of that required by other XRF scanners, without compromising detection limits, quantitative precision, or reproducibility.

Itrax Core Scanner™ provides consistently high analysis speed at every measurement point, regardless of the selected analytical resolution, from centimeter scale down to sub-millimeter resolution This unique capability can save substantial scan time, especially when analyzing long samples at millimeter-scale steps or smaller. [The very short time between analytical steps further minimizes total scan time, helping to reduce the time wet samples remain at room temperature.

The digital X-ray radiography system transfers X-ray transmission images directly to the computer. Its advanced design is intended to reveal very small variations in density and chemical composition. X-ray radiography is an ideal complement to the XRF data, helping you verify whether a XRF peak is to be interpreted as, for example, a pebble or as a stratigraphic layer.

The magnetic susceptibility add-on sensor requires contact with the sample surface and is therefore used as the final step in the measurement sequence, when included.

Itrax Core scanner offers uniquely high precision and repeatability in sample positioning, ensuring reliable data at every point, which is crucial, for example, for spliced cores.

The high-quality RGB camera in today's Itrax scanners is equipped with crossed polarizing filters that reduce glare from wet surfaces as well as other surface features that scatter light. The result is high-quality images that reveal details more clearly than the naked eye. The high image quality also enables effective contrast enhancement.

All sensors are position-calibrated relative to one another and operate during scanning with high precision.

Continued on next page

Software ecosystem

The software package is developed by Cox and supports the full analytical workflow from acquisition to data review and interpretation.

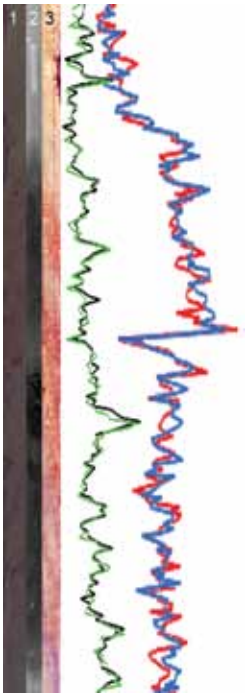
Itrax Navigator, our software for instrument operation and data display during scanning.

Q-spec, an advanced software package for display of spectra and automated extraction of peak areas for each element, from the x-ray spectra. It separates peaks from background noise and gives you net element peak areas. It also identifies and separates overlapping peaks and identifies sum peaks and diffraction peaks if such appears. It can calculate element concentrations by a simple click, is based on the Fundamental Parameter method and delivers good data from a uniquely wide range of sample matrices with one calibration. Calibrations with other standard samples will only be needed for odd matrix compositions. Another unique Q-spec feature is determination of the average atomic number in the sample volume, including the elements that are too light to detect with the XRF. This adds further precision to the calculations of element concentrations. The Qspec generates a summary file containing all data from each measurement step together with a note that indicates whether each analysis is correct. This puts the user in control of the analysis at every step. Incorrect data can e.g. be due to the appearance of an unexpected element appearing. XRF spectra from each analytical point is automatically stored for easy user access, review and re-processing.

The ReDiCore software is for display and presentation of element profiles, radiographic images, magnetic susceptibility data, and sample photos together.

The BoreHole Viewer offers data display and interactive examination of whole boreholes, compiling data from several core scans.

The data can be moved seamlessly between the different software apps as well as into e.g. Excel.



This photo shows a 0.1 m. section of a sediment core. Part 1. is the core section as seen by eye. Part 3. been contrast-enhanced. Part 2. in the center is the radiographic image. To the right are four graphs from the XRF scan, showing the variation in concentration along this sample section. The red and the blue graphs show Silica distribution from two consecutive scans. The green and the black graphs show the two Manganese profiles from the two scans. ***Please note the very good repeatability in peak position as well as peak size*** (arbitrary scale). *Measuring time was only 1 second at each position, with 0.2 mm steps. Extending the time improves the precision further. The average Si concentration was ~10%, and Manganese ~0.07%. This core was sampled off Greenland in 2012. Data with courtesy of Dr. R. Gyllencreutz, Stockholm Univ.*

Detection limits

Itrax Core Scanner detects all elements across the whole range Mg-U. High sensitivity, well-defined peaks, and high reproducibility for most metals provide the precision needed for confident use of element ratios in proxy studies.

The table lists the Detection Limits for selected elements of common interest. These values are examples spanning light to heavy elements within the full range detectable by this scanner.] The first value for each element shows the detection limit using a Cr anode x-ray tube, which has higher sensitivity for light elements. The second value is the value when applying a Mo tube, offering somewhat better sensitivity for the heavier elements. As a third alternative, a Rh anode x-ray tube can be applied when Mo is of special interest together with other heavier elements (not listed, but available on request). The reference material used is NIST610, measured at 100 seconds, applying the standard scientific model for calculations. Please contact us if you would like information about some element not listed.

Element	PPM	Element	PPM	Element	PPM
Mg	2230/-	V	16/12	Ba	9/51
Al	4089/575	Mn	24/9	Cd	3/144
Si	217/1249	Fe	24/9	La	15/47
P	104/465	Br	11/8	Hf	21/51
S	56/204	Rb	12/9	Hg	28/15
K	10/36	Sr	13/9	Pb	25/14
Ca	7/25	Zr	15/73	Th	28/16
Ti	2/14	Mo	14/184	U	35/19

Specifications

Function/Parameter	Value/Description
XRF scans and data	Maximum count rate of the XRF detector, up to >300,000 cps, allowing for very fast analyses. Better than 133 eV FWHM at 5.9 keV, at any count rate peak width, for best element peak separation. Typical time setting is 3 (1-10) sec. per scan step for a marine sediment total time per analytical step, covering all detected elements. The time between each measurement step is only a fraction of the time needed in scanners that use up/down movement between each step. The XRF spot size is 0.2 mmx8mm (8mm XRF scan width) as standard, with sharp edges, (0.1mmx8mm beam size optionally).
X-ray radiography	Digital radiography with data fed straight into the computer, resolving variations in sample chemistry and density down to ~0.5%. Image width is ~20 millimeters. Maximum sample thickness depends on composition (~60 mm for a typical marine sediment).
Magnetic Susceptibility	Bartington MS2E type, having a measuring spot of ~4x10mm. Touches sample surface (add-on).
Optical images	High quality RGB images, ~50 micrometer pixel size, an image width of about 100 millimeters, and user selected length along the core. Glare in wet sample photos is minimized by the included crossed polarizing filters.
X-ray Beam	Well defined x-ray beam with 0.2mmx20mm (optionally 0.1mmx20mm) with sharp edges and even intensity distribution. This makes small step analyses down to 0.2/0.1 mm just as fast as larger steps. Larger steps are implemented by sweeping over the selected step, without information loss. Enhanced intensity by Polyflat™ x-ray waveguide speeding up analyses for higher sample throughput.
Scanning steps	Any step from full sample length down to 0.01 millimeter, offering the best available precision in scan step positioning. Allows for continous scanning without loss of any information along a sample, as well as fast overview by “jumping” between positions at selectable jump length.
Element range and X-Ray tubes	Most users use only one tube type, but Cr, Mo and Rh anode tubes are available as alternatives, depending on elements of most interest for the user. The range is Mg – U for a Cr tube, and Al-U for Mo and Rh tubes. Each tube covers the whole respective element range, with detection limits as described under Detection limits section above. The tubes are easily shifted in ~15 minutes. These high power x-ray tubes are operated at 1650 W for high performance analyses. You are welcome to contact us in case you want more details.
Sample dimensions	Up to 1800 (L) x 122 mm Ø split core / 66 mm full core.
Instrument size and weight	4500 x 820 x 1570 mm LxWxH, ~1100 Kg.
Quantitative calibration	The State-of-the-art element quantification software is pre-calibrated and covers a very wide range of sample matrices. More standards can be added but are only needed for odd sample compositions.
Safety Registration	Ch-08425/S, in Swedish Radiation Safety Authority, plus approved for use in many other countries. The radiation level is below 0.5 µSv/h, allowing for work close to the instrument without limitations.

All specifications and all information in this document are subject to improvements, changes and updates. Please contact us if you want more information.

COX ANALYTICAL
Cox Analytical Systems www.coxsys.se phone: +46 708 3660 info@coxsys.se

Itrax FleXRay XRF Scanner description and data sheet

The ItraxFleXRay XRF Scanner™ determines elemental variations from Na to U along both wet and dry cores. It combines very high analytical speed with high sensitivity across the full elemental range, variable step size, and non-destructive scanning. Typical applications include paleoclimate and paleoenvironmental reconstruction, lacustrine and marine sediment studies, quaternary geology, cyclostratigraphy and varve analysis ,core correlation and composite sequence construction, drill-core characterization, sedimentology and stratigraphic interpretationThe sensor range includes high- quality sample images, magnetic susceptibility and spectrometer options.

Main benefits

- Itrax FleXRay™ combines high-performance XRF scanning with high-quality RGB imaging and, as optional add-ons, magnetic susceptibility and spectrometers in different spectral ranges, with all sensors calibrated to matching lateral positions.
- Itrax scanners offer exceptionally high scanning speed while maintaining high data quality.
- Itrax scanners preserve samples through non-contact scanning and maintain high analytical throughput and data quality in a unique way, even at step sizes down to 1 mm.
- Particularly well suited to proxy studies thanks to high precision in peak-area determination, good sensitivity across a wide range of elements, and precise lateral positioning of the data.
- This XRF scanner delivers high analytical speed without physical contact with the sample. It is especially strong in combining speed and analytical quality at any resolution down to millimeter-scale, and can also be configured for sub-millimeter analytical step sizes.



Itrax FleXRay Scanner offers superb performance, and excels in fast scanning, good sensitivity for a very wide range of elements, combined with cutting edge quantitative capacity.

- Gives the user strong control of the analytical process through easy access to the XRF spectrum from each analytical point.
- Provides high precision in sample positioning at each analytical point, helping ensure that every data value is associated with the correct location.
- Itrax FleXRay Scanner™ is part of the Itrax family of XRF scanners for sediments and drill cores, with installations worldwide and data represented in well over 2,000 scientific publications and a yearly groth in number of articles with more than 200.
- Itrax FleXRay Scanner is well suited to proxy studies because it analyzes a wide range of elements from Na to U with high precision, sensitivity, and variable lateral resolution. Furthermore, all elements are determined in the same XRF scan, under the same analytical conditions, eliminating time-consuming rescans at other voltages and reducing the need for frequent recalibration to normalize data between analytical points.

Features

The FleXRay Scanner is a highly useful instrument for preliminary analysis of both wet and dry cores It offers high sensitivity across a wide element range, with user-selectable step sizes to accommodate different resolution requirements.

Different sample types can be scanned, including wet cores, rock drill cores, slabs, U-channels, peat, cave stones, and related sample types.. As long as the samples are reasonably flat, FleXRay follows the sample surface to provide accurate and reproducible analytical data.

Itrax FleXRay is available in two versions: one for both wet and dry samples, and one optimized for dry samples such as drill cores.



The pull-out sample holder makes it convenient, quick and safe to switch samples, whether these are sediments in liners or drill cores.

High sample throughput is a key feature, enabled by fast XRF measurements and very short overhead time between analytical points.

This high scan speed is especially advantageous for high-resolution scanning while still maintaining excellent detection limits, precision, and reproducibility at a typical analysis time of 3 seconds per analytical step. Several features contribute to this performance, including the Cox proprietary X-ray beam guide that increases X-ray intensity at the sample, the short time between analytical steps, the non-contact measurement principle, and the ability to determine all elements at one voltage at each step while maintaining high sensitivity across the full range.

By scanning very close to the sample surface without touching it, the sample is preserved. Together with the high precision of peak-area separation and determination for each element, this is important for the detailed identification of laminae.

Smaller beam size and analytical steps all the way down to 0.2 mm are acheived with the high resolution kit available as an add-on.

Only Itrax scanners perform XRF scans of sediments that cover all elements from Na to U in a single pass. This ensures that all elements are measured under the same analytical conditions. This provides strong detection limits across the full elemental range and avoids time-consuming rescans at other voltages.

Other unique features of Itrax scanners are that the stability of hardware as well as data processing software make it unnecessary to do frequent re-calibrations during the scans, saving a lot of overhead time during scanning.

Your samples remain minimally affected during and after scanning because Itrax does not come into physical contact with the sample surface. This brings three main advantages: First, pressure on the sample surface is avoided, reducing the risk of deformation in soft samples. Secondly, the risk of forcing water out to form a film between a wet sample and an applied foil is reduced, lowering the risk of adversely affecting the data. Third, the non-contact technique minimizes the time between analytical points, substantially reducing total scan time.

If a magnetic susceptibility sensor is added to your Itrax FleXRay, those measurements are performed last in the analytical sequence, since they require contact with the sample surface and should therefore follow the non-contact measurements.

The RGB camera provides very high-quality images and is equipped with crossed polarizing filters that strongly reduce glare from wet sample surfaces.

Itrax FleXRay scanners offer high precision and repeatability in positioning at each analytical point along the sample. This is needed to ensure correct data at every point, which is important when thickness and absolute positions of laminae are in focus, for instance for spliced core records.

Continued on next page

Software ecosystem

The entire software package is developed by Cox, and includes:

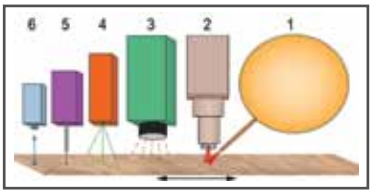
Itrax Navigator, our software for instrument control and real-time data display during scanning.

Q-spec, an advanced software package for spectral display and automated extraction of element peak areas from the X-ray spectra. It also identifies and resolves overlapping peaks, and detects sum peaks and diffraction peaks when they occur. It also identifies and resolves overlapping peaks and detects sum peaks and diffraction peaks when they occur. Element concentrations can be calculated with a simple click; the method is based on Fundamental Parameters and provides robust results across a uniquely wide range of sample matrices using a single calibration. Additional calibrations with other standards are typically only needed for unusual matrix compositions. Another distinctive Q-spec feature is determination of the average atomic number of the analyzed sample volume, including elements too light to be detected directly by XRF. This further improves the precision of the concentration calculations. Q-spec generates a summary file containing all data from each measurement step, together with an indicator showing whether the analysis passed quality checks. This helps keep the user in control of the analytical process at every step. For example, flagged data may result from the presence of an unexpected element. XRF spectra from each analytical point are automatically stored for easy access, review, and reprocessing.

ReDiCore is used to display and present element profiles, radiographic images, magnetic susceptibility data, and sample photographs together.

BoreHole Viewer enables data display and interactive examination of complete boreholes by compiling data from several core scans

Data can be transferred seamlessly between the different software applications and into programs such as Excel.]



This image shows the principal setup of the Itrax FleXRay x-ray source and sensors.
1. X-ray tube with Polyflat™ x-ray optics. 2. XRF detector. 3. RGB camera. 4. Laser distance gague. 5. Spectrometer. 6. Magnetic susceptibility sensor.

Detection limits

Itrax FleXRay Scanner detects elements across the full range from Na to U. High sensitivity, well-defined peaks, and high reproducibility for most metals provide the precision needed for confident use of element ratios in proxy studies.

The table lists detection limits for selected elements of common interest. These values are examples spanning light to heavy elements within the full range detectable by this scanner. Na, Mg, and Al are listed with two values because the FleXRay version for wet sediments has somewhat higher detection limits for these elements. The second value for Na, Mg and Al refers to the FleXRay version for wet and dry samples.

Element	PPM	Element	PPM	Element	PPM
Na	1251/3720	Ti	8	Ba	23
Mg	191/212	V	7	Cd	64
Al	56/60	Mn	6	La	21
Si	30	Br	5	Hf	10
P	22	Rb	5	Hg	9
S	12	Sr	6	Pb	9
K	11	Zr	6	Th	11
Ca	9	Mo	6	U	12

The reference material used is NIST 610, measured at 100 seconds, applying the standard scientific model for the calculations. *Please contact us if you would like information on any specific element not listed here.*

Specifications

Function/Parameter	Value/Description
XRF scans and data	Typical time setting is 3 (1-10) sec. per scan step for a marine sediment total time per analytical step, covering all detected elements. The XRF spot size is 1mmx8mm (8mm XRF scan width) as standard, (0.2mmx8mm with optional equipment). Maximum count rate of the XRF detector is >300,000 cps, allowing for samples with varying matrices without saturation effects. Better than 134 eV XRF detector FWHM at 5.9 keV, at any count rate peak width. This allows for very good peak separation and mimimized overlap. The overhead time between each XRF step is ~0.7 sec.
Magnetic Susceptibility	Bartington MS2E type, having a measuring spot of ~4x10mm. Touches sample surface (add-on).
Optical images	High quality RGB images, ~50 micrometer pixel size, and an image width of ~100 millimeters. Image quality reductions like glare in wet sample photos and light scatter from rough dry surfaces is minimized by the implemented crossed polarizing filters.
X-ray Beam	Well defined x-ray beam with 1mmx8mm, having sharp edges and an even intensity distribution. Enhanced intensity by Polyflat™ x-ray waveguide speeding up analyses for higher sample throughput.
Scanning steps	Any step from full sample length down to 0.01 millimeter can be selected. Step sizes larger than the beam are implemented by sweeping over the selected step, without information loss. This makes any step size analyses down to 1mm just as fast as larger steps, as larger steps than beam size are achieved by collecting data while sweeping over the selected step. Itrax FleXRay allows for scanning without loss of any information along a sample, and also allows for fast overview through discreet analysis mode, by "jumping" between positions at user selectable jump length and analytical step length.
X-Ray tube	A 60W Rh anode tube with an expected life time of 50,000 hours.
Element range	Na – U for wet and dry samples, determined simultaneously.
Sample dimensions	Up to 1520 (L) x 127 mm Ø split and full core.
Instrument size and weight	~2800x1350x1725 millimeters LxWxH including stand, plus top light. The weight is ~700 kilos.
Quantitative calibration	Peak areas and element concentrations are both available for the user, by a single click. The State-of-the-art element quantification software is pre-calibrated and covers a very wide range of sample matrices without further calibrations. More standards can be added, but are only needed for odd sample compositions.
Safety Registration	Ch-08425/S, in Swedish Radiation Safety Authority, plus is approved for use in many other countries. The dose rate equivalent level is below 0.5 µSv/h, allowing for work close to the instrument without limitations.
Power requirement	As standard 230 volts / 50-60Hz / 16 A one phase / 3kW. Other voltages and/or frequencies can be delivered on request
Available add on's	1. High resolution scanning kit that allows the user to switch beamsize to 0.2 mm. beam, for scanning in the 0.2-0.9 mm range. 2. Magnetic Susceptibility meter Bartington MS2E type, having a measuring spot of ~4x10mm. Touches sample surface. 3. Spectrometer with a choice of configurations. Please contact us for more details.

All specifications and all information in this document are subject to improvements, changes and updates. Please contact us if you want more information.

COX ANALYTICAL
Cox Analytical Systems www.coxsys.se phone: +46 708 3660 info@coxsys.se

SPONSORS


SOCIETY FOR SEDIMENTARY GEOLOGY
100th
1926
2026
ANNIVERSARY


NSTC


COX
ANALYTICAL SYSTEMS


中華民國地質學會
Geological Society Located in Taipei


國立臺灣大學
敦品勵學・愛國愛人


國立中央大學

Sedimentology of Convergent Margins

Symposia and field trips – April 26 to May 2

Compiled by Ludvig Löwemark[1] and Shahin Dashtgard[2]

[1]National Taiwan University

[2]Simon Fraser University

This field guide is largely based on:

Lin, A.T.-S., 2024. Field Guide Book: Tectonics, Sedimentation and Geomorphology of the Active Taiwan Mountain Belt. National Central University, Taiwan.

Chao, W.-S., Chen, S. Huang, J.-J., Kuo, P.-C., Lin, T.-S., Löwemark, L., Zheng, C. 2017. The 14th International Ichnofabric Workshop. Post-Workshop Field Guide. National Taiwan University, pp. 17

Huang, J.J. and Michael Strasser, M., 2025. Dynamic Island. Field excursion to Taiwan (Republic of China). 10th to 23rd February, 2025

Sponsors

中華民國地質學會 Geological Society Located in Taipei

SEPM Society for Sedimentary Geology

國立中央大學 National Central University

國立臺灣大學 人愛國愛・學勵品教

NSTC

COX ANALYTICAL SYSTEMS

Contents

Overview 3
Tectonic Setting of Taiwan 4
Present-Day Hydrodynamics and Sedimentation in Taiwan 7
Western Foreland Basin 9
Stratigraphic Fill of the Western Foreland Basin 9
Field Stops in the Western Foreland Basin – Days 1 to 4 12
Stop 1-1: Dahan River section (Yingge) – Middle to Late Miocene Nanchuang Formation *(24.9489° N, 121.3565° E)* 12
Stop 2-1: Dajia (Tachia) River upstream of the bike bridge – Late Pliocene Yutengping Sandstone (Kueichulin Formation) *(24.0424° N, 120.6992° E)* 13
Stop 2-2: Dajia (Tachia) River upstream of the Pifeng Bridge – Late Pliocene Chinshui Shale and Early Pleistocene Cholan Formation *(24.2794° N, 120.7608° E)* 15
Stop 2-3: Dajia (Tachia) River, Shigang Dam – neotectonics stop *(24.2827° N, 120.7692° E)* 16
Stop 2-4: Huoyanshan Nature Preserve (Fiery Mountain) – Late Pleistocene Toukoshan Formation *(24.3625° N, 120.7309° E)* 16
Stop 3-1: Wu River, Guoxing – Middle to Late Miocene Nanchuang Formation *(24.0266° N, 120.8264° E)* 17
Stop 3-2: 921 Earthquake Museum of Taiwan in Wufeng – neotectonics stop *(24.0424° N, 120.6992° E)* 17
Stop 3-3: Zhoulan Gorge, Da'an (Ta-an) River – neotectonics stop *(24.2921° N, 120.8306° E)* 18
Tian Liao Moon World – Mio-Plio-Pleistocene Gutingkeng Formation 21
Taitung-Chihpen Century Hotel 21
Coastal Range 22
Field Stops in the Southern Coastal Range – Day 5 24
Stop 5-1: Lichi (Liji) Melange 24
Stop 5-2: Xiaoyehliu Overturned Turbidites (Fukang) 24
Stop 5-3: Shiyushan (Umbrella Rock) Paliwan Formation 25
Stop 5-4: Baxiandong Uplifted Sea Caves (optional) 25
Stop 5-5: Tropic of Cancer 26
Stop 5-6: Chimei Turbidites and Chimei Fault (optional) 26
Stop 5-7: Derwu Viewpoint 26
Hoya Spa Hotel 27

Field Stops in the Northern Coastal Range Stops – Day 6 28
Stop 6-1: Shitiping White Tuffs 28
Stop 6-2: Niushan Huting – Slabs and blocks of shallow marine conglomerate 29
Stop 6-3: Lingding (Lingding) Tuluanshan Formation volcanoclastics 29
Stop 6-4: Qingshui Cliffs (optional) 30
Field Stops along the NE Coast - Day 7 31
Stop 7-1: Bitoujiao coastal platform – Miocene Kueichulin Formation *(25.1285° N, 121.9241° E)* 31
Stop 7-2: Yehliu Geopark – Miocene passive margin *(25.2084° N, 121.6936° E)* 32
Stop 7-3: Shuiwei Harbor Coastal Platform – Oligocene rifting 34
References 36

Overview

Dates	Locations
4/25	Icebreaker – NTU Geosciences Hotel: Howard Civic International House
4/26	**Symposium I - NTU Geosciences** ***Keynote speakers*** Field stop - Western Foreland Basin Transfer to central Taiwan Hotel: Chuanfu Hotel, Taichung
4/27	Field stops - Western Foreland Basin Outcrops Hotel: Chuanfu Hotel, Taichung
4/28	Western Foreland Basin Outcrops Hotel: Kuva-Chateau Hotel, Taoyuan
4/29	**Symposium II – NCU Earth Sciences** Field stop – Moon World Transfer to Taitung, Eastern Taiwan Hotel: Century Hotel, Taitung
4/30	Field stops – Southern Coastal Range Outcrops Hotel: Hoya-spa Manor, Ruei-Sui
5/1	Field stops – Northern Coastal Range Outcrops Transfer to Ilan Hotels: Silimu B&B and Winwin Guest House, Ilan
5/2	Field stops – Northeast Coast Outcrops Return to Taipei Hotel: Howard Civic International House

Tectonic Setting of Taiwan

Taiwan and its north-south trending mountain ranges contain a record of the still ongoing collision between the volcanic arc on the Philippine Sea Plate and the continental margin of the Eurasian continent (Fig. 1). The Philippine Sea Plate is moving northwestward at a rate of 50–82 mm/yr (Lin et al., 2003; Simoes and Avouac, 2006; Yu et al., 1997). In the south, oceanic crust of the Eurasian Plate is being subducted under the Philippine Sea Plate, thereby providing an analogue of the early stages of the collision. In the central part of Taiwan, the Coastal Range is actively bulldozing the sedimentary and metamorphic rocks of the Central Ranges and the Western Foothills towards the NW and this region is considered to record the active phase of the collision. In the north, the mountains are collapsing, thereby representing a post-collisional state of the orogeny. At the same time, the subduction of the Philippine Sea Plate at the Ryukyu Arc and the westwards propagating opening of the Okinawa Trough have resulted in volcanic activity that is evident in the volcanoes of the Yangmingshan mountains north of Taipei.

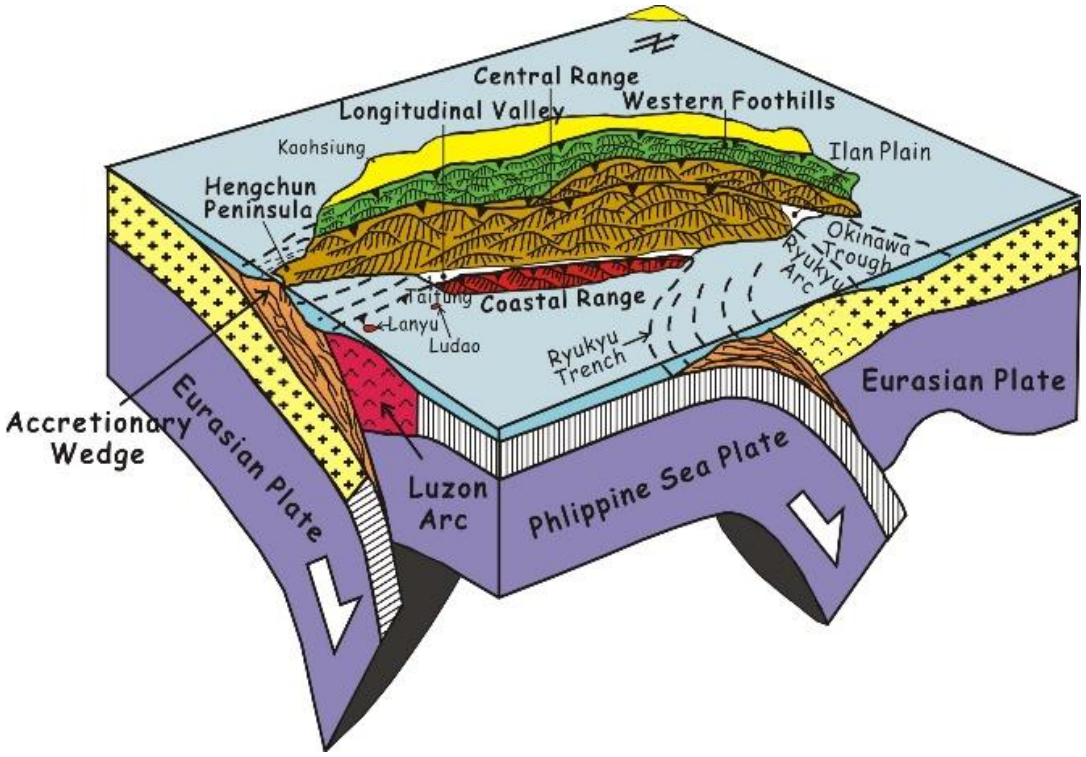


Figure 1 – 3D tectonic framework of Taiwan. Block diagram showing arc-continent collision and tectonic setting of Taiwan. Taiwan is situated in the active arc-continent collision region between the Eurasian continent and the Philippine Sea plate. South of Taiwan, the oceanic crust of the South China Sea (aged 15–32 Ma) is subducting beneath the Philippine Sea Plate along the Manila Trench. To the east of Taiwan, the Philippine Sea Plate is being consumed beneath the Eurasian continent along the Ryukyu Trench. The Philippine Sea Plate is moving northwestward at 310° at a rate of 50–82 mm/yr. The Luzon Arc on the Philippine Sea Plate is colliding with the Asian continent and forming the Coastal Range in eastern Taiwan.

The Taiwan orogenic belt comprises four geologic provinces (Ho, 1988). From east to west, they are the Coastal Range, the Central or Backbone Range, the Hsuehshan Range,

and the Western Foothills (Fig. 2). The terrains are of Eurasian Plate affinity with the exception of the Coastal Range, which incorporates the accreted volcanic arc and belongs to the Philippine Sea Plate. Overthrusting of the Luzon Arc on the northern South China Sea margin has exhumed material that was previously located in the outer part of the rifted South China Sea margin (Fig. 3).

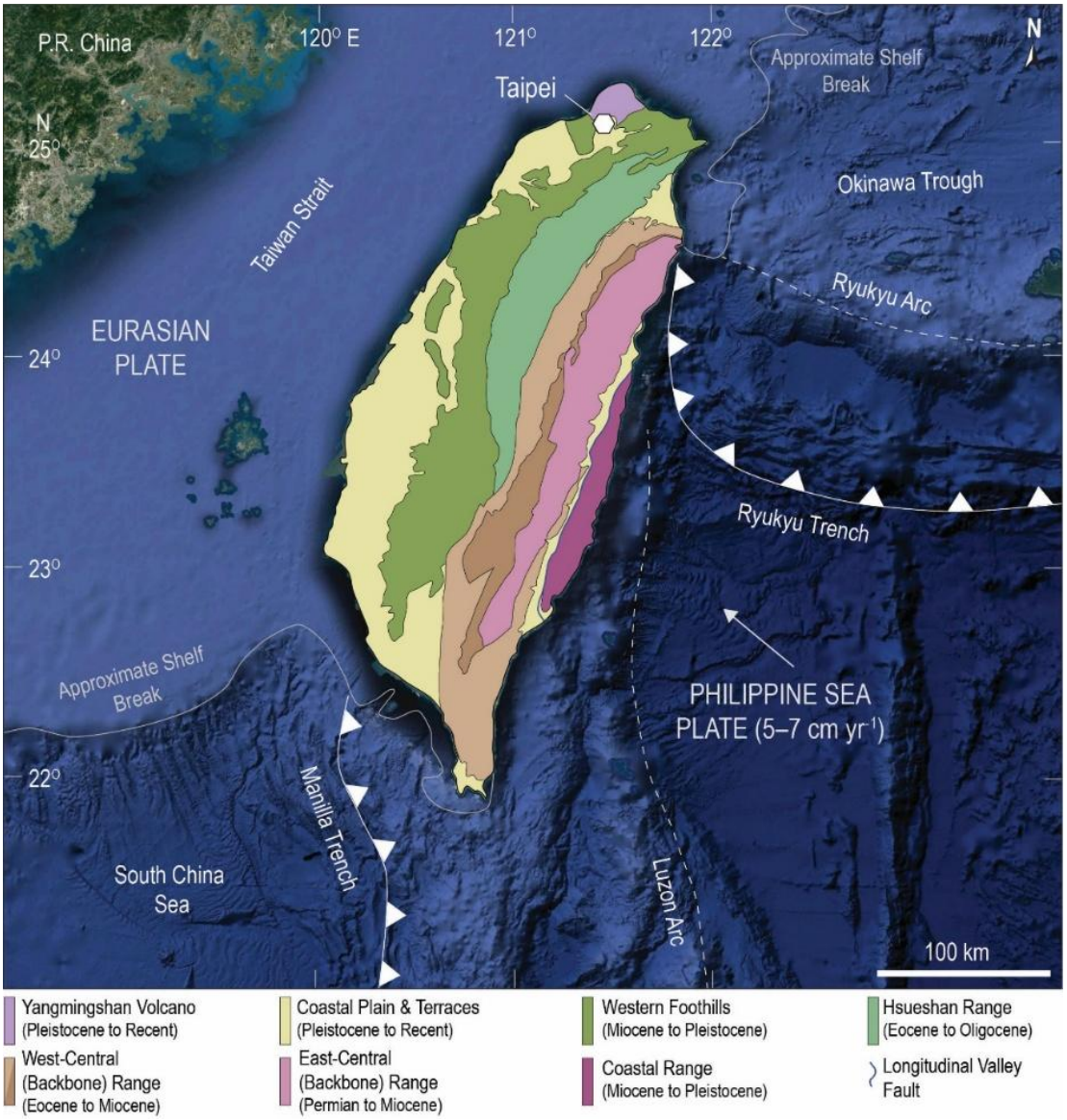


Figure 2 – General geological map of Taiwan showing the major tectonic and geographic elements of and near the island. The Western Foreland Basin extends from the Western Foothills westward and below the Taiwan Strait. The present-day rate of relative motion of the Philippine Sea Plate is derived from Lin et al. (2003) and Simoes and Avouac (2006). The general geology of Taiwan is based on Lin and Chen (2016), and the base map is sourced from Google Earth. Figure is modified after Dashtgard et al. (2020).

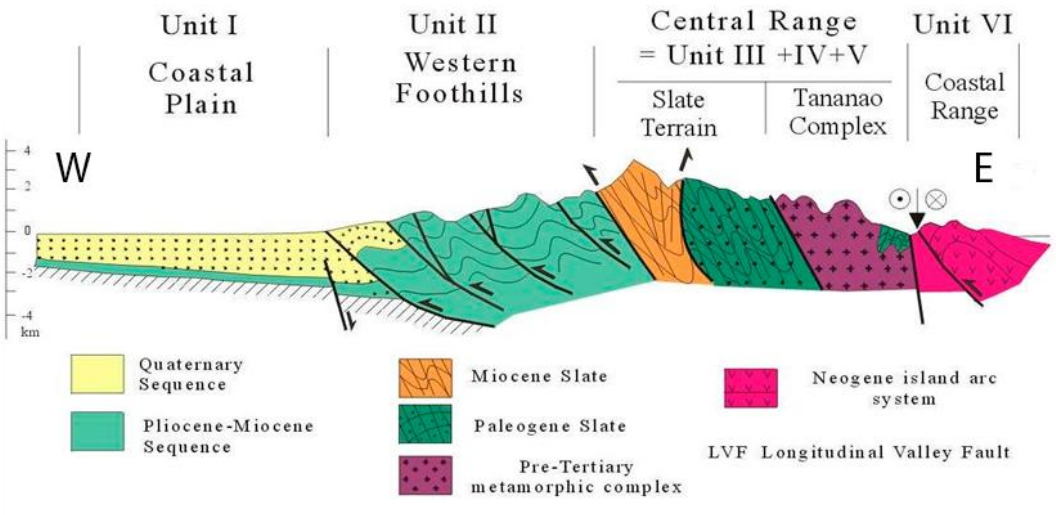


Figure 3 – Schematic transect through the central part of Taiwan showing the exhumed Central Range and the Western Foothills thrust and fold belt. The Coastal Range acts like a bulldozer, pushing the rocks on the continental margin of the Eurasian Plate towards the NW (modified after Teng, 1990).

The basement complex of Taiwan was covered by young sediments during the Cenozoic rifting related to the opening of the South China Sea. The arc-continental collision began in the late Miocene and continues today, and during this ongoing orogenic event, basement rock has been exhumed. Several mechanisms have been postulated to account for the exhumation (mountain building) process: (A) critical wedge, (B) discrete sequential thrusting model, (C) upper-crustal extension-extrusion and (D) lateral extrusion model, (E) lithospheric collision and (F) subduction and extrusion model. Recent development of close integration of metamorphic records with stratigraphy, geologic structure, geodesy, and seismological constraints led to emphasis on basal accretion and tectonic-climatic feedbacks, forming concepts of (G) deformation partitioning in mountain building processes. The exhumation was likely not uniform during the entire collision process but increased in the latest 2–3 Myr.

The Coastal Range acting like a bulldozer sitting on the edge of the Philippine Sea Plate has experienced rapid vertical crustal movements since the initiation of the orogeny. A rapid uplift around the time of the initiation of the collision at ~6 Ma resulted in an unconformity on the Miocene volcanic arc, followed by rapid foredeep subsidence, and finally extremely rapid uplift (9-14 mm/year) to form the Coastal Range in the last 800-500 ky (Lai et al., 2022).

Present-Day Hydrodynamics and Sedimentation in Taiwan

Tropical cyclones (TCs) in the Taiwan Strait normally pass over the island before crossing the strait. TC-related precipitation affects sedimentation mainly in the form of elevated runoff, and both hyperpycnal and hypopycnal discharge, and this is manifested in the delivery of large sediment volumes to the strait during and shortly after passage of the storm (Fig. 4; Chen et al., 2018; Chien and Kuo, 2011; Dadson et al., 2003; Dadson et al., 2004; Milliman and Kao, 2005; Warrick and Milliman, 2003). For example, during Super-Typhoon Herb (1996), suspended sediment concentrations in the Choshui River were measured at 1–10 g L^{-1} before and after the storm *versus* 10–100 g L^{-1} during it. Hyperpycnal conditions were quickly achieved during this event, although the peak in suspended-sediment concentration and discharge lagged behind the peak in precipitation by approximately 12 hours, which is approximately half the duration of the TC (Milliman and Kao, 2005). Total sediment discharge from the Choshui River during Super-Typhoon Herb (1996) was 130 million tonnes. Sediment discharge from the Choshui River during Typhoon Mindulle (2004) was estimated at approximately 72 million tonnes and the suspended sediment concentration exceeded 200 g L^{-1} at the start of the storm due to erosion of recent landslides; nearly 40% of this material was sand (Milliman et al., 2007).

Typhoon Morakot (2009) is the most devastating TC to hit Taiwan in the past 50 years because of the volume of rainfall associated with the event: 3000 mm of rain fell in 4 days in parts of Taiwan with over 1000 mm in a 24-hour period (Chien and Kuo, 2011). The elevated rainfall associated with Typhoon Morakot (which was a Tropical Storm at the time of making landfall), and other high precipitation TCs, is attributed to the slow translation speed of the typhoon across Taiwan, its coincidence with the monsoon, and the interaction of the typhoon with the nearly 4000 m high mountains of the Central Mountain Range (Backbone Range, Fig. 2; Chang et al., 1993; Chien and Kuo, 2011; Droser et al., 1999; Wu et al., 2009).

Sediment distribution in shallow-water regions of the Taiwan Strait is complex and reflects the interaction of multiple currents operating therein (Huh et al., 2011; Kao et al., 2008). Most of the seafloor comprises fine- to coarse- sand (97–100% sand) assembled into dune-scale bedforms (Boggs et al., 1979; Milliman et al., 2007). The exceptions to this are mud-dominated shallow-water regions along the margins of the strait upstream of river mouths (<10 m water depth; Kao et al., 2008; Milliman et al., 2007), and a wide band of mud-dominated seafloor that extends seaward off the Da'an River and then northwestward to the coast of The People's Republic of China (Fig. 1; Huh et al., 2011; Nagel et al., 2014).

Only a few studies describe the sedimentological characteristics of TC deposits in the Taiwan Strait. and these studies largely focus on the Choshui River (e.g., Milliman et al., 2007). Milliman et al. (2007) showed that TC-related hyperpycnites outboard of the Choshui River comprise medium-grained sand that was draped with up to 50 cm of hyperpycnal-flow derived mud; mud deposits thickened to 1–2 m (< 5% sand) between sand dunes. Most mud was removed subsequently by tidal flow, although some mud beds were preserved in depositional lows (Milliman et al., 2007).

For the past 35 years, an average of 3.5 TCs per year pass over Taiwan or the eye of

the storm passes within 50 km of the coastline. Super-typhoons occur less frequently with one impacting Taiwan approximately every 4 years. The intensity of TCs is highly variable, as are their paths with respect to Taiwan. In a 35-year period (1983–2017), super-typhoons crossed central Taiwan at a rate of one every approximately 17 years. Tropical depressions and tropical storms crossed central Taiwan every 1.9 years on average, and typhoons were experienced at a rate of one every approximately 1.5 years.

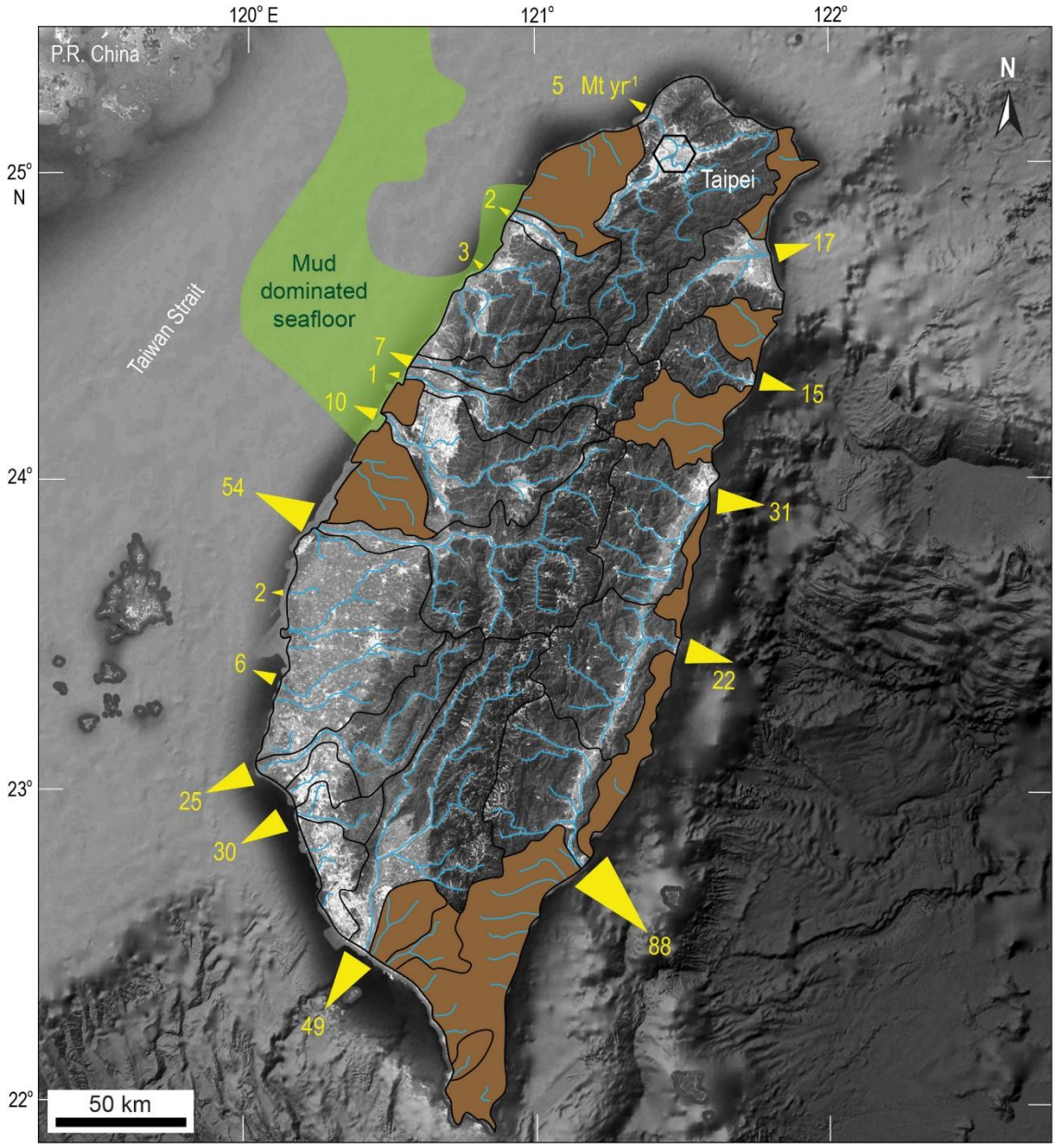


Figure 4 – Map of Taiwan (source: Google Earth) showing the approximate position of the drainage divides between river catchments (black lines) and the main rivers (light blue lines). The yellow arrows and numbers indicate the annual sediment load (in millions of tonnes per year (Mt yr^{-1}) predicted for each of the main rivers in Taiwan (Dadson et al., 2003), while the brown areas indicate river catchments without sediment load data. The mud-dominated seafloor is shown in green and is derived from Huh et al. (2011) and Nagel et al. (2014). Figure is modified after Dashtgard et al. (2020).

Western Foreland Basin

Taiwan formed through the oblique arc-continent collision of the Philippine Sea Plate and the Eurasian Plate (Fig. 1; e.g., Suppe, 1981, 1984). The two plates began colliding in the Late Miocene (~6.5 million years ago (Mya)) and formed the 330 km long, 100 km wide orogenic belt that makes up most of Taiwan (Fig. 2). The nearly 4,000 m high mountain belt continues to uplift at a rate of approximately 5–7 mm per year (Castelltort et al., 2011; Chang et al., 2023; Covey, 1984; Lin and Watts, 2002; Nagel et al., 2018). Through the ongoing collision and over the past 6.5 million years, the main depocenters of Taiwan's Western Foreland Basin (WFB) migrated south-southwestward at a rate of approximately 31.5 km (+10 to -5 km uncertainty) per million years (Shaw, 1996; Simoes and Avouac, 2006), and the continued and persistent uplift of Taiwan has exposed pre-collisional passive margin strata and post-collisional foreland basin strata (Lin et al., 2003; Lin and Watts, 2002; Suppe, 1981, 1984). The WFB is characterized by both high-accommodation and high-sedimentation rates, with sediment accumulation rates exceeding 400 m per million years in the Early Pliocene, and 1,000 m per million years in the late Pleistocene (Chang and Chi, 1983; Chen et al., 2001a; Covey, 1984; Simoes and Avouac, 2006; Vaucher et al., 2021; Vaucher et al., 2023b). Upper Miocene to Pliocene sedimentary strata of the Kueichulin Formation were deposited during the early stages of the collision (Lin et al., 2003; Yu and Chou, 2001) and in mainly shallow-marine environments (Castelltort et al., 2011; Covey, 1984; Dashtgard et al., 2020; Nagel et al., 2013).

Stratigraphic Fill of the Western Foreland Basin

The stratigraphic fill of the Western Foreland Basin extends from the Late Miocene to present, and begins with the late Miocene–early Pliocene Kueichulin Formation (Fig. 5). The Kueichulin Formation overlies the Nanchuang Formation and grades both upwards and southwards into the Chinshui Shale (Castelltort et al., 2011). The Kueichulin Formation is up to 800 m thick and consists of three members, including (from base to top): Kuantaoshan Sandstone, Shihliufen Shale, and Yutengping Sandstone (Fig. 3; Castelltort et al., 2011; Lin et al., 2007; Pan et al., 2015; Shaw, 1996). The Kuantaoshan Sandstone records deposition on the eastern margin of the Eurasian Plate between ~6.3 and 5.4 Mya (Hsieh et al., 2023a). The Shihliufen Shale is interpreted as forming near the Miocene-Pliocene boundary and coincides with the collision of the Luzon Arc on the Philippine Sea Plate with the Eurasian Plate starting around 5.4 Mya and continuing to about 4.9 Mya. The Yutengping Sandstone Member records deposition from 4.9–3.2 Mya (Hsieh et al., 2023a). Overall, and excluding the Shihliufen Shale, the Kueichulin Formation is sandstone-dominated and was deposited under wave and tidal action mainly in shelfal, shallow-marine, and deltaic environments (Castelltort et al., 2011; Dashtgard et al., 2020; Dashtgard et al., 2021; Nagel et al., 2013).

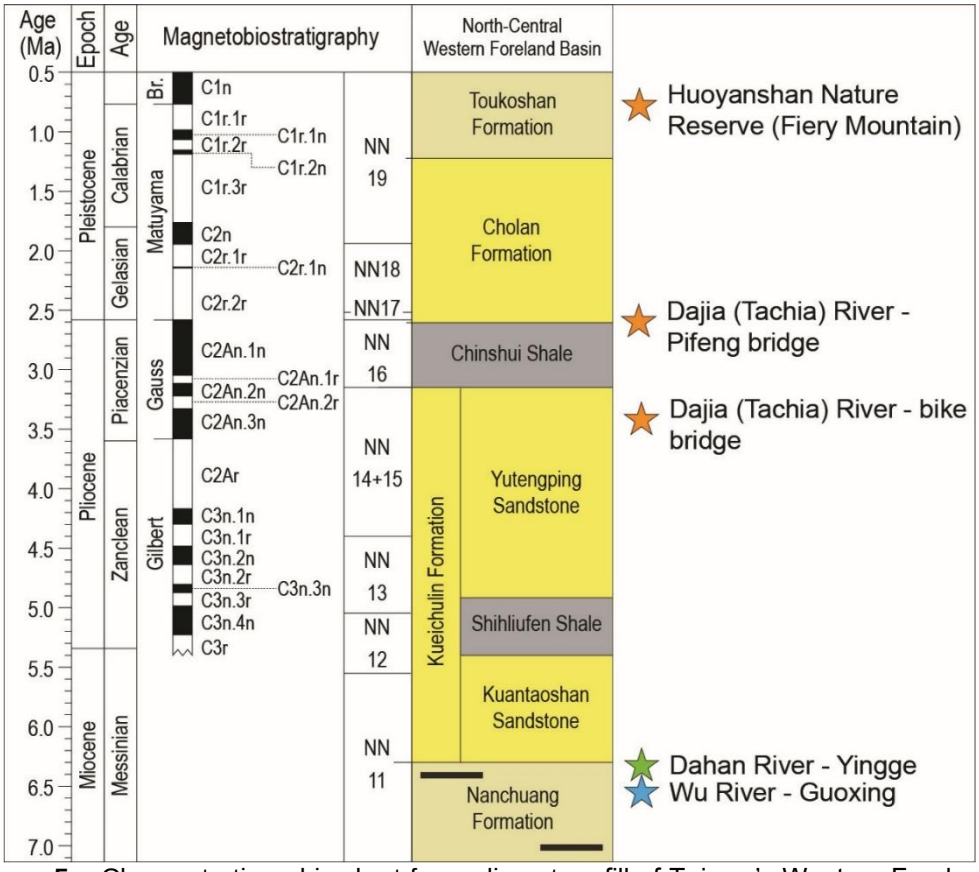


Figure 5 – Chronostratigraphic chart for sedimentary fill of Taiwan's Western Foreland Basin in the northern part of the Western Foothills. The righthand column shows the stratigraphic position of the strata we will observe at the various field stops on day 1 (green), day 2 (orange), and day 3 (blue). The dominant lithologies of units are indicated by the underlying colours (grayish yellow = terrestrial sandstone, bright yellow = marine sandstone, grey = marine mudstone/shale, and black = coal). Nannofossil (NN) zonation is based on the International Commission on Stratigraphy, and nannofossil distributions in formations are derived from Horng and Shea (1996) and Pan et al. (2015) and references therein. The chronostratigraphic chart for Taiwan is based on Teng et al. (1991), Lin et al. (2003), Nagel et al. (2013) and Lin and Chen (2016). The magnetobiostratigraphy is from Hsieh et al. (2023c) and references therein. The lithologies of various units are based on this study and MOEA (2019). Figure is modified from Dashtgard et al. (2026).

The Kueichulin Formation is overlain by the late Pliocene Chinshui Shale, the latter of which is a mudstone-prone interval deposited in an offshore environment during a period of maximum flooding and increased subsidence in the WFB (Castelltort et al., 2011; Nagel et al., 2013; Pan et al., 2015). The early Pleistocene Cholan Fm comprises mainly heterolithic strata deposited in shallow-marine environments and under the influence of wave, river and tidal processes (Covey, 1984; Nagel et al., 2013; Pan et al., 2015; Vaucher et al., 2021). The whole interval is capped by the late Pleistocene Toukoshan Formation, which is a conglomerate-dominated interval that records deposition mainly in terrestrial environments. Overall, the shallowing-upwards Chinshui–Cholan–Toukoshan succession records infilling of the WFB associated with the westward migration of the Taiwan orogen (Nagel et al., 2018). As well, during deposition of all post-collision strata (Late Miocene to Recent), the north-to-south deepening of the WFB remains evident (Fig. 6).

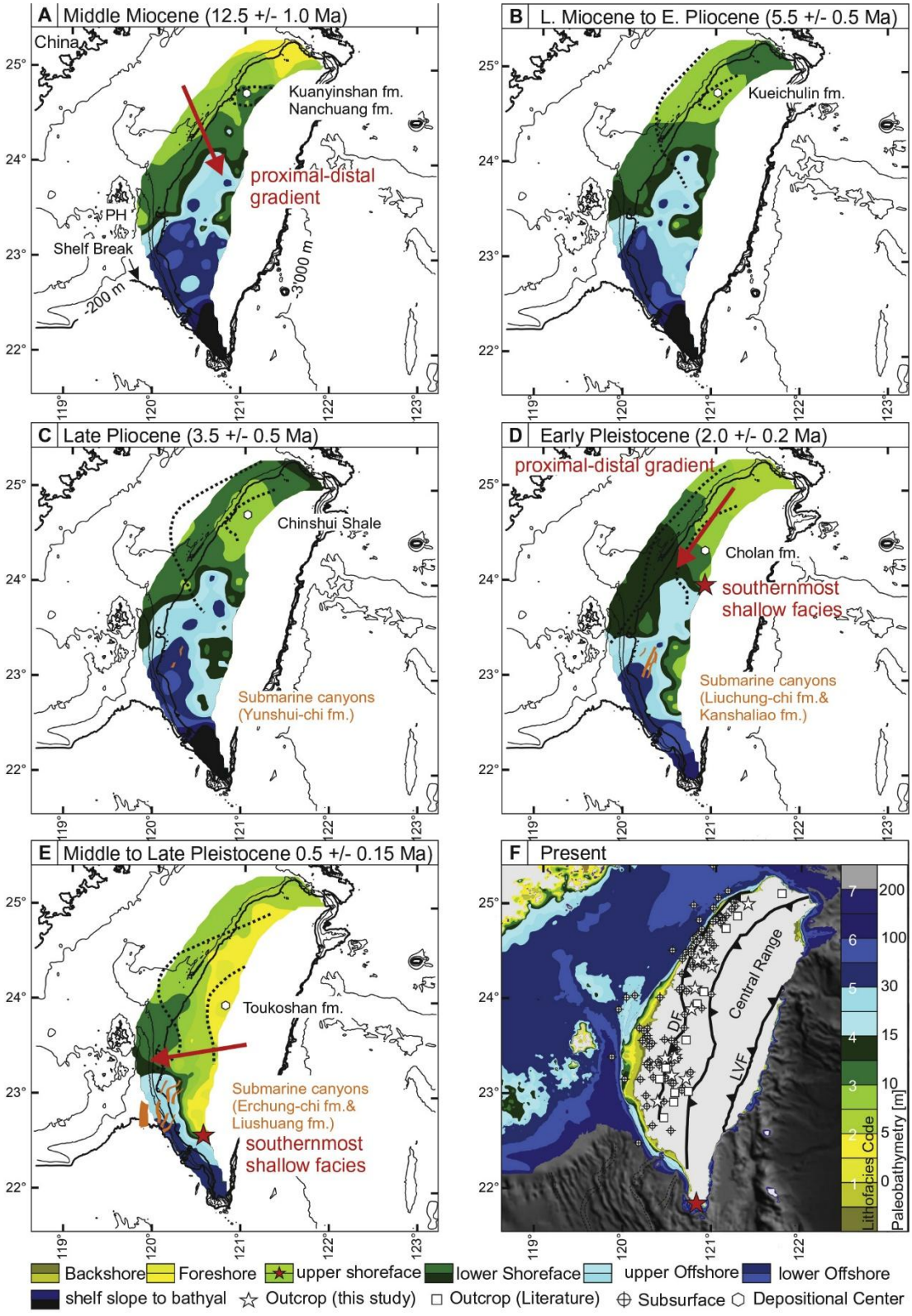


Figure 6 – Paleogeographic reconstructions of the Western Foreland Basin from **(A)** pre-collision (Nanchuang Formation) through **(F)** present. The strata we will look at correlate to **(A)** Stop 1-1 and 3-1, **(B)** Stop 2-1, **(C)** Stop 2-2, **(D)** Stop 2-2, and **(E)** Stop 2-4. Maps are derived from Nagel et al. (2013).

Field Stops in the Western Foreland Basin – Days 1 to 4

Our plan is to visit both outcrops of sedimentary strata that record the evolution of the Western Foreland Basin and sites that record neotectonic events in the region. The sites we will visit are shown in Figure 7, and descriptions of the sites are given below. The stratigraphic positions of the strata we are looking at is shown in Figure 5.

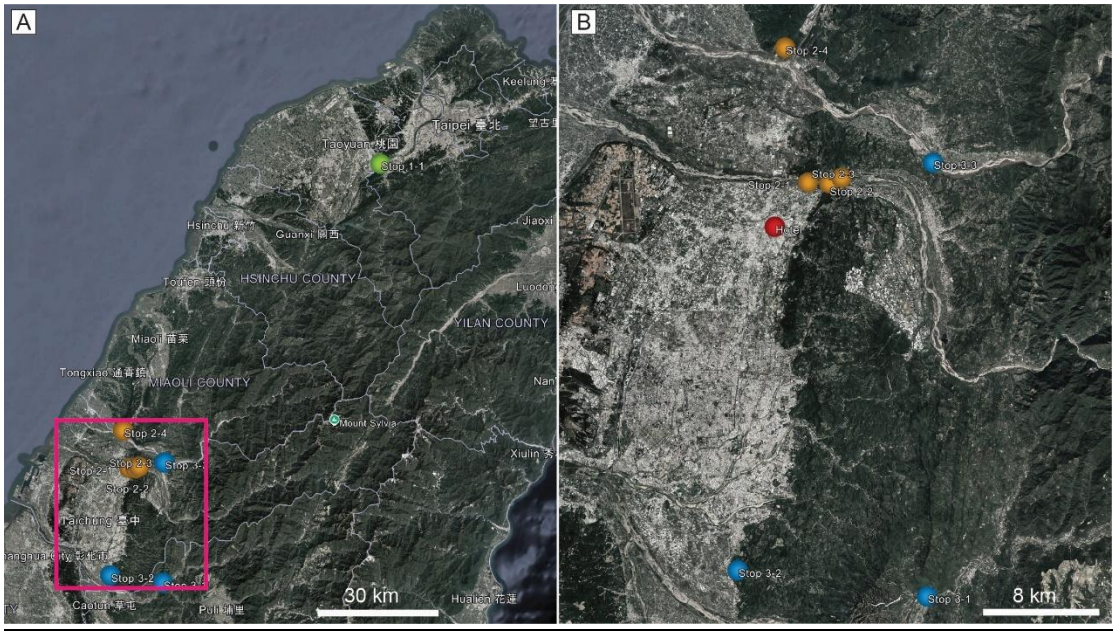


Figure 7 – (A) Google Earth images of northwest Taiwan showing the approximate positions of field trip stops in the Western Foreland Basin. The pink rectangle shows the area enlarged in **(B)**.

Day 1 – Sunday, April 26

Stop 1-1: Dahan River section (Yingge) – Middle to Late Miocene Nanchuang Formation *(24.9489° N, 121.3565° E)*

The outcrop along the Dahan River at Yingge (Fig. 8A) exposes shallow marine strata of the uppermost part of the Nanchuang Formation, which is one of three coal bearing formations in northern Taiwan (Huang, 2005). In northern and central Taiwan, the Nanchuang Formation typically consists of deltaic sediments deposited in both terrestrial and marine environments (Fig 6A–B).

At Yingge, the exposed strata appear to record progradation mixed tidal flats with abundant wavy- to lenticular bedding and pyritized nodules, algal mats, a composite fill of a tidal channel (Fig. 8B), and an incipient-paleosol. Elsewhere, thin coal beds and coarse clastic layers are abundant, and some strata contain sparse marine fossils (Ho, 1988). In addition to the coals beds, some of which have been exploited, the 500–600 m (in Taipei area) thick Nanchuang Formation also contains numerous volcanic tuff beds of varying thickness (Ho, 1988).

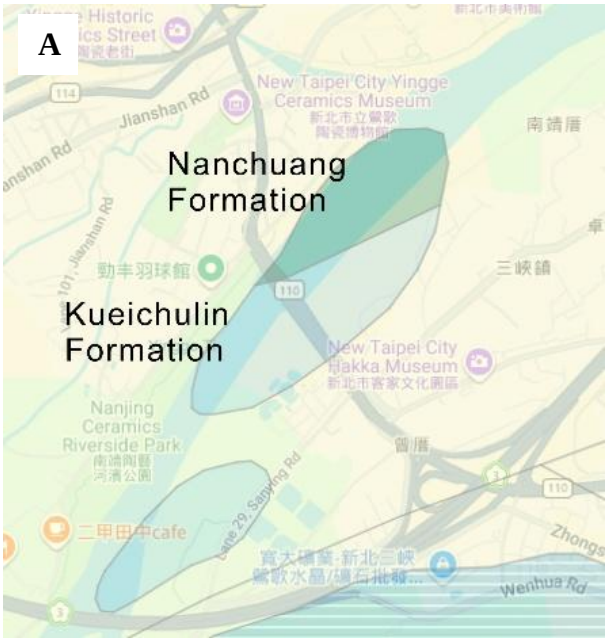




Figure 8 – (A) Geological map overlain on the river and road map of Yingge and surrounding areas. Both the Nanchuang and overlying Kueichulin Formations are exposed in the river, but only the Nanchuang Formation is accessible today. **(B)** Oblique aerial view of tidal channel.

Day 2 – Monday, April 27

Stop 2-1: Dajia (Tachia) River upstream of the bike bridge – Late Pliocene Yutengping Sandstone (Kueichulin Formation) *(24.0424° N, 120.6992° E)*

The outcrop along the Tachia River upstream of the bike bridge exposes the upper part of the Yutengping Sandstone which is the uppermost unit of the Kueichulin Formation. The up to 800 m thick Kueichulin Formation is Late Miocene–Early Pliocene and overlies the Nanchuang Formation (Fig. 6B–C). It grades both upwards and southwards into the Chinshui Shale (Castelltort et al., 2011). The sedimentation rate estimated

during deposition of the Yutengping Sandstone exceeds 400 m per million years (Chang and Chi, 1983; Chen et al., 2001a; Covey, 1984; Simoes and Avouac, 2006). Interestingly, the organic matter preserved in the Yutengping indicates that virtually 100% of the organic material, and probably the associated sediment, is derived from the recently uplifted Taiwan Orogen (Fig. 9; Dashtgard et al., 2021; Hsieh et al., 2023b).

The strata we will observe at this field stop comprise mudstone to sandstone cycles that in the lower part of the Yutengping Sandstone and at localities further north have been attributed to Milankovitch cycles (Hsieh et al., 2023c). These strata are dominated by heterolithic intervals that are interpreted as recording deposition in a tidal strait with a strong fluvial overprint. As well, evidence of extensive soft-sediment deformation in some sandstone beds is attributed to slumping induced by seismic activity, possibly on the front of strait-margin deltas.

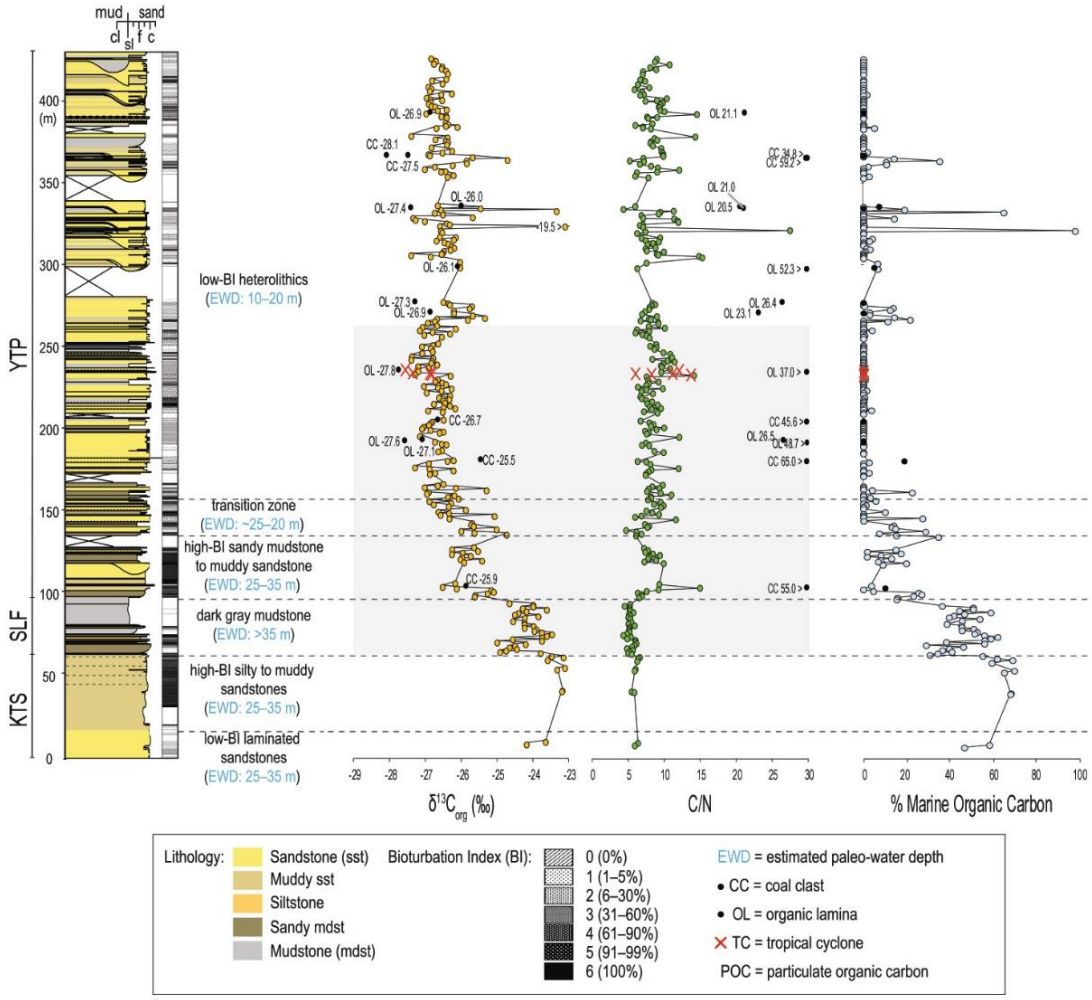


Figure 9 – Litholog through the upper Kuantaoshan Sandstone (KTS), Shihliufen Shale (SLF) and lower Yutengping Sandstone (YTP) exposed along the Da'an River. Measurements of $\delta^{13}C_{org}$ and Carbon:Nitrogen (C/N) indicate that after emergence of Taiwan virtually all organic material, and presumably the sediment as well, delivered to the WFB derived from the island. Unfortunately, these strata are presently buried under 3 m of gravel and a road was built overtop as well. Figure is modified from Hsieh et al. (2023b) and Dashtgard et al. (2021).

Stop 2-2: Dajia (Tachia) River upstream of the Pifeng Bridge – Late Pliocene Chinshui Shale and Early Pleistocene Cholan Formation *(24.2794° N, 120.7608° E)*

The second outcrop along the Tachia River that we will visit is upstream of the Pifeng Bridge and is also upsection of stop 2-1. Here, the upper part of the Chinshui Shale and lower part of the Cholan Formation are exposed (Fig. 5). The Late Pliocene Chinshui Shale is a mudstone-prone interval deposited in an offshore environment during a period of maximum flooding and increased subsidence in the WFB (Castelltort et al., 2011; Hsu et al., 2006; Nagel et al., 2013; Pan et al., 2015). The Early Pleistocene Cholan Formation comprises mainly heterolithic strata deposited in shallow-marine environments and under the influence of wave, river and tidal processes (Fig. 6C–D; Covey, 1984; Nagel et al., 2013; Pan et al., 2015; Vaucher et al., 2021). They have been interpreted as the accumulated deposits of storm-flood deltas in a tidal strait (Fig. 10; Vaucher et al., 2023a). The sedimentation rate during deposition of the Cholan Formation is estimated at close to 1,000 m per million years (Vaucher et al., 2021).

The strata we will observe at this field stop comprise mainly mudstone of the Chinshui shale that is overlain by mudstone-to-sandstone cycles of the Cholan Formation. The Cholan Formation comprises thick successions of heterolithics and thick sandstone beds that are interpreted as possible channelized hyperpycnal flows generated during typhoons (Dashtgard et al., 2020; Vaucher et al., 2023a).

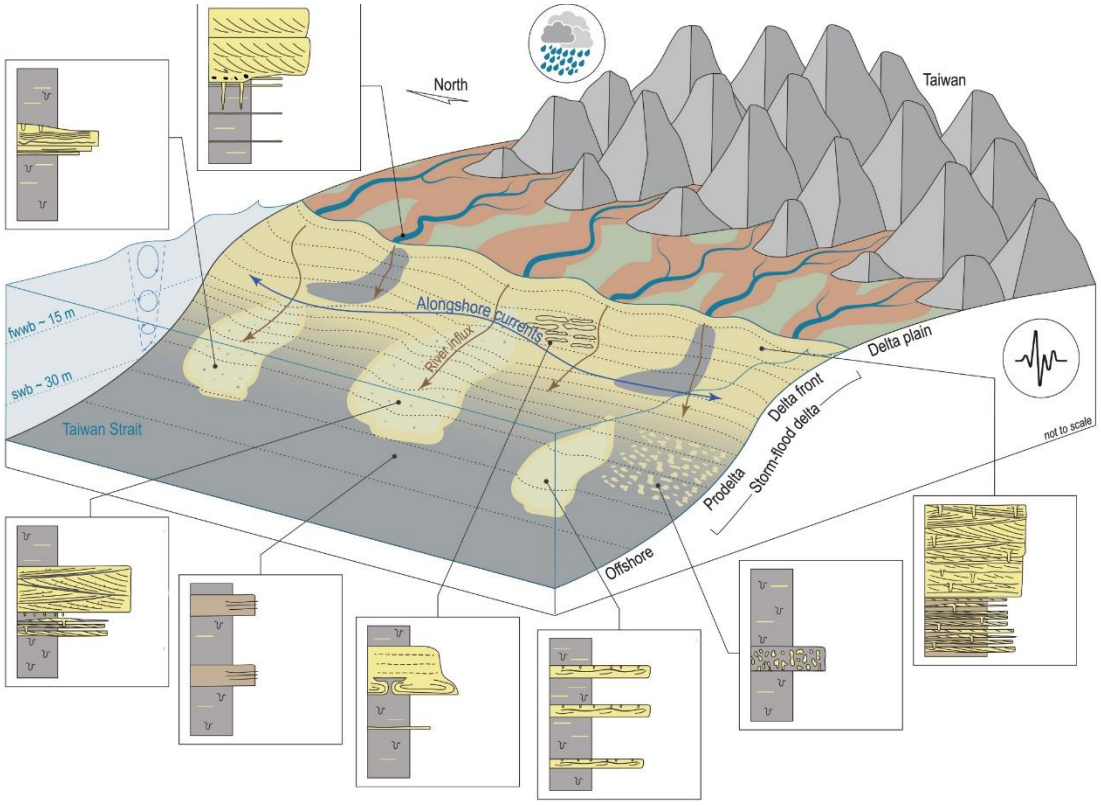


Figure 10 – Conceptual model of a storm-flood-dominated delta system proposed by Vaucher et al. (2023a) for the Taiwan coast during the Early Pleistocene (Cholan Formation). The cloud with the rain and the seismic icon symbolise the frequent tropical cyclones and earthquakes that affect Taiwan, respectively. Fwwb: fair-weather wave base; swb: storm wave base. Figure and caption are modified from Vaucher et al. (2023a).

Stop 2-3: Dajia (Tachia) River, Shigang Dam – neotectonics stop *(24.2827° N, 120.7692° E)*

Shigang Dam was damaged severely during the Mw=7.6 Chi-Chi Earthquake in 1999, and this resulted in the main part of the dam uplifting 12 m and the northern extent uplifting by only 2 m. The resulting 10 m offset severely damaged one of the water control gates, and the damage is preserved in the Shigang Dam Park (Fig. 11).



Figure 11 – Damage o the Shigang Dam during the 1999 Chi-Chi earthquake. The photo on the left is taken from the end of the section at stop 2-2 looking upstream, and the green box highlights where the fault rupture plane propagated through the dam. The photo on the right is from the Shigang Dam Park looking downstream.

Stop 2-4: Huoyanshan Nature Preserve (Fiery Mountain) – Late Pleistocene Toukoshan Formation *(24.3625° N, 120.7309° E)*

The last stop of day 2 is at Fiery Mountain, which is a steep hike to a series of lookouts both of the Da'an River and of the thick conglomerate successions that are characteristics of the upper Toukoshan Formation (Chen et al., 2001b). The Toukoshan Formation comprises shallow marine strata near the base that pass upwards into thick conglomeratic intervals that are evident in many of the hills in the western foothills of Taiwan. These conglomerates are interpreted as recording deposition on the coastal plain as the large gravel-dominated river systems migrated across the flat lying surface (Fig. 6E). Sedimentation rates during deposition of the Toukoshan formation are estimated to have increased from about 1,000 m per million years at the onset of deposition to nearly 1,900 m more recently (Chen et al., 2001b; Wilcox et al., 2011).

At this stop, we will observe the Da'an River as it occurs most of the time and compare it to the width of the diked braid plain. This is a good example of the magnitude of outflow that is expected during typhoons. We will also observe the thick conglomerates of the Toukoshan Formation that are exposed in the western foothills and that were deposited on the nearby coastal plain (Fig. 12).



Figure 12 – Panoramic of the Toukoshan Formation conglomerates exposed at Fiery Mountain.

Day 3 – Tuesday, April 28

Stop 3-1: Wu River, Guoxing – Middle to Late Miocene Nanchuang Formation *(24.0266° N, 120.8264° E)*

The outcrop of Nanchuang Formation along the Wu River at Guoxing is close in age to that observed at stop 1-1 along the Dahan River at Yingge. However, where as the more northerly Yingge outcrop preserves mainly prograding tidal flat strata, the deposits along the Wu River are interpreted as occurring in upper offshore and deeper environments. The southward deepening in depositional environments is recorded in both pre- and post-collision strata (Fig. 6), and the comparison of the Nanchuang Formation strata along the Wu River and those exposed along the Dahan River demonstrate that.

Stop 3-2: 921 Earthquake Museum of Taiwan in Wufeng – neotectonics stop *(24.0424° N, 120.6992° E)*

Near the central portion of the about 100-km long Chi-Chi rupture, the fault cuts across the sport stadium of the Kuangfu Junior High School at Wufeng and creates a 2–3 m fault scarp (Fig. 13; Angelier et al., 2003). The site has now become the earthquake museum to commemorate the loss caused by the Chi-Chi earthquake and to witness the surface rupture brought about by the earthquake.

The local fault strikes vary because the shape of the scarp was influenced by the mechanical response of the surface layers, including the stadium track cover. These local strikes do not reflect the fault geometry at depth (Fig. 13).

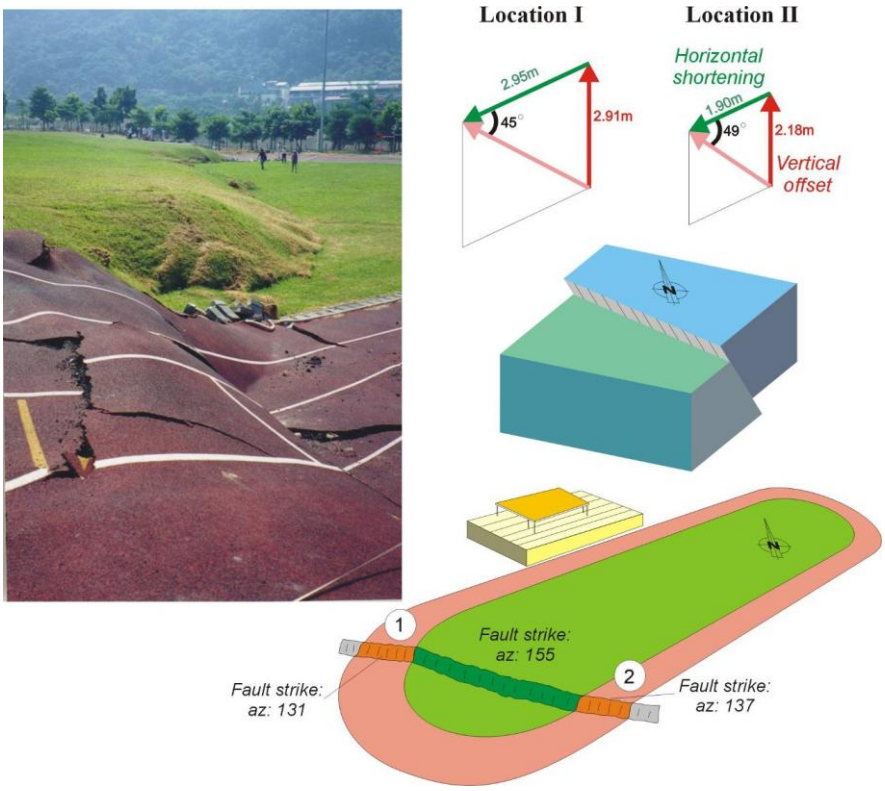


Figure 13 – Kinematics analysis and reconstruction of the movement of the fault in the Kuangfu school, in Wufeng. The earthquake fault formed a 2 m high thrust scarp that cut through the sport stadium. The lines on the running tracks allow measuring the displacements of the fault in 3 dimensions. Note that the strike of the surface fault changed because of the different mechanical properties of surface materials. The reconstructed fault geometry shows a reverse fault with a fault plane dipping 45°–50° to the east.

Stop 3-3: Zhoulan Gorge, Da'an (Ta-an) River – neotectonics stop *(24.2921° N, 120.8306° E)*

A large earthquake (Mw=7.6) occurred in west-central Taiwan in 1999 with its epicenter near the small town of Chi-Chi at a focal depth of about 10 km. The Chi-Chi rupture took place mainly along the north-south stretch of the Chelungpu Fault and cuts mainly along and within the Chinshui Shale (Fig. 14). At the northern segment of Chi-Chi rupture at Shihkang Township, the rupture turns to an easterly direction and cuts stratigraphic up-section and across the strike of the Cholan Formation. The stop in the Cholan-Neiwan area provides an opportunity for examining the Chi-Chi ruptures that formed in a conjugate pair and helped to "push up" the Tungshih anticline (Fig. 15), a décollement fold, as well as examining the coastal sediments of the Cholan Formation that were accumulated during the later stage of the foreland basin development.

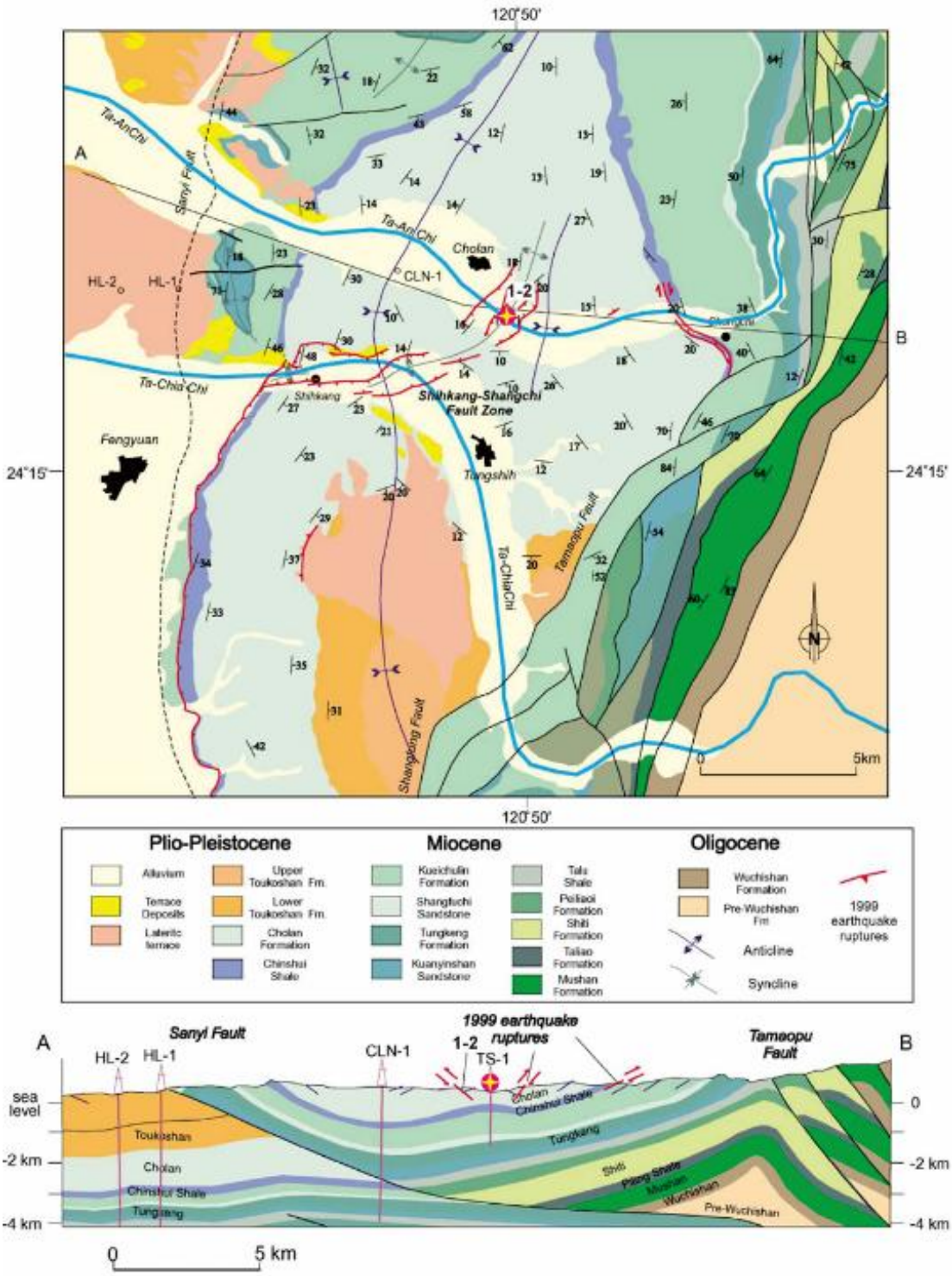


Figure 14 – Map of the northern surface ruptures of the 1999 Chi-Chi earthquake in the Shihkang-Shangchi fault zone (Lee et al., 2002). Geologic section shows that the uprising Tungshi anticline is formed by faulting and detaching along the bedding planes of the Chinshui Shale (purple-color). Note that the Tungshih anticline (at TS-1) is visible only above the detachment surface and anticline is absent beneath the detachment level (i.e., the Chinshui Shale).

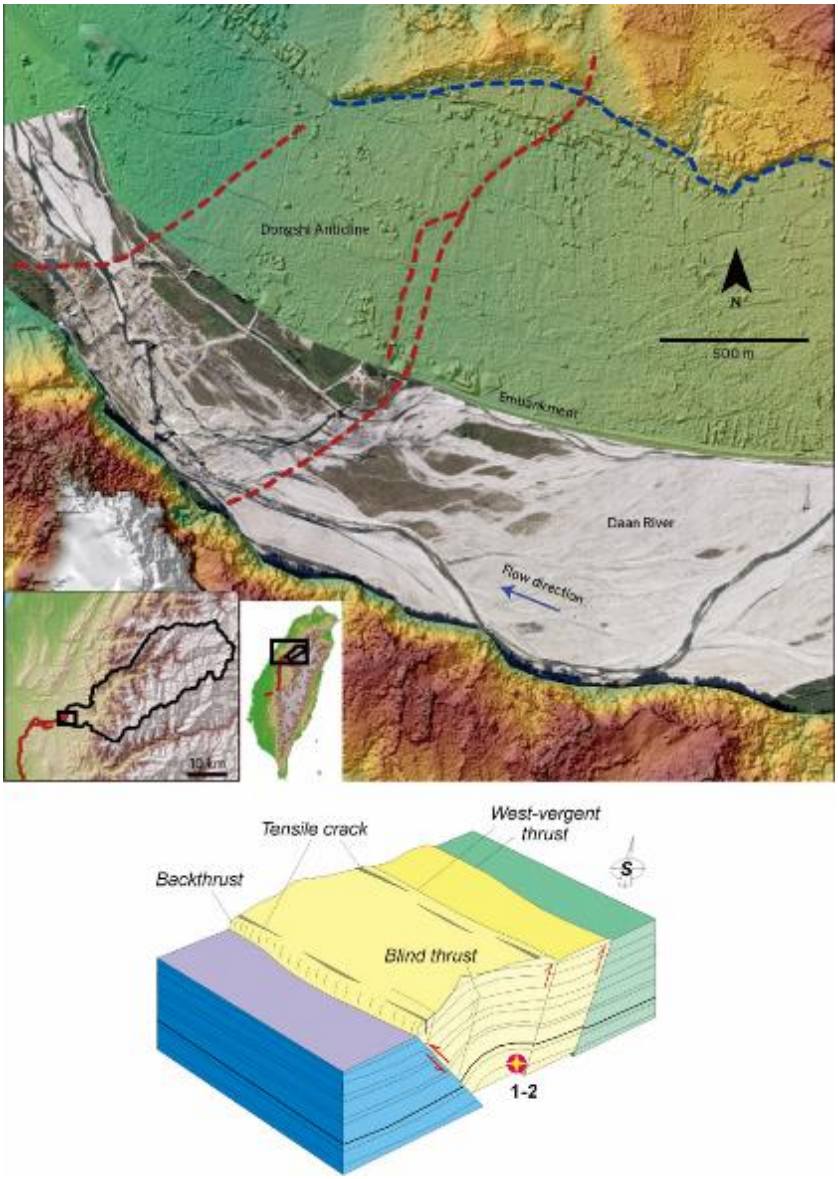


Figure 15 – Aerial photograph combined with a DEM of the surrounding area (Cook et al., 2014). Da'an (Ta-an) River valley Pop-up structure with thrust-and-backthrust system situated on a pre-existing anticlinal fold, the Tungshih anticline, in the Diaoshenshan area near Neiwan (after Lee et al., 2002). Field stop in the gorge where the river cuts through the structure is shown as red circle.

Day 4 – Wednesday, April 29

Tian Liao Moon World – Mio-Plio-Pleistocene Gutingkeng Formation

The Gutingkeng Formation, largely a thick (2600-3800 m) massive mudstone sequence well known for its badland topography, is widely exposed, occupying about 750 km^2 in southwestern Taiwan. Its age ranges from late Miocene to late Pleistocene and the sediemnts formed on the stable continental margin of the syn-collisional foreland basin (Hsieh and Knuepfer, 2001).

Recent studies using the elevation of river terraces have shown that the Moon World area was rapidly uplifted about 1500 to 1300 years ago, leading to a rapid incision of gullies and the formation of the present badland morphology (Yang et al., 2025). The combination of silt-rich, poorly consolidated material, rapid uplift, impermeable strata, and high seasonal rainfall (2000 mm/y), creates ideal conditions extremely rapid erosion with slope retreats approaching 10 cm per year (Higuchi et al., 2013)!

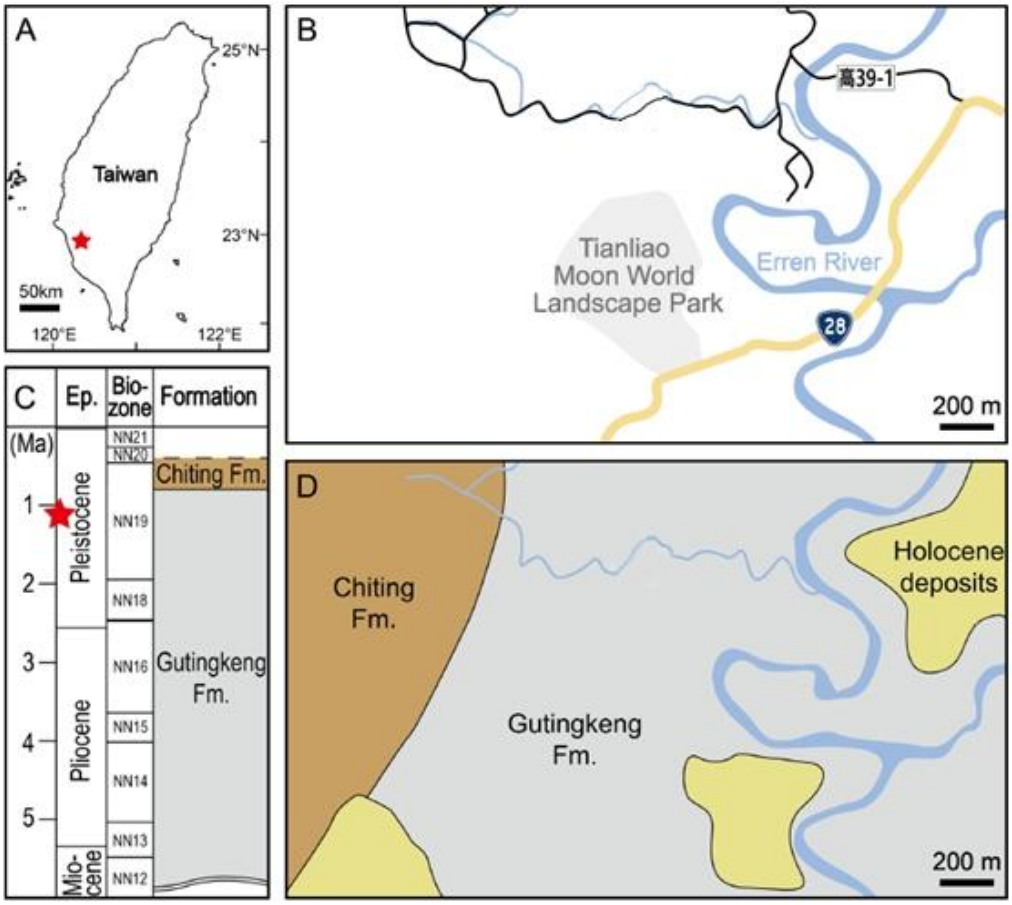


Figure 16 – A) Location of Tianliao Moon World. **B)** Geographic location. **C)** Stratigrraphic overview. **D)** Geological map. Red star marks spatangoid echinoderm site of Hsu et al. (Hsu et al., 2024).

Taitung-Chihpen Century Hotel

Hot spring hotel south of Taitung.

https://centuryhotel.com.tw/zh/

Coastal Range

The Coastal Range in eastern Taiwan, separated from the Central Range by the Huatung (Longitudinal) Valley, represents the accreted portion of the Luzon Arc which has been sutured onto the Eurasian Continent (Fig. 17).

The sequences of the Coastal Range comprise about 6000~8000 m of marine and fluvial sedimentary and volcanic rocks of Neogene-Quaternary age. Ignoring late Quaternary alluvium and terrace deposits, these rocks may be divided into four main rock-stratigraphic units (Fig. 18). From top to bottom:

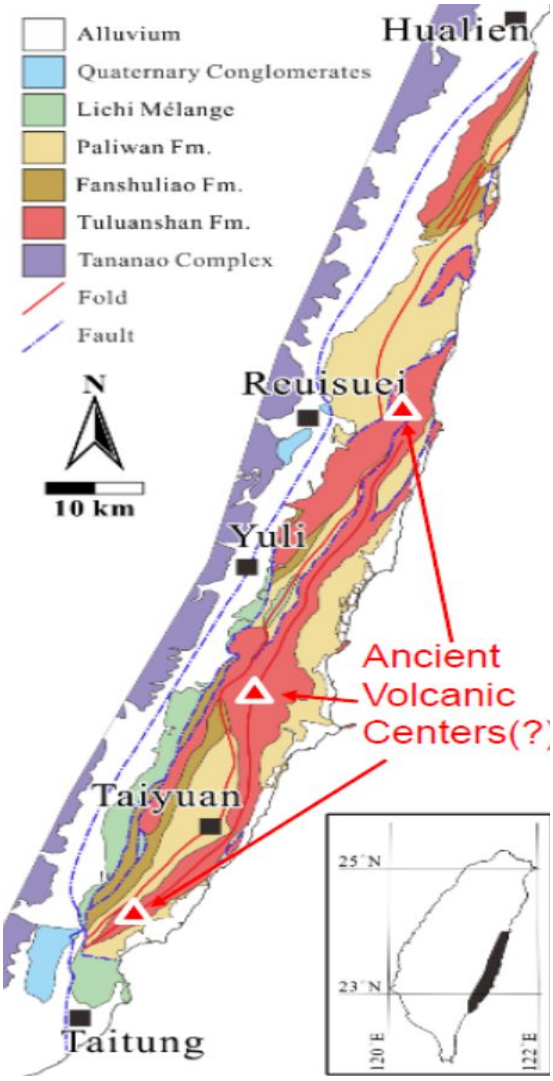


Figure 17 – Geological map of the Coastal Range with possible locations of ancient volcanic centers marked (from Larry Lai, modiefied from Wang and Chen, 1993).

1) Pinanshan Conglomerate

The Pinanshan (Peinanashan) conglomerate consists of non-marine molasse deposits in the Huatung (Longitudinal) Valley originating from the Central Range (Lee et al., 1998). The age is believed to be middle to late Pleistocene.

2) Lichi Mélange

The Lichi Mélange crops out in the southwestern part of the Coastal Range. Chaotic mudstones that contain numerous exotic blocks of various sizes consisting of ophiolites and marine sediments from the continental margin. Both matrix and clasts are cut by shearing.

3) Takangkou Formation

Pliocene-Pleistocene deep-sea turbidites that are further divided into the Fanshuliao and Paliwan Formations.

Paliwan Formation consists of turbidites ranging from conglomeratic facies (Shuilien Conglomerate) in the north, sandy facies in the middle, and shaly facies in the south.

Fanshuliao Formation consists of fine-grained turbidites conformabley overlying the Tuluanshan Formation. Slumps and slide blocks up to hundreds of meters in size are common. The Fanshulio Formation is interpreted to be mass-flow deposits laid down in a base-of slope setting.

4) Tuluanshan Formation

Miocene volcanic and volcanoclastic rocks representing the remnant Luzon Island Arc. Fission track ages show gradually younging ages from north to south, with ages from about 16 Ma in the northern part of the Coastal Range to as young as 20 ky for the outlying Lanyu Island, which represents the southward modern extension of the Luzon Arc (Yang et al., 1995). Most of the volcanics are made up of andesite, with some basalt and dacite. Sometimes reefal limestones (Kangkou Formation) are intercalated in the upper parts of the Tuluanshan Formation.

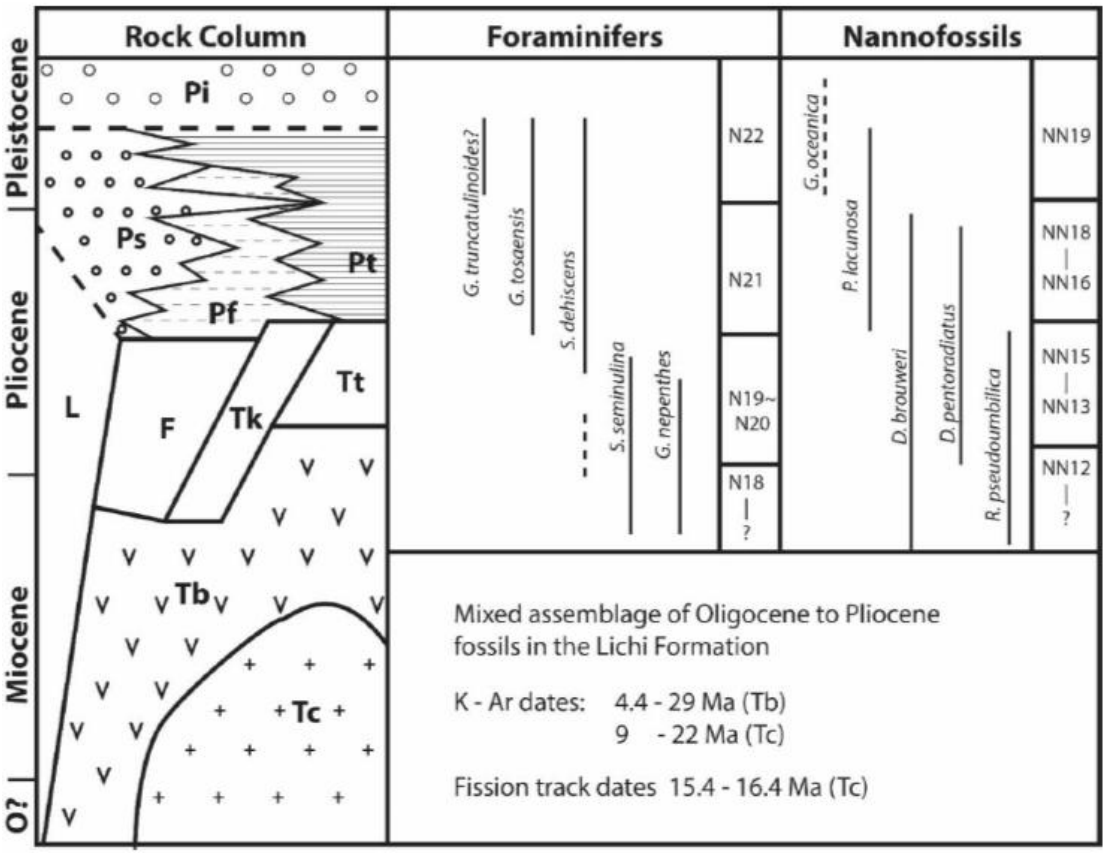


Figure 18 – Generalized stratigraphic column and biostratigraphy of the Coastal Range. (Redrawn from Teng et al., 1988). L: Lichi Formation; Tx: Tuluanshan Formation (Tk: Kangkou Limestone; Tt: Shihtiping Tuff; Tb: Shihmen Breccia; Tc: Chimei Andesite); Px: Paliwan Formation (Ps: Shuilien Conglomerate; Pt: Taiyuan Member; Pt: Futien Member); F: Fanshuliao Formation; Pi: Pinanshan Conglomerates.

Field Stops in the Southern Coastal Range – Day 5

Stop 5-1: Lichi (Liji) Melange

The Lichi Mélange type locality is situated close to the Lichi (Liji) village at the southernmost end of the Coastal Range, but outcrops of the Lichi Mélange can be found in a narrow band along the western side of the Coastal Range for about 70 km (Fig. 19). The mélange consists of more than 1 km thick mudstones (Meng and Chiang, 1965) mixed with various exotic clasts, such as ophiolites, sandstones, greywackes, limestones, and andesitic conglomerates. Ophiolite fragments, known as the East Taiwan Ophiolite, contain a typical ophiolitic suite from peridotite, gabbro, serpentinite, diabasic dikes, plagiogranite, to basalt and red clay, and display shearing and disorganized features typical for mélanges (e.g., Page and Suppe, 1981; Teng, 1981). Geochemical and geochronological evidence indicates that the ophiolite originated from subducted South China Sea oceanic crust (Hsieh et al., 2017; Lo et al., 2020), and micro/nannofossil ages indicate a range from the Oligocene to the Pliocene (Chi, 1982). Two main hypotheses have been put forward to explain the Lichi Mélange: 1) A tectonic mélange that is formed through fault shearing along the subduction interface, 2) An olistostrome which is rock mixture due to extraordinary and repeating submarine mass-wasting (cf. Chang et al., 2001).

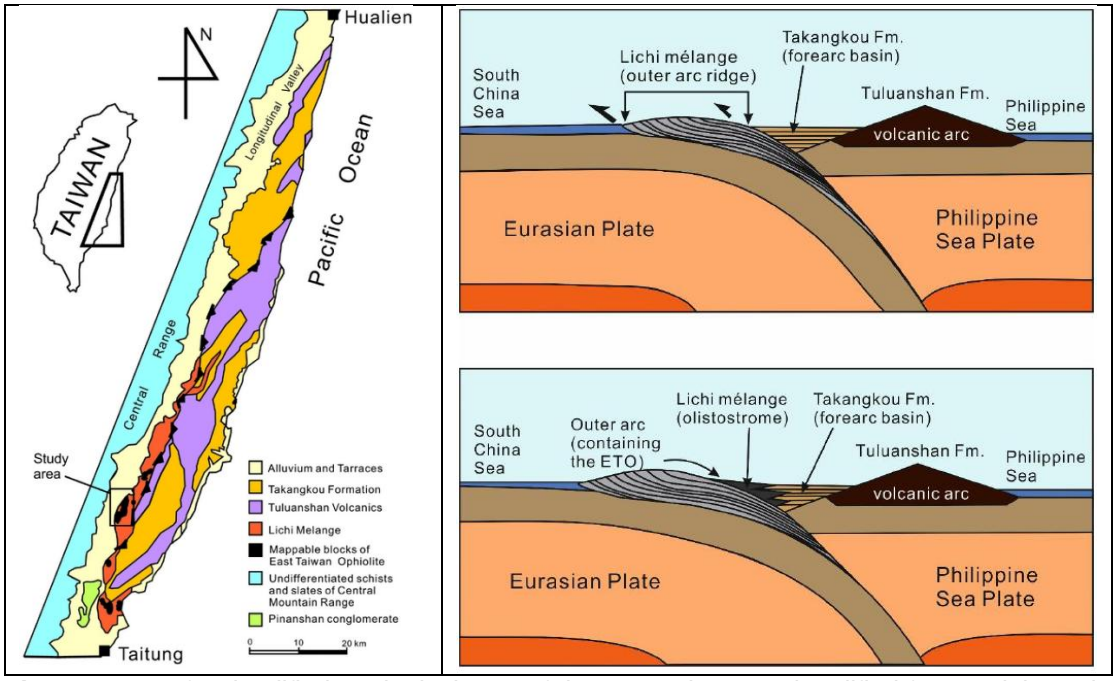


Figure 19 – Left: Simplified geological map of the Coastal Range (modified from Hsieh et al., 2017). Right: The two main hypotheses for the formation of the Lichi Mélange. Top, the "subduction complex" origin, and bottom, the "olistostrome" origin (modified from Chang et al., 2001).

Stop 5-2: Xiaoyehliu Overturned Turbidites (Fukang)

The overturned sandy turbidites at Xiaoyehliu are actually part of a huge (>1 km) exotic block in the the Lichi Mélange. In the exposed groves in between the cuestas running perpendicular to the shore, climbing ripples, dewatering structures such as flames, dishes and pillars can be seen. With a late Miocene age (Chi, 1981), these turbidities are similar in age to similar turbidites in southernmost Taiwan at Jialeshui. Also, zircon dating results show similar patterns to the turbidites in Jialeshui, but distinctly different

from the turbidites in the Coastal Range. Coral carbonates capping the sandstones and boring bivalves penetrating the sandstone surface (Fig. 20) show ages ranging from hundreds to almost 10 ka (Peng et al., 1977; Yamaguchi and Ota, 2004).

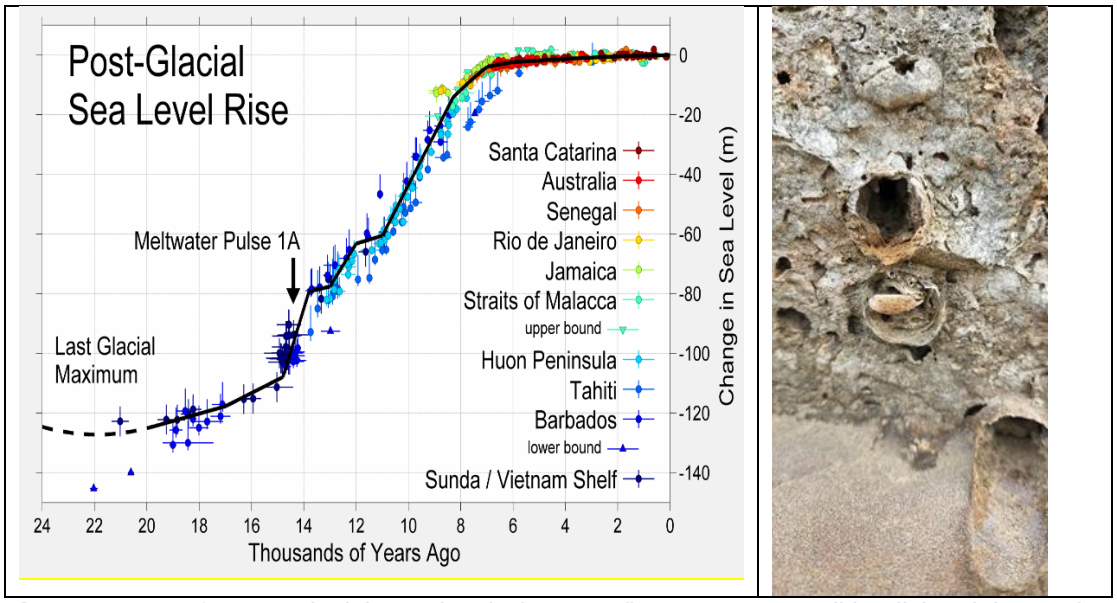


Figure 20 – Left: Post-glacial sea level changes (image source Wikipedia). Right: Boring bivalves penetrating both coral limestone and the turbidites.

Stop 5-3: Shiyushan (Umbrella Rock) Paliwan Formation

The Paliwan Formation is generally dominated by conglomeratic facies in the north, sandy facies in the middle, and shaly facies in the south (Teng, 1982). At Shiyusan, a thick sandstone bed in the turbidites of the Paliwan Formation has weathered out as a distinct promontory and sea stacks stretching several hundred meters into the Pacific Ocean. The name Shyyusan (Umbrella Rock) comes from the large block of reef limestone that balances on top of a pedestal rock by the entrance to the harbor. Within the thick sandstone bed, numerous clasts can be observed. Along the coastal cliff inside of the little harbor, almost vertically inclined thin-bedded muddy and sandy turbidites are exposed.

Stop 5-4: Baxiandong Uplifted Sea Caves (optional)

At Baxiandong, more than 10 sea caves have been uplifted to elevations ranging from 20 m to over 100 m above sea level. Both beach deposits and archeological artifacts indicate that the caves formed at sea level. Archeological finds suggest that the caves may have been inhabited as early as 30 ka (Changbin Culture; https://www.eastcoast-nsa.gov.tw/), while charcoal from the Chaoyin Cave has been radiocarbon dated to around 6 ka (Fig. 21).

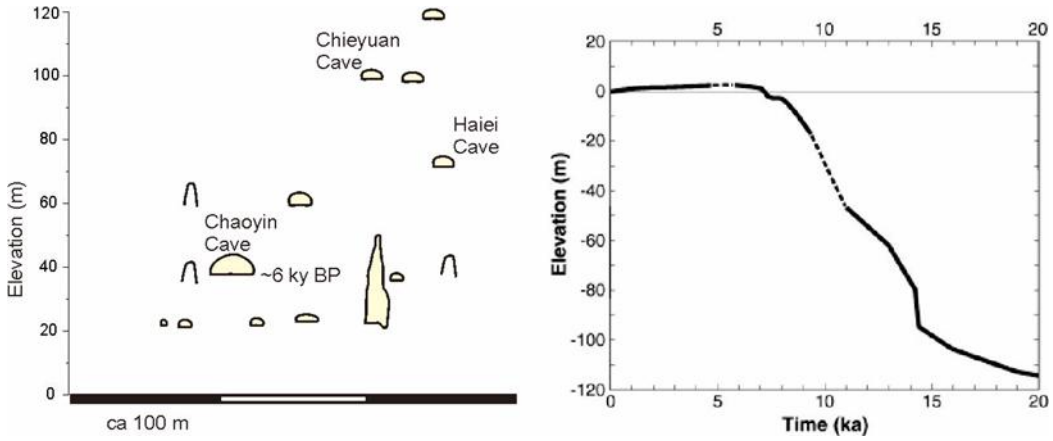


Figure 21 – Vertical distribution of the sea caves at Baxiendong (left). Global sea level curve for the past 20 ky (right)(modified from Hsieh et al., 2001).

Stop 5-5: Tropic of Cancer

The Tropic of Cancer is the northern boundary on Earth that can receive direct overhead sunlight. Today, the position of the Tropic of Cancer is at 23°26'09.2″ N, but because of the cyclic change in Earth's obliquity, the latitude is shifting by approximately 15 m per year. In 1917, the circle's position was at exactly 23°27'N, and in 2045 it will be at 23°26'N. Consequently, the monument is no longer in the exact location!

Stop 5-6: Chimei Turbidites and Chimei Fault (optional)

On the eastern/northern riverbank turbidites of the Paliwan Formation are exposed on the river bed and on the steep cliffs upstream of the bridge crossing the Hsiukulan River. To the southern/western side of the river, the Chimei Fault brings the volcanics of the Tuluanshan Formation in direct contact with the Paliwan Formation (Fig. 22).

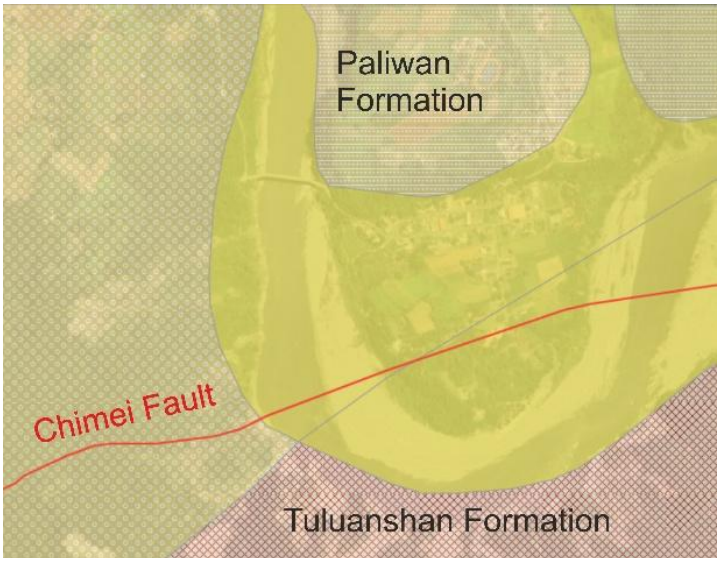


Figure 22 – Geological map overlaid onto Google satellite image of the area where the Yuanshanqimei Bridge crosses the Hsiukulan River in Chimei. Access to the river is from the river-rafting starting platform a few hundred meters south of the bridge.

Stop 5-7: Derwu Viewpoint

The Hsiukulan River with its head waters on the eastern slopes of the Central Range is the only river that crosses the Coastal Range and is believed to be an antecedent river that has been able to erode the rapidly uplifting mountain range. From the Derwu Viewing Platform, a number of tall terraces can be seen where the river enters the mountain range (Fig. 23). The terraces are mostly of strath type, overlain by relatively thin (5-7 m) fluvial sediments. Dating of the terraces indicates incision rates of 1-2 cm per year.

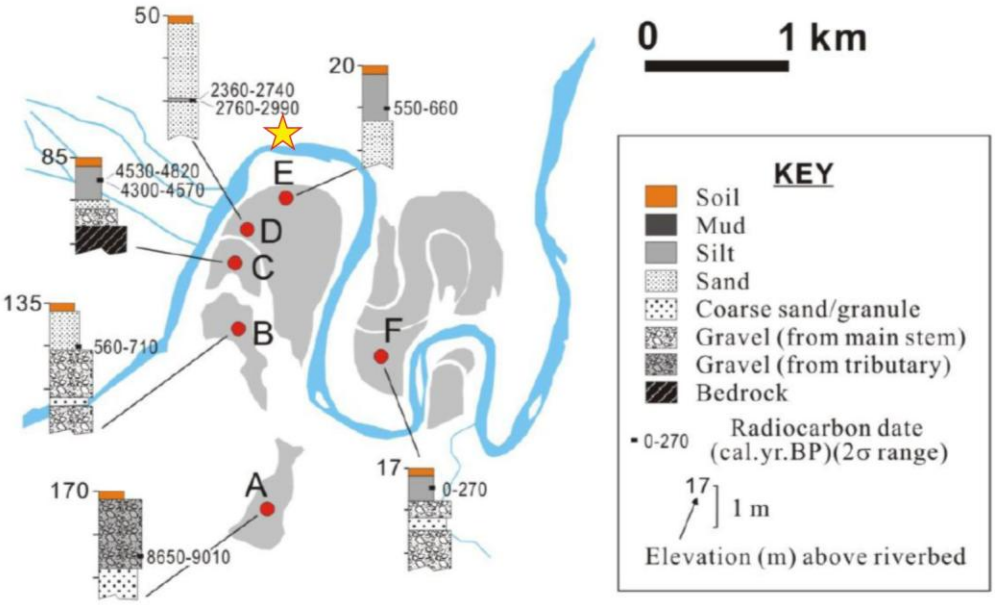


Figure 23 – Derwu River terraces (gray-shaded areas) with radiocarbon dated lithostratigraphic columns (Shyu et al., 2005). Yellow star marks approximate position of viewing platform.

Hoya Spa Hotel

Hot spring hotel in the Ruisuei Village at the foot of the Central Range.

http://www.hoya-spa.com.tw/

Field Stops in the Northern Coastal Range Stops – Day 6

Stop 6-1: Shitiping White Tuffs

The outcrop at Shihtiping is characterized by the presence of lava flows, white ignimbrites, agglomerates with plastic deformation, tuffs and tuffaceous sandstones and conglomerates from lower to upper sections (Fig. 24). It is about 100 meters in thickness and overlies the poorly columnar-jointed lavas of the Shihmen volcanic breccias. Deposition of the Shihtiping White Tuff is later than the late Miocene as indicated by the fossil ages of the sediments at its base. Both glass-rich and crystal-rich tuffs have been identified. They are the products of ash-fall, surge and pyroclastic flows. The ash-fall tuffs are thinly-bedded with fine-grained glasses and crystals in alternations and are well-sorted. The volcanic surge deposits, the base surges, are represented by the coarse-grained tuffs and lapillistones with massive, planar and dune-like sedimentary structures. Many sedimentary structures such as cross bedding, parallel lamination, normal and reserve graded beddings, impacted sag blocks, plastic deformations and erosion surface can be observed in the outcrops. Optical and scanning electron microscopic studies show that they are highly vesiculated and slightly welded. White volcanic bombs are andesitic to dacitic, and consist of plastic, welded, and impacted structures in the outcrops. These deformed structures show that the pyroclastic flows were still high in temperature during transportation and deposition. This evidence suggests that these pyroclastic flows erupted and were deposited in a subaerial environment (Song and Lo, 1988). In some sections, peperite formed inside the white volcanic bombs because of the hot flow mingling with water or wet unconsolidated sediments. White volcanic bombs and pumice contain abundant vesicles with various shapes because of subaerial explosions. Lithic fragments in the ignimbrites are blackish, greenish, and reddish, and subangular to angular. The essential mineral constituents of the Shitiping White Tuff are plagioclase, hornblende, hypersthenes, augite and magnetite listed in decreasing amount. The phenocrysts or crystal fragments are less than 50 percent, and the matrix is mainly glassy. Xenolithes of pyroxenite and hornblende gabbro can also be found at Shitiping.

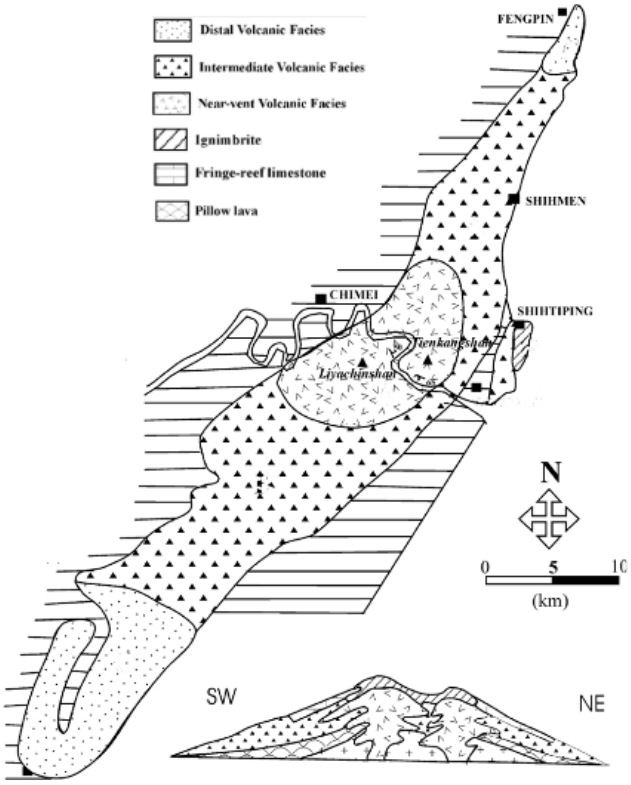


Figure 24 – Lithofacies of the area around Shitiping and a reconstruction of the Chimei volcanic island (modified from Song and Lo, 1988).

Stop 6-2: Niushan Huting – Slabs and blocks of shallow marine conglomerate

The outcrop is located close to the boundary of the volcanic Tuluanshan Formation and the Paliwan Formation (Taiyuan Member) (Fig. 25).

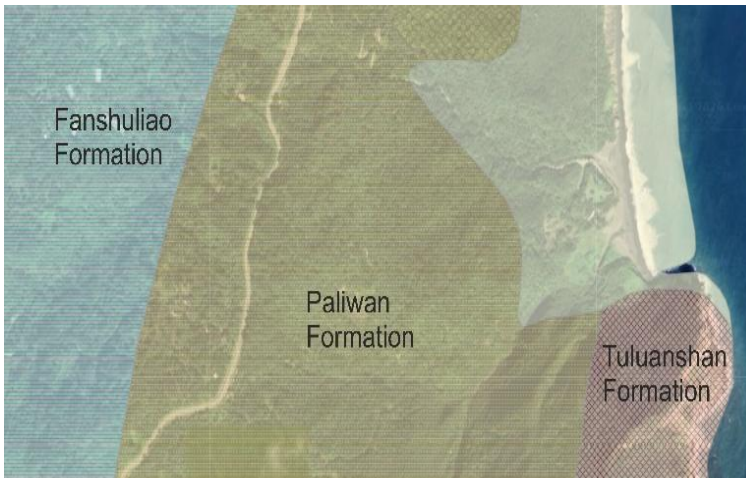


Figure 25 – Geological map of the Niushan Huting area overlaid onto Google satellite image.

The outcrop displays an enigmatic conglomerate with shallow water components such as bivalve shells, coral fragments, and large sandstone blocks with *Bichordites*-like trace fossils (Fig. 26). Chen and Wang (1988) interpreted the conglomerates and turbidites of the Pliocene Paliwan Formation to be part of two submarine fans, Shuilien-Chi-Chi fan and Chimei fan.



Figure 26 – Shallow water components in the Shuilien Conglomerate.

Stop 6-3: Lingding (Lingding) Tuluanshan Formation volcanoclastics

At the northernmost tip of the Coastal Range, late Miocene pyroclastics of the Tuluanshan Formation related to the Yuemei volcano (Lai and Song, 2013) are exposed by the coast (Fig. 27). The rocks consist of agglomerates, conglomerates and finer-grained volcanoclastic layers showing flow structures. Zircon dating places the deposits in the Middle Miocene at around 16 Ma (Lai et al., 2018).

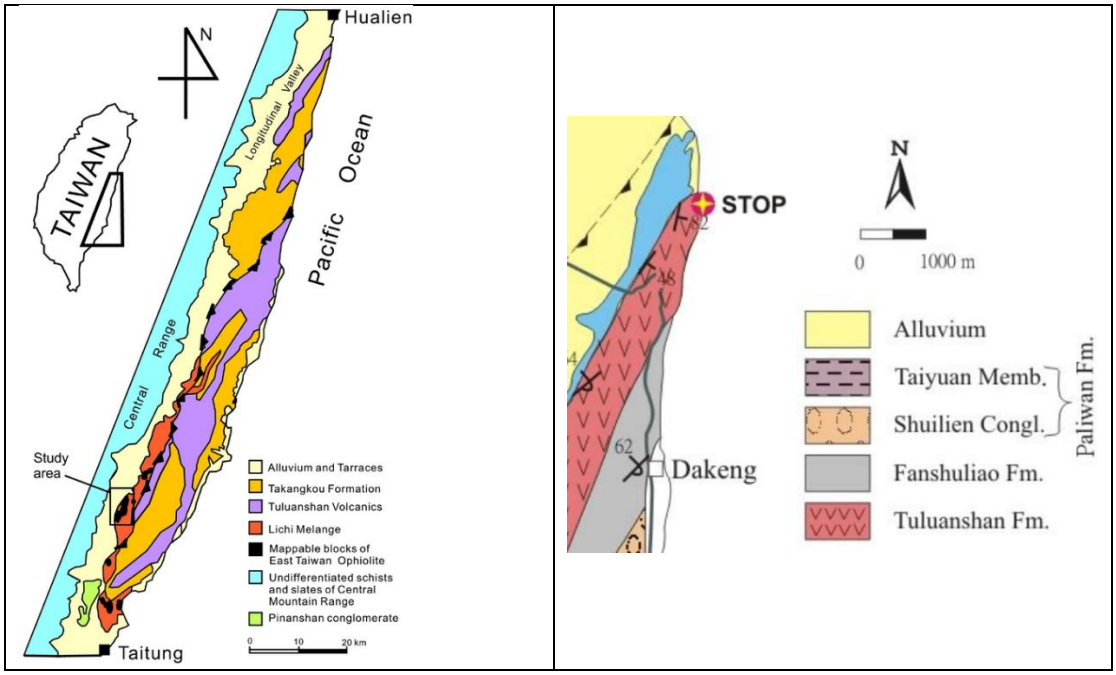


Figure 27 – Left: Simplified geological map of the Coastal Range (modified from Hsieh et al., 2017). Right: Geological map showing the northernmost part of the Coastal Range (modified from Teng et al., 2002).

Stop 6-4: Qingshui Cliffs (optional)

Chingshui Cliff is one of the most famous cliffs in Taiwan due to the huge relief from the mountains to the seafloor (Fig. 28). On the outcrop, distinct vertical normal faults with slickensides can be observed.

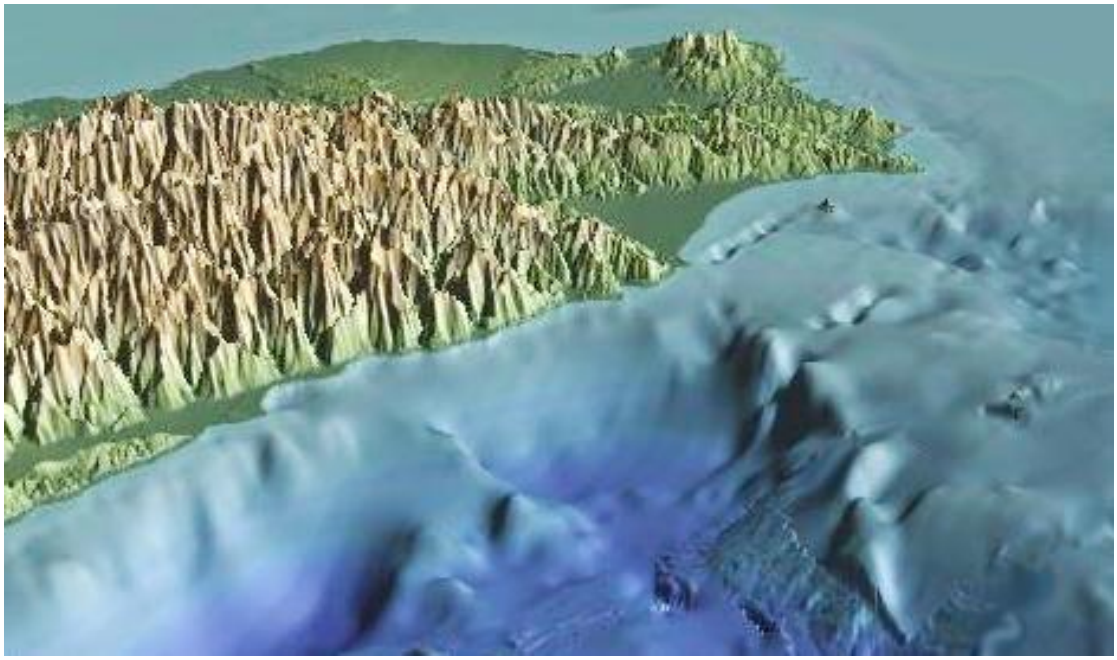


Figure 28 – Digital elevation model showing the eastern coast of Taiwan. Note how the Chingshui Cliffs dive into the Hoping Basin south of the Ryukyu Arc.

Silimu & Winwin Guest Houses, Ilan

Field Stops along the NE Coast - Day 7

The northeastern coast of Taiwan exposes Cenozoic strata representing the whole sequence from the Paleogene rifting margin, to early Neogene pre-collisional passive margin strata, and finally late Neogene collisional strata. Due to a set of reverse faults (Fig. 29), the sedimentary sequence is exposed multiple times along the coast. Because of the collision, and subsequent stress release as the collisional zone shifted southward, the uplifted thrust and fold belt has experienced two rotations: first a clockwise rotation of 30-60 ° during the collision, and then about 30 ° anticlockwise rotation during the opening of the Okinawa Trough (Sonnette et al., 2017).

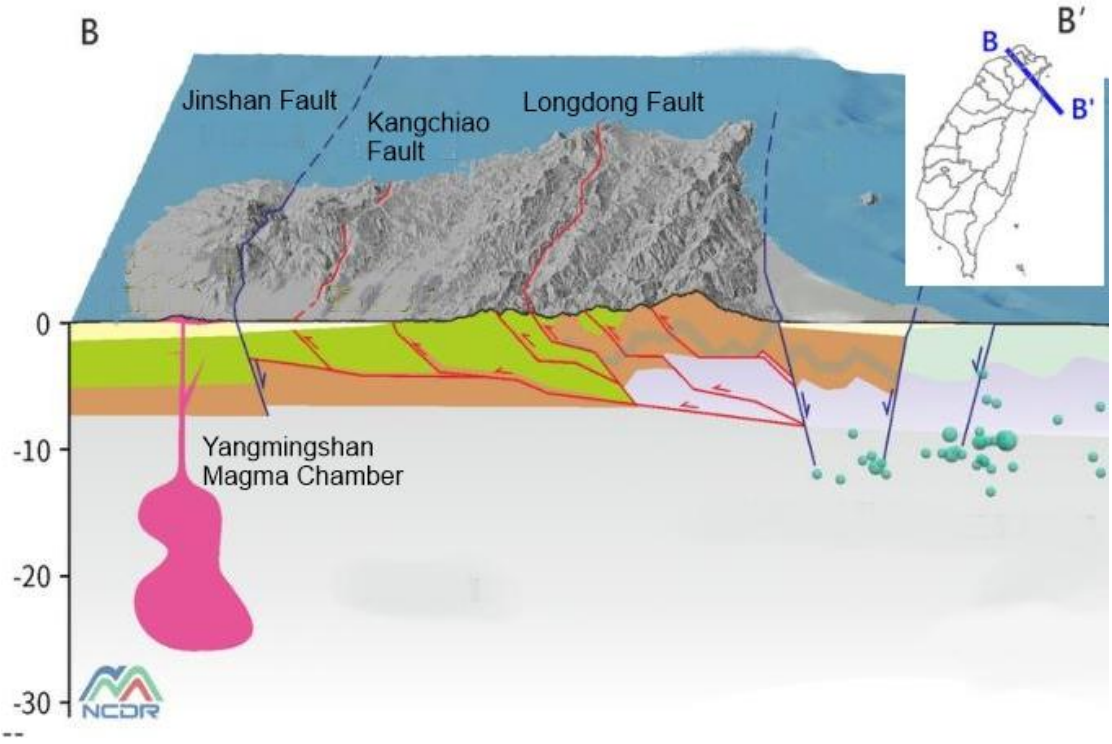


Figure 29 – Faulting related to the collision between the Philippine Sea Plate and the Eurasian margin, and subsequent opening of the Okinawa Trough (modified from NCDR, 2026).

Stop 7-1: Bitoujiao coastal platform – Miocene Kueichulin Formation *(25.1285° N, 121.9241° E)*

The cliffs and the coastal platform at Bitoujaio Geopark expose argillaceous sandstones and mudstones of the late Miocene to Pliocene Kueichulin Formation (Figure 30). Herring-bone cross-bedding, flaser-bedding, wavy bedding, as well as abundant fossils and trace fossils indicate that the sediments were deposited in an intertidal to sub-tidal environment where tidal currents played an important role. Of particular interest are a large number of crab burrows, sometimes found in conjunction with exquisitely preserved crab fossils indicating a catastrophic event killing off large numbers of crabs. Possible *Zoophycos* trace fossils have also been observed, making Bitoujiao one of the youngest shallow marine occurrences of this trace fossil.

Bitoujiao is a syncline situated at the northeastern-most tip of the Western Foothills. The name means “nose cape” and derives from the nose-like shape of the tip of the cape.

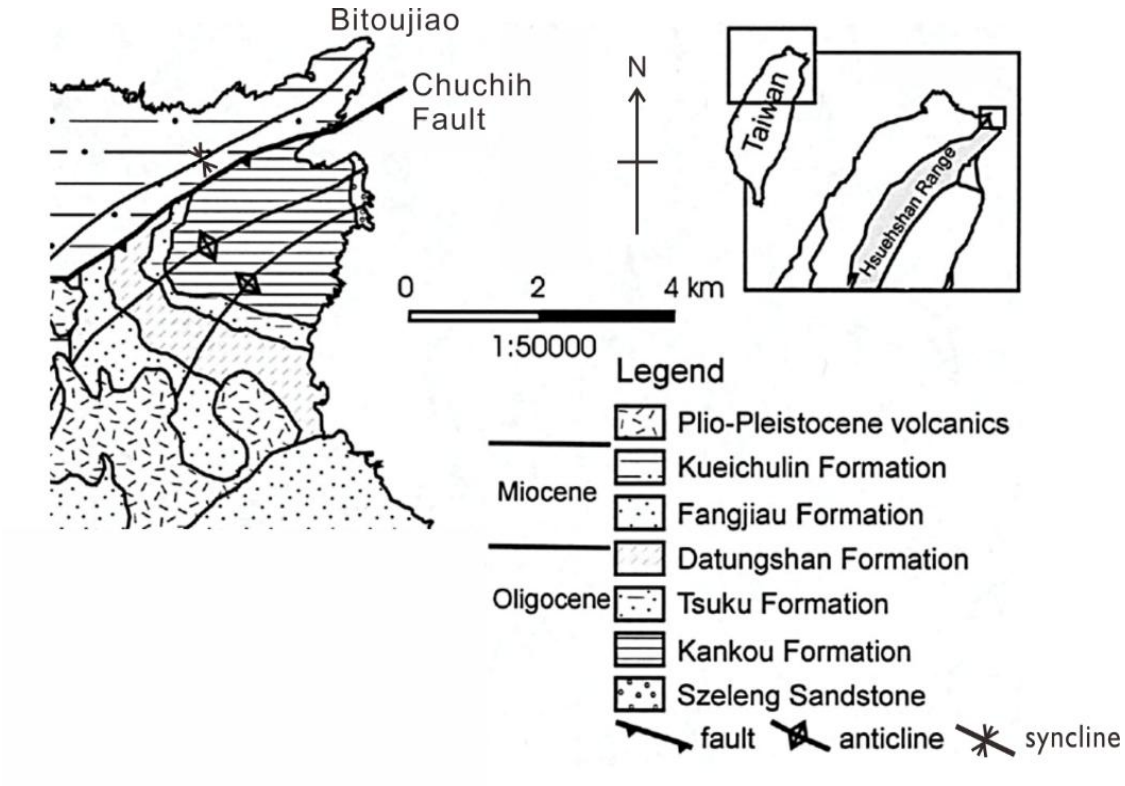


Figure 30 – Geological map of the Bitoujiao and the surrounding area (modified after Chen, 2005)

Stop 7-2: Yehliu Geopark – Miocene passive margin *(25.2084° N, 121.6936° E)*

The Miocene Taliao Formation is well exposed along the northern coast from the Yehliu peninsula to Badouzi promontory southwest of Keelung City. The formation is composed of a lower mudstone unit, a middle sandstone unit (the Yehliu Sandstone Member) (Ho et al., 1964), and an upper thin, interbedded sandstone and mudstone unit (Hong and Huang, 2000; Yen and Chen, 1953). The homoclinal nature of the strata results in a conspicuous cuesta topography with spectacular hoodoo/pedestal rocks tied to the different layers (Figs. 31 & 32). Within these sandstones, scattered lenses or layers of molluscs, echinoids and bryozoans occur. A few of the fossiliferous lenses are composed of *in situ* molluscs, mostly oysters. Accordingly, the member is interpreted as offshore bar and shoreface deposits (Hong and Wang, 1988).

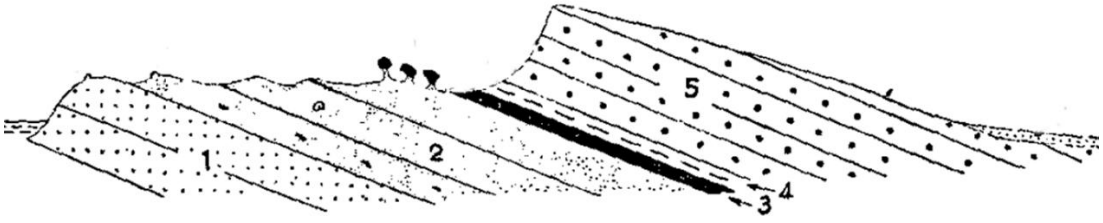


Figure 31 – Pedestal rock types are closely tied to slight differences in the sedimentary layers (Hsu, 1964) (Hong and Huang, 2001).

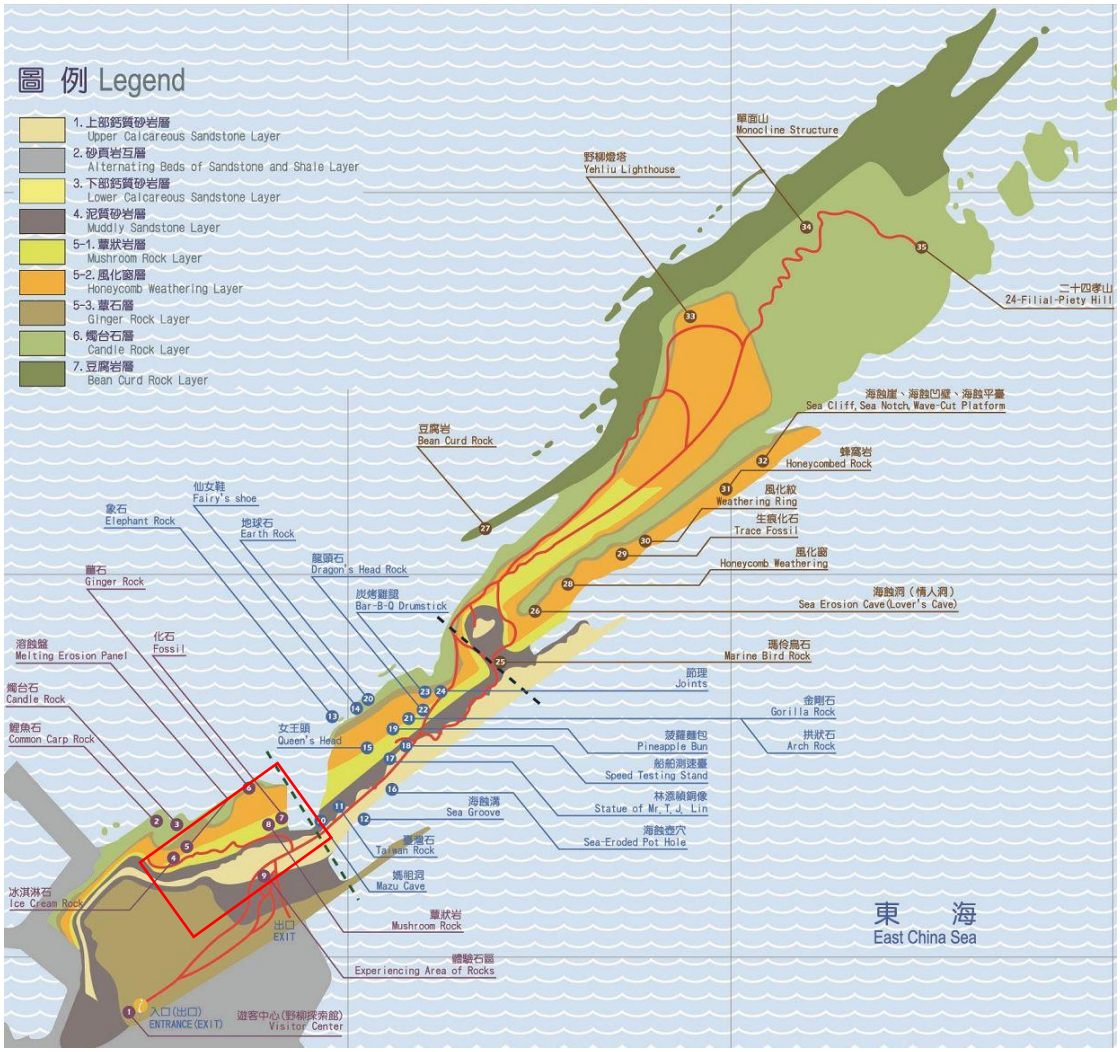


Figure 32 – Map of Yehliu Peninsula. The different colors correspond to distinctly different erosional landforms, such as mushroom rocks, ginger root rocks, or candle rocks.

The Taliao Formation and consists of lower Miocene sandstones deposited in an offshore to shoreface environment, and the formation has been subdivided into a lower mudstone member interpreted as an inner offshore environment, a middle sandstone member (Yehliu Sandstone Member) interpreted as offshore to shoreface transition, and an upper thin, interbedded sandstone and mudstone member, also related to an inner offshore environment (Hong and Wang, 1986; Miguez-Salas et al., 2022). Areas of the Yehliu Sandstone Member where the sediment consists of fairly well sorted yellowish sandstone typically contain abundant *Ophiomorpha* isp. *Phycosiphon incertum. Macaronichnus* is abundant in the topmost meter, suggesting a shallow paleoenvironment close to the shore, as *M. segregatus* is typically restricted to foreshore sediments in modern settings (cf. Seike, 2007). In contrast, areas where the strata consist of more grayish muddy sandstones, the trace fossils are dominated by *Schaubcylindrichnus,* with only few *Ophiomorpha,* suggesting a slightly deeper environment. Feeding traces (*Piscichnus Waitemata*) left by hunting stingrays feeding on worms (*Schaubcylindrichnus*) or shrimp (*Ophiomorpha*) are common in the sandstones (Löwemark, 2015) (Fig. 33).

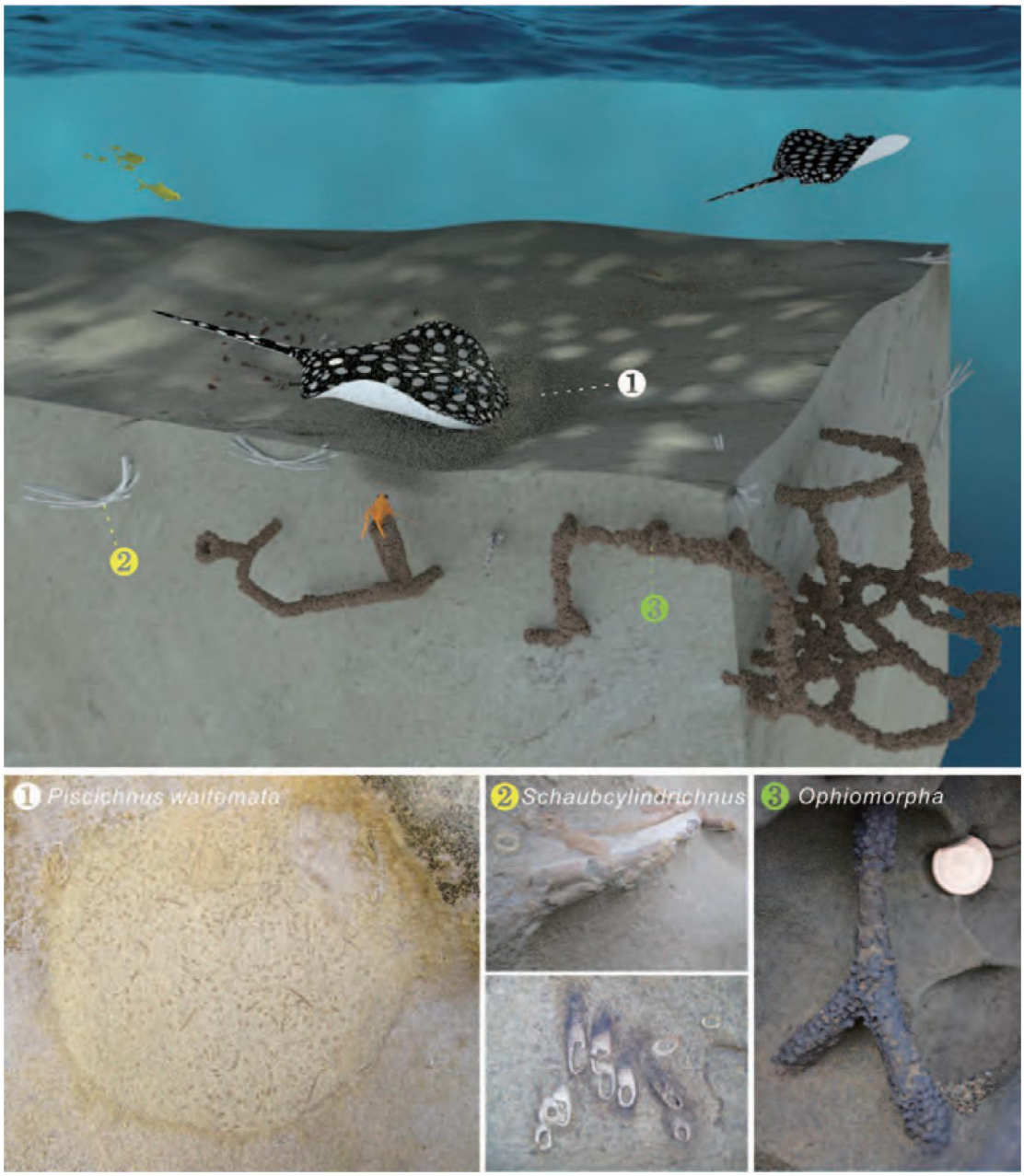


Figure 33 – Illustration demonstrating the relationship between the three most prominent trace fossils at Yehliu and their producing organisms (Chen and Shi, 2015).

Stop 7-3: Shuiwei Harbor Coastal Platform – Oligocene rifting

The Oligocene Wuchihshan Formation exposed on the coastal platform by Shuiwei Harbor in Jinshan is the oldest stratigraphic unit exposed in the Western Foothills. Sediments consist of fluviatile and transitional marine-continental facies with several coarse-grained beds of poorly sorted material. Total thickness of the formation is not known, but is believed to be at least 1000 m (Ho, 1988). The sediments are believed to have been deposited in a half-graben structure on the continental margin of the Eurasian Continent due to extensional processes during the opening of the South China Sea (Fig. 34; Chen, 2005). relative sea level changes recorded in the Oligocene strata do not correspond to global sea level changes and are therefore interpreted as a result of base-level changes related to tectonic movement of the half-graben system.

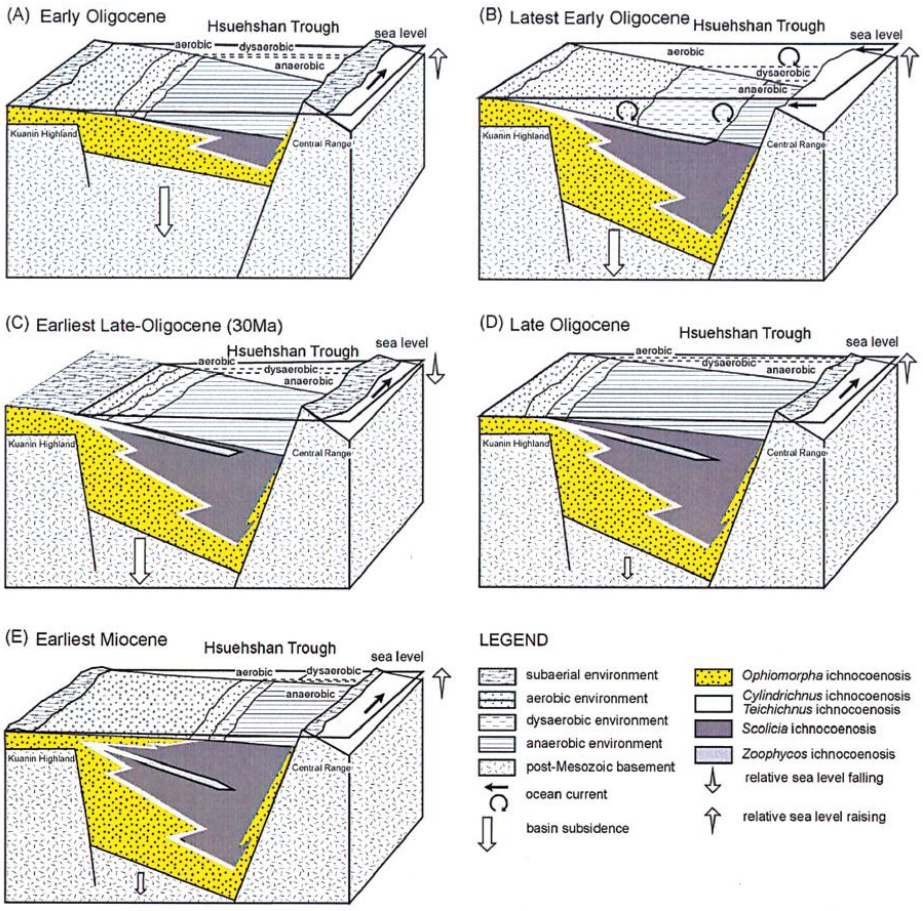


Figure 34 – Evolution of the Oligocene half-graben depositional environment on the Eurasian continental margin (Chen, 2005).

References

Angelier, J., Lee, J.-C., Hu, J.-C., Chu, H.-T., 2003. Three-dimensional deformation along the rupture trace of the September 21st, 1999, Taiwan earthquake: a case study in the Kuangfu school. Journal of Structural Geology 25, 351-370.

Boggs, J., S, Wang, W.-C., Lewis, F.S., Chen, J.-C., 1979. Sediment properties and water characteristics of the Taiwan shelf and slope. Acta Oceonographica Taiwanica 10, 10-49.

Castelltort, S., Nagel, S., Mouthereau, F., Lin, A.T., Wetzel, A., Kaus, B., Willett, S., Chiang, S.-P., Chiu, W.-Y., 2011. Sedimentology of early Pliocene sandstones in the south-western Taiwan foreland: Implications for basin physiography in the early stages of collision. Journal of Asian Earth Sciences 40, 52-71.

Chang, C., Angelier, J., Huang, C., Liu, C., 2001. Structural evolution and significance of a mélange in a collision belt: The Lichi Mélange and the Taiwan arc–continent collision. Geological Magazine 138, 633-651. .

Chang, C.P., Yeh, T.-C., Chen, J.M., 1993. Effects of terrain on the surface structure of typhoons over Taiwan. Monthly Weather Review 121, 734-752.

Chang, Q., Hren, M.T., Lai, L.S.-H., Dorsey, R.J., Byrne, T.B., 2023. Rapid topographic growth of the Taiwan orogen since ~1.3-1.5 Ma. Science Advances 9.

Chang, S.S.L., Chi, W.-R., 1983. Neogene nannoplankton biostratigraphy in Taiwan and the tectonic implications. Petroleum Geology of Taiwan 19, 93-147.

Chen, C.-W., Oguchi, T., Hayakawa, Y.S., Saito, H., Chen, H., Lin, G.-W., Wei, L.-W., Chao, Y.-C., 2018. Sediment yield during typhoon events in relation to landslides, rainfall, and catchment areas in Taiwan. Geomorphology 303, 540-548.

Chen, T.-T., Shi, L.-Y., 2015. 中新世大寮層發現: 魟魚掠食海蛄蝦之證據. Ti-Chih 34, 78-81.

Chen, W.-S., 2005. Characteristic trace fossils from shoreface to offshore environments of an Oligocene succession, Northeastern Taiwan. TAO 16, 1097-1120.

Chen, W.-S., Ridgway, K.D., Horng, C.-S., Chen, Y.-G., Shea, K.-S., Yeh, M.-G., 2001a. Stratigraphic architecture, magnetostratigraphy, and incised-valley systems of the Pliocene-Pleistocene collisional marine foreland basin of Taiwan. Geological Society of America Bulletin 113, 1249-1271.

Chen, W.-S., Ridgway, K.D., Horng, C.-S., Chen, Y.-G., Shea, K.-S., Yeh, M.-G., 2001b. Stratigraphic architecture, magnetostratigraphy, and incised-valleysystems of the Pliocene-Pleistocene collisional marine foreland basin of Taiwan. GSA Bulletin 113, 1249-1271.

Chen, W., Wang, Y., 1988. The Plio-Pleistocene basin development in the Coastal Range of Taiwan. ACTA Geol. Taiwanica 26, 37-56.

Chi, W., 1981. Stratigraphic record of plate interactions in the Coastal Range of eastern Taiwan. Memoir of the Geological Society of China 4, 155-194.

Chi, W.R., 1982. The calcareous nannoplankton of the Lichi Melange and the Kenting Melange and their significance in the interpretation of Plate-Tertiaires of the Taiwan Region. Ti-Chi.

Chien, F.-C., Kuo, H.-C., 2011. On the extreme rainfall of Typhoon Morakot (2009). Journal of Geophysical Research 116.

Cook, K.L., Turowski, J.M., Hovius, N., 2014. River gorge eradication by downstream sweep erosion. Nature Geosci 7, 682-686.

Covey, M., 1984. Lithofacies analysis and basin reconstruction, Plio-Pleistocene Western Taiwan Foredeep. Petroleum Geology of Taiwan 20, 53-83.

Dadson, S.J., Hovius, N., Chen, H., Dade, W.B., Hsieh, M.-L., Willett, S.D., Hu, J.-C., Horng, M.-J., Chen, M.-C., Stark, C.P., Lague, D., Lin, J.-C., 2003. Links between erosion, runoff variability and seismicity in the Taiwan orogen. Nature 426, 648-651.

Dadson, S.J., Hovius, N., Chen, H., Dade, W.B., Lin, J.-C., Hsu, M.-L., Lin, C.-W., Horng, M.-J., Chen, T.-C., Milliman, J., Stark, C.P., 2004. Earthquake-triggered increase in sediment delivery from an active mountain belt. Geology 32, 733-736.

Dashtgard, S.E., Hsieh, A.I., Vaucher, R., Löwemark, L., 2026. Controls on the ichnology of late miocene–pliocene shallow-marine strata during uplift of the Taiwan Orogen: A semi-quantitative approach. Palaeogeography, Palaeoclimatology, Palaeoecology 692.

Dashtgard, S.E., Löwemark, L., Vaucher, R., Pan, Y., Pilarczyk, J., Castelltort, S., 2020. Tropical cyclone deposits in the Pliocene Taiwan Strait: Processes, examples, and conceptual model. Sedimentary Geology 405.

Dashtgard, S.E., Löwemark, L., Wang, P.-L., Setiaji, R.A., Vaucher, R., 2021. Geochemical evidence of tropical cyclone controls on shallow-marine sedimentation (Pliocene, Taiwan). Geology 49, 566-570.

Droser, M.L., Gehling, J.G., Jensen, S., 1999. When the worm turned: concordance of Early Cambrian ichnofabric and trace-fossil record in siliciclastic rocks of South Australia. Geology 27, 625-628.

Higuchi, K., Chigira, M., Lee, D.-H., 2013. High rates of erosion and rapid weathering in a Plio-Pleistocene mudstone badland, Taiwan. CATENA 106, 68-82.

Ho, C.S., 1988. An introduction to the geology of Taiwan: explanatory text of the geology map of Taiwan, 2nd ed. Ministry of Economic Affaires, R.O.C., p. 192.

Ho, C.S., Hsu, M.Y., Jen, L.S., Fong, G.S., 1964. Geology and coal resources of the northern coastal area of Taiwan. Bulletin of the Geological Survey of Taiwan 15, 1-23.

Hong, E., Huang, E., 2000. The formation of the pedestal rocks in the Taliao Formation, northern coast of Taiwan. Journal of the Geolological Society of China 44, 43-72.

Hong, E., Huang, E., 2001. Formation of the pedestal rocks in the Taliao Formation, northeastern coast of Taiwan. Western Pacific Earth Sciences 1, 99-106.

Hong, E., Wang, Y., 1986. Sedimentary structures and trace fossils in the Wuchihshan formation, Waiwulun Area, northern Taiwan. Ti-Chih 7, 11-30.

Hong, E., Wang, Y., 1988. Basin analysis of the upper Miocene-lower Pliocene series in northwestern foothills of Taiwan. Ti-Chih 8, 1-20.

Horng, C.-S., Shea, K.-S., 1996. Dating of the Plio-Pleistocene rapidly deposited sequence based on integrated magneto-biostratigraphy: A case study of the

Madagida-Chi section, coastal range, eastern Taiwan. Journal of the Geological Society of China 39, 31-58.

Hsieh, A.I., Dashtgard, S.E., Clift, P.D., Lo, L., Vaucher, R., Löwemark, L., 2023a. Competing influence of the Taiwan orogen and East Asian Summer Monsoon on South China Sea paleoenvironmental proxy records. Palaeogeography, Palaeoclimatology, Palaeoecology 635.

Hsieh, A.I., Dashtgard, S.E., Wang, P.L., Horng, C.S., Su, C.C., Lin, A.T., Vaucher, R., Löwemark, L., 2023b. Multi-proxy evidence for rapidly shifting sediment sources to the Taiwan Western Foreland Basin at the Miocene–Pliocene transition. Basin Research 34, 932-948.

Hsieh, A.I., Vaucher, R., Löwemark, L., Dashtgard, S.E., Horng, C.S., Lin, A.T., Zeeden, C., 2023c. Influence of a Rapidly Uplifting Orogen on the Preservation of Climate Oscillations. Paleoceanography and Paleoclimatology 38.

Hsieh, M.-L., Knuepfer, P.L.K., 2001. Middle–late Holocene river terraces in the Erhjen River Basin, southwestern Taiwan—implications of river response to climate change and active tectonic uplift. Geomorphology 38, 337-372.

Hsieh, R.B.J., Shellnutt, J.G., Yeh, M.-W., 2017. Age and tectonic setting of the East Taiwan Ophiolite: implications for the growth and development of the South China Sea. Geological Magazine 154, 441-455.

Hsu, C.-H., Lin, J.-P., Lin, C.-H., 2024. A spatangoid echinoid assemblage from the Gutingkeng Formation (Early Pleistocene) of Taiwan and its paleoenvironmental and geological implications. Geobios.

Hsu, S.-C., Kao, S.-J., Jeng, W.-L., 2006. Quantitative links between fluvial sediment discharge, trapped terrigenous flux and sediment accumulation, and implications for temporal and spatial distributions of sediment fluxes. Deep Sea Research Part I: Oceanographic Research Papers 53, 241-252.

Hsu, T.L., 1964. Hoodoo rocks at Yehliu, northern coast of Taiwan. Bulletin of the Geological Survey of Taiwan 15, 37-43.

Huang, C.-S., 2005. Explanatory text of the geological map of Taiwan. Taipei, 3 ed. Central Geological Survey, Taipei.

Huh, C.-A., Chen, W., Hsu, F.-H., Su, C.-C., Chiu, J.-K., Lin, S., Liu, C.-S., Huang, B.-J., 2011. Modern (<100 years) sedimentation in the Taiwan Strait: Rates and source-to-sink pathways elucidated from radionuclides and particle size distribution. Continental Shelf Research 31, 47-63.

Kao, S.-J., Jan, S., Hsu, S.-C., Lee, T.-Y., Dai, M., 2008. Sediment Budget in the Taiwan Strait with High Fluvial Sediment Inputs from Mountainous Rivers: New Observations and Synthesis. Terrestrial, Atmospheric and Oceanic Sciences 19, 525-546.

Lai, L.S.-H., Dorsey, R.J., Horng, C.-S., Chi, W.-R., Shea, K.-S., Yen, J.-Y., 2022. Extremely rapid up-and-down motions of island arc crust during arc-continent collision. Communications Earth & Environment.

Lai, Y.-M., Chu, M.-F., Chen, W.-S., Shao, W.-Y., Lee, H.-Y., Chung, S.-L., 2018. Zircon U-Pb and Hf isotopic constraints on the magmatic evolution of the Northern Luzon Arc. Terrestrial, Atmospheric & Oceanic Sciences 29.

Lai, Y.-M., Song, S.-R., 2013. The volcanoes of an oceanic arc from origin to destruction: A case from the northern Luzon Arc. Journal of Asian Earth Sciences 74, 97-112.

Lee, J.-C., Angelier, J., Chu, H.-T., Yu, S.-B., Hu, J.-C., 1998. Plate-boundary strain partitioning along the sinistral collision suture of the Philippine and Eurasian plates: Analysis of geodetic data and geological observation in southeastern Taiwan. Tectonics 17, 859-871.

Lee, J.-C., Chu, H.-T., Angelier, J., Chan, Y.-C., Hu, J.-C., Lu, C.-Y., Rau, R.-J., 2002. Geometry and structure of northern surface ruptures of the 1999 Mw=7.6 Chi-Chi Taiwan earthquake: influence from inherited fold belt structures. Journal of Structural Geology 24, 173-192.

Lin, A.T.-S., Wang, S.-M., Hung, J.-H., Wu, M.-S., Liu, C.-S., 2007. Lithostratigraphy of the Taiwan Chelungpu-Fault Drilling Project-A Borehole and Its Neighboring Region, Central Taiwan. Terrestrial, Atmospheric and Oceanic Sciences 18.

Lin, A.T.-S., Watts, A.B., Hesselbo, S.P., 2003. Cenozoic stratigraphy and subsidence history of the South China Sea margin in the Taiwan region. Basin Research 15, 453-478.

Lin, A.T., Watts, A.B., 2002. Origin of the West Taiwan basin by orogenic loading and flexure of a rifted continental margin. Journal of Geophysical Research: Solid Earth 107, ETG 2-1-ETG 2-19.

Lin, C.-W., Chen, W.-S., 2016. Geological Map of Taiwan. Geological Society of Taiwan, Taipei, Taiwan.

Lo, Y.-C., Chih-Tung, C., Lo, C.-H., Sun-Lin, C., 2020. Ages of ophiolitic rocks along plate suture in Taiwan orogen: Fate of the South China Sea from subduction to collision. TAO: Terrestrial, Atmospheric and Oceanic Sciences 31, 3.

Löwemark, L., 2015. Evidence for targeted elasmobranch predation on thalassinidean shrimp in the Miocene Taliao sandstone formation, NE Taiwan. Lethaia 48, 227-234.

Meng, C.-Y., Chiang, S.Y., 1965. Subsurface data from the wildcat SS -1, Shihshan, 1 Taitung. Petroleum Geology of Taiwan 4, 283-286.

Miguez-Salas, O., Löwemark, L., Pan, Y.-Y., Rodríguez-Tovar, F.J., 2022. Selective colonization after storm events in a delta environment: applied ichnology from the early Miocene of Taiwan. Ichnos 29, 27-39.

Milliman, J.D., Kao, S.-J., 2005. Hyperpycnal discharge of fluvial sediment to the ocean: impact of Super-Typhoon Herb (1996) on Taiwanese Rivers. The Journal of Geology 113, 503-516.

Milliman, J.D., Lin, S.W., Kao, S.J., Liu, J.P., Liu, C.S., Chiu, J.K., Lin, Y.C., 2007. Short-term changes in seafloor character due to flood-derived hyperpycnal discharge: Typhoon Mindulle, Taiwan, July 2004. Geology 35, 779-782.

MOEA, C.G.S.o.T., 2019. Geology of Taiwan, https://www.moeacgs.gov.tw/english2/twgeol/. Central Geological Survey, Taiwan.

Nagel, S., Castelltort, S., Garzanti, E., Lin, A.T., Willett, S.D., Mouthereau, F., Limonta, M., Adatte, T., 2014. Provenance Evolution During Arc-Continent Collision:

Sedimentary Petrography of Miocene To Pleistocene Sediments In the Western Foreland Basin of Taiwan. Journal of Sedimentary Research 84, 513-528.

Nagel, S., Castelltort, S., Wetzel, A., Willett, S.D., Mouthereau, F., Lin, A.T., 2013. Sedimentology and foreland basin paleogeography during Taiwan arc continent collision. Journal of Asian Earth Sciences 62, 180-204.

Nagel, S., Granjeon, D., Willett, S., Lin, A.T.-S., Castelltort, S., 2018. Stratigraphic modeling of the Western Taiwan foreland basin: Sediment flux from a growing mountain range and tectonic implications. Marine and Petroleum Geology 96, 331-347.

Page, B.M., Suppe, J., 1981. The Pliocene Lichi melange of Taiwan; its plate-tectonic and olistostromal origin. American Journal of Science 281, 193-227.

Pan, T.-Y., Lin, A.T.-S., Chi, W.-R., 2015. Paleoenvironments of the evolving Pliocene to early Pleistocene foreland basin in northwestern Taiwan: An example from the Dahan River section. Island Arc 24, 317-341.

Peng, T.-H., Li, Y.-H., Wu, F.T., 1977. Tectonic uplift rates of the Taiwan Island since the early Holocene. Memoir of the Geological Society of China 2, 57-69.

Seike, K., 2007. Palaeoenvironmental and palaeogeographical implications of modern Macaronichnus segregatis-like traces in foreshore sediments on the Pacific coast of central Japan. Palaeogeogr., Palaeoclim., Palaeoec. 252, 497-502.

Shaw, C.-L., 1996. Stratigraphic correlation and isopach maps of the Western Taiwan Basin. Terrestrial, Atmospheric and Oceanic Sciences 7, 333-360.

Shyu, J.B.H., Sieh, K., Chen, Y.-G., Liu, C.-S., 2005. Neotectonic architecture of Taiwan and its implications for future large earthquakes. Journal of Geophysical Research: Solid Earth 110, B08402.

Simoes, M., Avouac, J.P., 2006. Investigating the kinematics of mountain building in Taiwan from the spatiotemporal evolution of the foreland basin and western foothills. Journal of Geophysical Research 111, B10401, 1-25.

Song, S.-R., Lo, H.-J., 1988. Volcanic geology of Fengpin-Takangkou area, coastal range of Taiwan. Yánjiū bāogāo-Guólė Táiwān dāxué. Lǐxuéyuān dėzhėxué xė, 223-235.

Sonnette, L., Lee, J.-C., Horng, C.-S., 2017. The arcuate fold-and-thrust belt of northern Taiwan: Results of a two-stage rotation revealed from a paleomagnetic study. Journal of Asian Earth Sciences 147, 284-309.

Suppe, J., 1981. Mechanics of mountain building and metamorphism in Taiwan. Memoir of the Geological Society of China 4, 67-89.

Suppe, J., 1984. Kinematics of arc-continent collision, flipping of subduction and back-arc spreading near Taiwan. Memoir of the Geological Society of China 6, 21-33.

Teng, L., 1982. Stratigraphy and sedimentation of the Suilien Conglomerate, northern Coastal Range, eastern Taiwan. Yánjiū bàogào-Guólì Táiwān dàxué. Lǐxuéyuàn dìzhìxué xì, 201-220.

Teng, L.S., 1981. On the origin and tectonic significance of the Lichi Formation, Coastal Range, eastern Taiwan. Ti-Chih 2, 51-62.

Teng, L.S., 1990. Geotectonic evolution of late Cenozoic arc-continent collision in

Taiwan Tectonophysics 183, 57-76.

Teng, L.S., Lee, J.-C., Hsu, C.-B., 2002. Soft-sediment deformation in the Fanshuiliao Formation of the Coastal Range, eastern Taiwan. Bulletin of the Central Geological Survey, Taiwan 15, 103-137.

Teng, L.S., Wang, Y., Tang, C.-H., Huang, C.-Y., Huang, T.-C., Yu, M.-S., Ke, A., 1991. Tectonic aspects of the Paleogene depositional basin of northern Taiwan. Proceedings of the Geological Society of China 34, 313-336.

Vaucher, R., Dashtgard, S.E., Horng, C.-S., Zeeden, C., Dillinger, A., Pan, Y.-Y., Setiaji, R.A., Chi, W.-R., Löwemark, L., 2021. Insolation-paced sea level and sediment flux during the early Pleistocene in Southeast Asia. Scientific Reports 11.

Vaucher, R., Dillinger, A., Hsieh, A.I., Chi, W.R., Löwemark, L., Dashtgard, S.E., 2023a. Storm-flood-dominated delta succession in the Pleistocene Taiwan Strait. The Depositional Record 9, 820-843.

Vaucher, R., Zeeden, C., Hsieh, A.I., Kaboth-Bahr, S., Lin, A.T., Horng, C.-S., Dashtgard, S.E., 2023b. Hydroclimate dynamics during the Plio-Pleistocene transition in the northwest Pacific realm. Global and Planetary Change 223.

Wang, Y., Chen, W.-S., 1993. Geologic Map of Eastern Coastal Range (Northern Sheet). Scale 1:100000. Central Geological Survey, Taipei.

Warrick, J.A., Milliman, J.D., 2003. Hyperpycnal sediment discharge from semiarid southern California rivers: Implications for coastal sediment budgets. Geology 31, 781-784.

Wilcox, T., Mueller, K., Upton, P., Chen, Y.G., Huang, S.T., Yanites, B.J., Tucker, G., 2011. Linking Taiwan's subcritical Hsuehshan Range topography and foreland basin architecture. Tectonics 30.

Wu, C.C., Cheung, K.K.W., Lo, Y.-Y., 2009. (2009), Numerical study of the rainfall event due to the interaction of Typhoon Babs (1998) and the northeasterly monsoon. Monthly Weather Review 137, 2049-2064.

Yamaguchi, M., Ota, Y., 2004. Tectonic interpretations of Holocene marine terraces, east coast of Coastal Range, Taiwan. Quaternary International 115–116, 71-81.

Yang, C.-J., Turowski, J.M., Gailleton, B., Tseng, C.-W., Chao, C.-M., Chuang, R.Y., 2025. Badland distribution as a marker of rapid tectonic activity. Scientific Reports 15, 15912.

Yang, T.F., Tien, J.-l., Chen, C.-H., Lee, T., Punongbayan, R.S., 1995. Fission-track dating of volcanics in the northern part of the Taiwan-Luzon Arc: eruption ages and evidence for crustal contamination. Journal of Southeast Asian Earth Sciences 11, 81-93.

Yen, T.P., Chen, P.Y., 1953. Explanatory Text of the Geologic Map of Taiwan, Tatunshan Sheet. Geological Survey of Taiwan.

Yu, H.-S., Chou, Y.-W., 2001. Characteristics and development of the flexural forebuldge and basal unconformity of Western Taiwan Foreland Basin. Tectonophysics 333, 277-291.

Yu, S.-B., Chen, H.-Y., Kuo, L.-C., 1997. Velocity field of GPS stations in the Taiwan area. Tectonophysics 274, 41-59.

Itrax Core Scanner description and data sheet

The Itrax Core Scanner™ determines the variation of all elements from Mg to U along wet as well as dry cores. It offers very high speed of analysis combined with high sensitivity, variable analytical step size and non-destructive scans. The sensor range includes a unique combination of XRF and X-ray radiography, plus high-quality sample images and magnetic susceptibility. Typical applications include paleoclimate and paleoenvironmental reconstruction, lacustrine and marine sediment studies, quaternary geology, cyclostratigraphy and varve analysis ,core correlation and composite sequence construction, drill-core characterization, sedimentology and stratigraphic interpretation

Main benefits

- A unique combination of XRF scanning and X-ray radiography, plus RGB camera and Magnetic Susceptibility in one fully position-calibrated system.
- Very fast XRF scanning at any step size while maintaining high data quality, from centimeter scale and all the way down to sub-millimeter analyses.
- Provides excellent preservation of sensitive samples through non-contact scanning combined with very high analytical speed.
- Measurement of all detectable elements simultaneously in a single scan.
- Excels in proxy studies thanks to very high precision in peak-area determination combined with high sensitivity across a wide range of elements.
- Provides uniquely strong positional precision and repeatability, making it ideal for spliced records and high-resolution stratigraphic studies where position precision is crucial.



Itrax Core Scanner samples are inserted in the left wing, and automatically moved during scanning. The user sets the scan parameters from the computer, and can then leave the instrument to apply the measurements unattended.

- Gives users extended control of the analytical process through easy access to the XRF spectrum from every analytical point.
- Is the leading XRF scanner for sediments examinations worldwide, supported by a large installed base and with extensive scientific publication output of over 200 scientific articles published yearly.
- Is the preferred choice for labs requiring both maximum throughput and the highest performance at millimeter and sub-millimeter resolution.
- Only Itrax Core Scanner maintains the same high data quality per unit time across all resolutions from centimeter scale down to 0.1 millimeter.

Features

The Itrax Core Scanner™ can scan both wet and dry cores. It offers high sensitivity across a wide elemental range, including the elements commonly used in sediment proxy studies as well as rare earth elements (REEs). The analytical step length can be easily adjusted in the software to meet different resolution requirements, while ensuring continuous coverage over the full step interval and sample length. This makes Itrax equally well suited to rapid sample overviews and high-resolution detailed scans.



This photo shows a split sediment core sample in a liner being placed in the Itrax Core Scanner. The long sample holder allows for all standard core lengths and is easily accessible. All scanning can be performed with or without a foil covering the sample surface, as chosen by the user.

Compatible sample types include wet cores, rock drill cores, slabs, U-channels, peat, cave stones, etc. As long as the samples are reasonably flat, the Itrax follows the surface and automatically adjusts the measurement to a constant distance over the surface.

Only the Itrax scanner family can perform XRF scans that cover all elements, from the lightest to the heaviest, in a single pass.

Itrax does not make direct contact with the sample surface during scanning, but analyzes it from a fixed, close distance.] The advantages include:

- No deformation of soft sediment samples
- The risk of forming a water film between a wet sample and an applied XRF foil is minimized, since no pressing on the film occurs.
- Drying or deformation of the sample between scans is avoided, as can occur in multi-pass scanners that touch the surface.
- Total scan time is minimized by eliminating the need for vertical up-and-down movement at each analytical step.

The combination of XRF and X-ray radiographic imaging enables detailed identification of laminae and clear differentiation between stratigraphic layers and individual particles. This, plus the uniquely precise steps positioning along the sample provides an indispensable examination tool for high-resolution core analysis.

Itrax Core Scanner™ **excels** in rapid analysis, with performance that has been continuously improved over the years. This high speed is enabled by several features, including the high-power X-ray tube, the very short time between analytical steps, the non-contact measurement principle, and the unique Itrax capability to determine all elements simultaneously at a single voltage. Together, these features reduce scan time to only a fraction of that required by other XRF scanners, without compromising detection limits, quantitative precision, or reproducibility.

Itrax Core Scanner™ provides consistently high analysis speed at every measurement point, regardless of the selected analytical resolution, from centimeter scale down to sub-millimeter resolution This unique capability can save substantial scan time, especially when analyzing long samples at millimeter-scale steps or smaller. [The very short time between analytical steps further minimizes total scan time, helping to reduce the time wet samples remain at room temperature.

The digital X-ray radiography system transfers X-ray transmission images directly to the computer. Its advanced design is intended to reveal very small variations in density and chemical composition. X-ray radiography is an ideal complement to the XRF data, helping you verify whether a XRF peak is to be interpreted as, for example, a pebble or as a stratigraphic layer.

The magnetic susceptibility add-on sensor requires contact with the sample surface and is therefore used as the final step in the measurement sequence, when included.

Itrax Core scanner offers uniquely high precision and repeatability in sample positioning, ensuring reliable data at every point, which is crucial, for example, for spliced cores.

The high-quality RGB camera in today's Itrax scanners is equipped with crossed polarizing filters that reduce glare from wet surfaces as well as other surface features that scatter light. The result is high-quality images that reveal details more clearly than the naked eye. The high image quality also enables effective contrast enhancement.

All sensors are position-calibrated relative to one another and operate during scanning with high precision.

Continued on next page

Software ecosystem

The software package is developed by Cox and supports the full analytical workflow from acquisition to data review and interpretation.

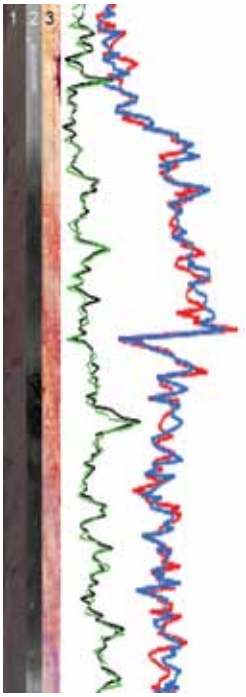
Itrax Navigator, our software for instrument operation and data display during scanning.

Q-spec, an advanced software package for display of spectra and automated extraction of peak areas for each element, from the x-ray spectra. It separates peaks from background noise and gives you net element peak areas. It also identifies and separates overlapping peaks and identifies sum peaks and diffraction peaks if such appears. It can calculate element concentrations by a simple click, is based on the Fundamental Parameter method and delivers good data from a uniquely wide range of sample matrices with one calibration. Calibrations with other standard samples will only be needed for odd matrix compositions. Another unique Q-spec feature is determination of the average atomic number in the sample volume, including the elements that are too light to detect with the XRF. This adds further precision to the calculations of element concentrations. The Qspec generates a summary file containing all data from each measurement step together with a note that indicates whether each analysis is correct. This puts the user in control of the analysis at every step. Incorrect data can e.g. be due to the appearance of an unexpected element appearing. XRF spectra from each analytical point is automatically stored for easy user access, review and re-processing.

The ReDiCore software is for display and presentation of element profiles, radiographic images, magnetic susceptibility data, and sample photos together.

The BoreHole Viewer offers data display and interactive examination of whole boreholes, compiling data from several core scans.

The data can be moved seamlessly between the different software apps as well as into e.g. Excel.



This photo shows a 0.1 m. section of a sediment core. Part 1. is the core section as seen by eye. Part 3. been contrast-enhanced. Part 2. in the center is the radiographic image. To the right are four graphs from the XRF scan, showing the variation in concentration along this sample section. The red and the blue graphs show Silica distribution from two consecutive scans. The green and the black graphs show the two Manganese profiles from the two scans. ***Please note the very good repeatability in peak position as well as peak size*** (arbitrary scale). *Measuring time was only 1 second at each position, with 0.2 mm steps. Extending the time improves the precision further. The average Si concentration was ~10%, and Manganese ~0.07%. This core was sampled off Greenland in 2012. Data with courtesy of Dr. R. Gyllencreutz, Stockholm Univ.*

Detection limits

Itrax Core Scanner detects all elements across the whole range Mg-U. High sensitivity, well-defined peaks, and high reproducibility for most metals provide the precision needed for confident use of element ratios in proxy studies.

The table lists the Detection Limits for selected elements of common interest. These values are examples spanning light to heavy elements within the full range detectable by this scanner.] The first value for each element shows the detection limit using a Cr anode x-ray tube, which has higher sensitivity for light elements. The second value is the value when applying a Mo tube, offering somewhat better sensitivity for the heavier elements. As a third alternative, a Rh anode x-ray tube can be applied when Mo is of special interest together with other heavier elements (not listed, but available on request). The reference material used is NIST610, measured at 100 seconds, applying the standard scientific model for calculations. Please contact us if you would like information about some element not listed.

Element	PPM	Element	PPM	Element	PPM
Mg	2230/-	V	16/12	Ba	9/51
Al	4089/575	Mn	24/9	Cd	3/144
Si	217/1249	Fe	24/9	La	15/47
P	104/465	Br	11/8	Hf	21/51
S	56/204	Rb	12/9	Hg	28/15
K	10/36	Sr	13/9	Pb	25/14
Ca	7/25	Zr	15/73	Th	28/16
Ti	2/14	Mo	14/184	U	35/19

Specifications

Function/Parameter	Value/Description
XRF scans and data	Maximum count rate of the XRF detector, up to >300,000 cps, allowing for very fast analyses. Better than 133 eV FWHM at 5.9 keV, at any count rate peak width, for best element peak separation. Typical time setting is 3 (1-10) sec. per scan step for a marine sediment total time per analytical step, covering all detected elements. The time between each measurement step is only a fraction of the time needed in scanners that use up/down movement between each step. The XRF spot size is 0.2 mmx8mm (8mm XRF scan width) as standard, with sharp edges, (0.1mmx8mm beam size optionally).
X-ray radiography	Digital radiography with data fed straight into the computer, resolving variations in sample chemistry and density down to ~0.5%. Image width is ~20 millimeters. Maximum sample thickness depends on composition (~60 mm for a typical marine sediment).
Magnetic Susceptibility	Bartington MS2E type, having a measuring spot of ~4x10mm. Touches sample surface (add-on).
Optical images	High quality RGB images, ~50 micrometer pixel size, an image width of about 100 millimeters, and user selected length along the core. Glare in wet sample photos is minimized by the included crossed polarizing filters.
X-ray Beam	Well defined x-ray beam with 0.2mmx20mm (optionally 0.1mmx20mm) with sharp edges and even intensity distribution. This makes small step analyses down to 0.2/0.1 mm just as fast as larger steps. Larger steps are implemented by sweeping over the selected step, without information loss. Enhanced intensity by Polyflat™ x-ray waveguide speeding up analyses for higher sample throughput.
Scanning steps	Any step from full sample length down to 0.01 millimeter, offering the best available precision in scan step positioning. Allows for continous scanning without loss of any information along a sample, as well as fast overview by “jumping” between positions at selectable jump length.
Element range and X-Ray tubes	Most users use only one tube type, but Cr, Mo and Rh anode tubes are available as alternatives, depending on elements of most interest for the user. The range is Mg – U for a Cr tube, and Al-U for Mo and Rh tubes. Each tube covers the whole respective element range, with detection limits as described under Detection limits section above. The tubes are easily shifted in ~15 minutes. These high power x-ray tubes are operated at 1650 W for high performance analyses. You are welcome to contact us in case you want more details.
Sample dimensions	Up to 1800 (L) x 122 mm Ø split core / 66 mm full core.
Instrument size and weight	4500 x 820 x 1570 mm LxWxH, ~1100 Kg.
Quantitative calibration	The State-of-the-art element quantification software is pre-calibrated and covers a very wide range of sample matrices. More standards can be added but are only needed for odd sample compositions.
Safety Registration	Ch-08425/S, in Swedish Radiation Safety Authority, plus approved for use in many other countries. The radiation level is below 0.5 µSv/h, allowing for work close to the instrument without limitations.

All specifications and all information in this document are subject to improvements, changes and updates. Please contact us if you want more information.

COX ANALYTICAL
Cox Analytical Systems www.coxsys.se phone: +46 708 3660 info@coxsys.se

Itrax FleXRay XRF Scanner description and data sheet

The ItraxFleXRay XRF Scanner™ determines elemental variations from Na to U along both wet and dry cores. It combines very high analytical speed with high sensitivity across the full elemental range, variable step size, and non-destructive scanning. Typical applications include paleoclimate and paleoenvironmental reconstruction, lacustrine and marine sediment studies, quaternary geology, cyclostratigraphy and varve analysis ,core correlation and composite sequence construction, drill-core characterization, sedimentology and stratigraphic interpretationThe sensor range includes high- quality sample images, magnetic susceptibility and spectrometer options.

Main benefits

- Itrax FleXRay™ combines high-performance XRF scanning with high-quality RGB imaging and, as optional add-ons, magnetic susceptibility and spectrometers in different spectral ranges, with all sensors calibrated to matching lateral positions.
- Itrax scanners offer exceptionally high scanning speed while maintaining high data quality.
- Itrax scanners preserve samples through non-contact scanning and maintain high analytical throughput and data quality in a unique way, even at step sizes down to 1 mm.
- Particularly well suited to proxy studies thanks to high precision in peak-area determination, good sensitivity across a wide range of elements, and precise lateral positioning of the data.
- This XRF scanner delivers high analytical speed without physical contact with the sample. It is especially strong in combining speed and analytical quality at any resolution down to millimeter-scale, and can also be configured for sub-millimeter analytical step sizes.



Itrax FleXRay Scanner offers superb performance, and excels in fast scanning, good sensitivity for a very wide range of elements, combined with cutting edge quantitative capacity.

- Gives the user strong control of the analytical process through easy access to the XRF spectrum from each analytical point.
- Provides high precision in sample positioning at each analytical point, helping ensure that every data value is associated with the correct location.
- Itrax FleXRay Scanner™ is part of the Itrax family of XRF scanners for sediments and drill cores, with installations worldwide and data represented in well over 2,000 scientific publications and a yearly groth in number of articles with more than 200.
- Itrax FleXRay Scanner is well suited to proxy studies because it analyzes a wide range of elements from Na to U with high precision, sensitivity, and variable lateral resolution. Furthermore, all elements are determined in the same XRF scan, under the same analytical conditions, eliminating time-consuming rescans at other voltages and reducing the need for frequent recalibration to normalize data between analytical points.

Features

The FleXRay Scanner is a highly useful instrument for preliminary analysis of both wet and dry cores It offers high sensitivity across a wide element range, with user-selectable step sizes to accommodate different resolution requirements.

Different sample types can be scanned, including wet cores, rock drill cores, slabs, U-channels, peat, cave stones, and related sample types.. As long as the samples are reasonably flat, FleXRay follows the sample surface to provide accurate and reproducible analytical data.

Itrax FleXRay is available in two versions: one for both wet and dry samples, and one optimized for dry samples such as drill cores.



The pull-out sample holder makes it convenient, quick and safe to switch samples, whether these are sediments in liners or drill cores.

High sample throughput is a key feature, enabled by fast XRF measurements and very short overhead time between analytical points.

This high scan speed is especially advantageous for high-resolution scanning while still maintaining excellent detection limits, precision, and reproducibility at a typical analysis time of 3 seconds per analytical step. Several features contribute to this performance, including the Cox proprietary X-ray beam guide that increases X-ray intensity at the sample, the short time between analytical steps, the non-contact measurement principle, and the ability to determine all elements at one voltage at each step while maintaining high sensitivity across the full range.

By scanning very close to the sample surface without touching it, the sample is preserved. Together with the high precision of peak-area separation and determination for each element, this is important for the detailed identification of laminae.

Smaller beam size and analytical steps all the way down to 0.2 mm are acheived with the high resolution kit available as an add-on.

Only Itrax scanners perform XRF scans of sediments that cover all elements from Na to U in a single pass. This ensures that all elements are measured under the same analytical conditions. This provides strong detection limits across the full elemental range and avoids time-consuming rescans at other voltages.

Other unique features of Itrax scanners are that the stability of hardware as well as data processing software make it unnecessary to do frequent re-calibrations during the scans, saving a lot of overhead time during scanning.

Your samples remain minimally affected during and after scanning because Itrax does not come into physical contact with the sample surface. This brings three main advantages: First, pressure on the sample surface is avoided, reducing the risk of deformation in soft samples. Secondly, the risk of forcing water out to form a film between a wet sample and an applied foil is reduced, lowering the risk of adversely affecting the data. Third, the non-contact technique minimizes the time between analytical points, substantially reducing total scan time.

If a magnetic susceptibility sensor is added to your Itrax FleXRay, those measurements are performed last in the analytical sequence, since they require contact with the sample surface and should therefore follow the non-contact measurements.

The RGB camera provides very high-quality images and is equipped with crossed polarizing filters that strongly reduce glare from wet sample surfaces.

Itrax FleXRay scanners offer high precision and repeatability in positioning at each analytical point along the sample. This is needed to ensure correct data at every point, which is important when thickness and absolute positions of laminae are in focus, for instance for spliced core records.

Continued on next page

Software ecosystem

The entire software package is developed by Cox, and includes:

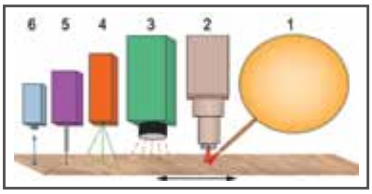
Itrax Navigator, our software for instrument control and real-time data display during scanning.

Q-spec, an advanced software package for spectral display and automated extraction of element peak areas from the X-ray spectra. It also identifies and resolves overlapping peaks, and detects sum peaks and diffraction peaks when they occur. It also identifies and resolves overlapping peaks and detects sum peaks and diffraction peaks when they occur. Element concentrations can be calculated with a simple click; the method is based on Fundamental Parameters and provides robust results across a uniquely wide range of sample matrices using a single calibration. Additional calibrations with other standards are typically only needed for unusual matrix compositions. Another distinctive Q-spec feature is determination of the average atomic number of the analyzed sample volume, including elements too light to be detected directly by XRF. This further improves the precision of the concentration calculations. Q-spec generates a summary file containing all data from each measurement step, together with an indicator showing whether the analysis passed quality checks. This helps keep the user in control of the analytical process at every step. For example, flagged data may result from the presence of an unexpected element. XRF spectra from each analytical point are automatically stored for easy access, review, and reprocessing.

ReDiCore is used to display and present element profiles, radiographic images, magnetic susceptibility data, and sample photographs together.

BoreHole Viewer enables data display and interactive examination of complete boreholes by compiling data from several core scans

Data can be transferred seamlessly between the different software applications and into programs such as Excel.]



This image shows the principal setup of the Itrax FleXRay x-ray source and sensors.
1. X-ray tube with Polyflat™ x-ray optics. 2. XRF detector. 3. RGB camera. 4. Laser distance gague. 5. Spectrometer. 6. Magnetic susceptibility sensor.

Detection limits

Itrax FleXRay Scanner detects elements across the full range from Na to U. High sensitivity, well-defined peaks, and high reproducibility for most metals provide the precision needed for confident use of element ratios in proxy studies.

The table lists detection limits for selected elements of common interest. These values are examples spanning light to heavy elements within the full range detectable by this scanner. Na, Mg, and Al are listed with two values because the FleXRay version for wet sediments has somewhat higher detection limits for these elements. The second value for Na, Mg and Al refers to the FleXRay version for wet and dry samples.

Element	PPM	Element	PPM	Element	PPM
Na	1251/3720	Ti	8	Ba	23
Mg	191/212	V	7	Cd	64
Al	56/60	Mn	6	La	21
Si	30	Br	5	Hf	10
P	22	Rb	5	Hg	9
S	12	Sr	6	Pb	9
K	11	Zr	6	Th	11
Ca	9	Mo	6	U	12

The reference material used is NIST 610, measured at 100 seconds, applying the standard scientific model for the calculations. *Please contact us if you would like information on any specific element not listed here.*

Specifications

Function/Parameter	Value/Description
XRF scans and data	Typical time setting is 3 (1-10) sec. per scan step for a marine sediment total time per analytical step, covering all detected elements. The XRF spot size is 1mmx8mm (8mm XRF scan width) as standard, (0.2mmx8mm with optional equipment). Maximum count rate of the XRF detector is >300,000 cps, allowing for samples with varying matrices without saturation effects. Better than 134 eV XRF detector FWHM at 5.9 keV, at any count rate peak width. This allows for very good peak separation and mimimized overlap. The overhead time between each XRF step is ~0.7 sec.
Magnetic Susceptibility	Bartington MS2E type, having a measuring spot of ~4x10mm. Touches sample surface (add-on).
Optical images	High quality RGB images, ~50 micrometer pixel size, and an image width of ~100 millimeters. Image quality reductions like glare in wet sample photos and light scatter from rough dry surfaces is minimized by the implemented crossed polarizing filters.
X-ray Beam	Well defined x-ray beam with 1mmx8mm, having sharp edges and an even intensity distribution. Enhanced intensity by Polyflat™ x-ray waveguide speeding up analyses for higher sample throughput.
Scanning steps	Any step from full sample length down to 0.01 millimeter can be selected. Step sizes larger than the beam are implemented by sweeping over the selected step, without information loss. This makes any step size analyses down to 1mm just as fast as larger steps, as larger steps than beam size are achieved by collecting data while sweeping over the selected step. Itrax FleXRay allows for scanning without loss of any information along a sample, and also allows for fast overview through discreet analysis mode, by "jumping" between positions at user selectable jump length and analytical step length.
X-Ray tube	A 60W Rh anode tube with an expected life time of 50,000 hours.
Element range	Na – U for wet and dry samples, determined simultaneously.
Sample dimensions	Up to 1520 (L) x 127 mm Ø split and full core.
Instrument size and weight	~2800x1350x1725 millimeters LxWxH including stand, plus top light. The weight is ~700 kilos.
Quantitative calibration	Peak areas and element concentrations are both available for the user, by a single click. The State-of-the-art element quantification software is pre-calibrated and covers a very wide range of sample matrices without further calibrations. More standards can be added, but are only needed for odd sample compositions.
Safety Registration	Ch-08425/S, in Swedish Radiation Safety Authority, plus is approved for use in many other countries. The dose rate equivalent level is below 0.5 µSv/h, allowing for work close to the instrument without limitations.
Power requirement	As standard 230 volts / 50-60Hz / 16 A one phase / 3kW. Other voltages and/or frequencies can be delivered on request
Available add on's	1. High resolution scanning kit that allows the user to switch beamsize to 0.2 mm. beam, for scanning in the 0.2-0.9 mm range. 2. Magnetic Susceptibility meter Bartington MS2E type, having a measuring spot of ~4x10mm. Touches sample surface. 3. Spectrometer with a choice of configurations. Please contact us for more details.

All specifications and all information in this document are subject to improvements, changes and updates. Please contact us if you want more information.

COX ANALYTICAL
Cox Analytical Systems www.coxsys.se phone: +46 708 3660 info@coxsys.se

SPONSORS


SOCIETY FOR SEDIMENTARY GEOLOGY
100th
1926
2026
ANNIVERSARY


NSTC


COX
ANALYTICAL SYSTEMS


中華民國地質學會
Geological Society Located in Taipei


國立臺灣大學
敦品勵學・愛國愛人


國立中央大學